Chapter 2
Experimental Techniques and Structure of the Underpotential Deposition Phase

2.1 Introduction

The electrochemical deposition of metals on foreign substrates is a complex process, which includes a number of phase formation phenomena. The very initial electrodeposition stages of a metal, M, on a foreign substrate, S, involve adsorption reactions as well as two-dimensional (2D) and/or three-dimensional (3D) nucleation and growth processes. The most important factors determining the mechanism of electrochemical M phase formation on S are the binding energy between the metal adatoms (M_{ads}) and S, as well as the crystallographic misfit between the 3D M bulk lattice parameters and S. As we have shown in Fig. 1.3, when the binding energy between the depositing M-adatoms and the substrate atoms exceeds that between the atoms of the deposited metal, low dimensional iD metal phases ($i = 0$, 1 and 2) are formed onto the foreign metal substrate. This phenomenon, introduced in Chap. 1 as underpotential deposition (upd) [1–4], has been known for a long time and it has been intensively subject of study in the past decades since the 1970s. This has been demonstrated by many studies of the upd process of different metals on mono- and polycrystalline substrates as well as reviews on the subject. The understanding of the nature of this phenomenon as conceived in the middle 1990s can be found in the book of Lorenz et al. [1]. Reviews available in the literature include the works of Kolb et al., Abruña et al., Sudha and Sangaranarayanan, Aramata [5–8], and the work of Szabó [3] concerning the theoretical aspects of upd, updated by Leiva [9], and also the works of Adžic [10] and Kokkinidis [11], concerning mainly the catalytic effects of upd adatoms.

Monolayer amounts of metal adatoms obtained by upd alter the electronic properties of the substrate material itself by changing the interfacial reactivity, and therefore these systems have been the subject of a large number of studies, not only in terms of their fundamental aspects related to electrochemical phenomena (adsorption, charge transfer, nucleation and growth) but also in their technological application for corrosion inhibition or as models for the design of new electrocatalysts, between others. In addition, the study and applications of upd

© Springer International Publishing Switzerland 2016

O.A. Oviedo et al., *Underpotential Deposition*, Monographs in Electrochemistry,
DOI 10.1007/978-3-319-24394-8_2

processes involve now numerous disciplines apart from electrochemistry, such as chemistry, physics and materials science, as discussed in the remaining of this book.

Many electrochemical and surface characterization methods have been employed to study the upd phenomenon. Whereas electrochemical techniques provide valuable information on the kinetics and mechanisms of processes occurring at the metal/solution interface, the molecular specificity required to give unequivocal identification of species formed at electrode surfaces are obtained by a number of in situ and ex situ spectroscopies. These spectroscopic methods have been applied to augment electrochemical approaches and provide information on the elemental and molecular composition, the atomic geometry, and the electronic structure of the interface. The great progress that has been made in the development of new in-situ techniques allowed to obtain important information on electrode processes at the molecular and atomic level. In this Chapter, different techniques used for characterization of upd layers will be discussed briefly and illustrated by appropriate, representative examples.

2.2 Cyclic Voltammetry

Cyclic voltammetry has been and still is the most important routine method for characterizing the upd of a metal M on a foreign metal substrate. This technique consists of scanning linearly the potential of a stationary working electrode with a constant scan rate (dE/dt) between two chosen limits, one or more times, while the current is continuously monitored. The obtained cyclic current-potential curves offer a rapid location of redox potentials of electroactive species and provide a convenient evaluation of the effect of media upon the redox process. Any reaction at the electrode surface will usually be detected as a current superimposed to the base current due to double-layer charging.

The upd process is reflected in cathodic and anodic current density peaks at different potentials, indicating the deposition and dissolution of the metal adsorbate, respectively. The occurrence of distinct adsorption peaks in the cyclic voltammetric measurements indicates that the formation of 1–2 monolayers at underpotentials takes place in several energetically different adsorption steps.[1] The peak structure is found to depend strongly on the crystallographic orientation of the substrate and the density of crystals imperfections [1]. The number of these peaks and positions also depend on the substrate and the crystal plane on which the adsorption takes place as well as on the nature of the electrolyte. The peaks are not well-pronounced for polycrystalline electrodes whose surface presents different

---

[1] To learn more on the relationship between the peak potential and the energetic properties of the monolayer see Chap. 3.

crystallographically oriented domains and a high density of crystal imperfections (e.g. steps, kinks, vacancies) as compared with single crystals.

Some representative examples illustrating what can be achieved with cyclic voltammetry will be presented here.

Gold has been extensively used as electrode material in fundamental electrochemistry and therefore it is interesting to evaluate its behaviour related to M upd. Ag adatoms are attractive to study on such surfaces because they present strong M-S interactions and negligible M-S misfit (the corresponding lattice parameters are $d_{0,\mathrm{Au}} = 2.8840$ Å, $d_{0,\mathrm{Ag}} = 2.8895$ Å) [12].

Figure 2.1 shows cyclic voltammograms for Ag upd in the systems Au(100)/Ag^+, SO_4^{2-} (Fig. 2.1a) and Au(111)/Ag^+, SO_4^{2-} (Fig. 2.1b) [13]. In the case of Au (100) substrates, three different adsorption-desorption (A_i/D_i) peaks are observed in the potential range $15 \leq \Delta E(\mathrm{mV}) \leq 720$. In these experiments, the lower potential limit was kept higher than the bulk deposition potential to prevent alloying processes. For Au(111) substrates, the voltammogramm displays two characteristic adsorption/desorption peaks in the upd range studied.

The deposition of Ag on Au(111) in sulphuric acid has been studied by different groups and some discrepancies in the reported voltammetric curves have been found, depending on the surface state of the substrate, which plays a critical role in the initial stages of metal deposition [13–17]. Yang et al. [18] have revisited these previous results and demonstrated that potential cycling in the upd region introduces some surface defects. They proposed that this procedure gradually transforms the surface into a surface alloy phase, leading to the appearance of another Ag upd peak located at 80 mV more positive than the first upd peak associated with the deposition of Ag on Au terraces.

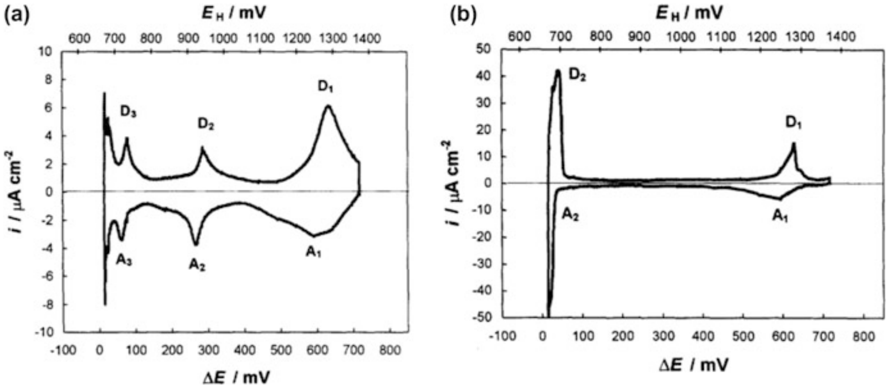

Fig. 2.1 Cyclic voltammograms for the upd of Ag in 5×10^{-3} M Ag_2SO_4 + 0.5 M H_2SO_4 solution at $T = 298$ K on (**a**) Au(100) and (**b**) Au(111) substrates. A_n and D_n with n = 1, 2, 3 denote cathodic adsorption and anodic desorption peaks, respectively. $|\mathrm{d}E/\mathrm{d}t| = 7$ mV s^{-1}. The upper scale corresponds to the hydrogen normal electrode, while the lower is referred to the bulk Ag deposition potential (Reprinted with permission from Ref. [13])

Fig. 2.2 (**a**) Cyclic voltammogram for the upd of Cu on Au(111) in 1 mM $CuSO_4 + 0.05$ M H_2SO_4 solution. $|dE/dt| = 1$ mV s^{-1}. (**b**) Adsorption isotherm corresponding to (**a**), with a schematic view of the proposed Cu structures formed on Au(111) (Reprinted with permission from Ref. [39])

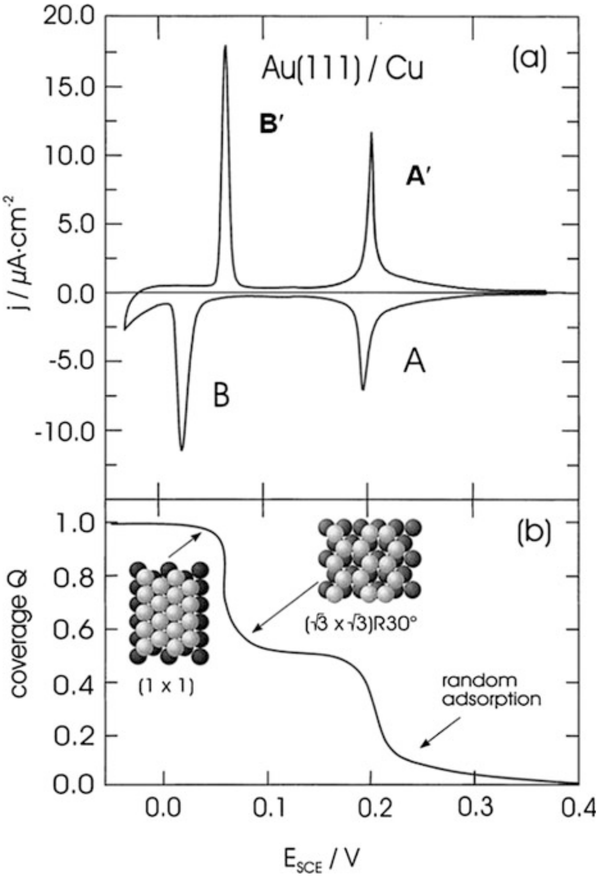

Cu upd on polycrystalline and single crystal gold surfaces, in particular on Au(111), is certainly one of the few systems that has been studied with a wide variety of in-situ techniques including electrochemical ones [19–28], Scanning Tunneling Microscopy [23, 29–31], Atomic Force Microscopy [32], Spectroscopic Methods [33–36] and Quartz Crystal Microbalance [25, 37], and Ex-Situ Techniques such as Low Energy Electron Diffraction, Auger Electron Spectroscopy and Reflection High Energy Electron Diffraction [21, 22, 38].

A typical cyclic voltammogram for Cu upd on Au(111) in sulphuric acid solution is shown in Fig. 2.2a [39]. It is clearly seen that the deposition of a Cu monolayer takes place in the potential region between 0.35 V and 0 V vs SCE, before starting the bulk deposition. The present phenomenon involves two energetically distinct steps, reflected by two pronounced adsorption (A, B)/desorption (A′, B′) peaks pairs. The corresponding charge isotherm and the schematic view of the structures $(\sqrt{3} \times \sqrt{3})R30°$ and (1×1), related to the first and second peaks respectively, are shown in Fig. 2.2b [39]. These structures were associated hitherto to the Cu deposit at a medium coverage (2/3 Cu monolayer) and at a full Cu

Fig. 2.3 Cyclic voltammogram of Au(100) in 0.05 M $H_2S0_4 + 1$ mM $CuSO_4$ solution showing Cu deposition in the underpotential and overpotential region. $|dE/dt| = 2$ mV s^{-1} (Reprinted with permission from Ref. [40])

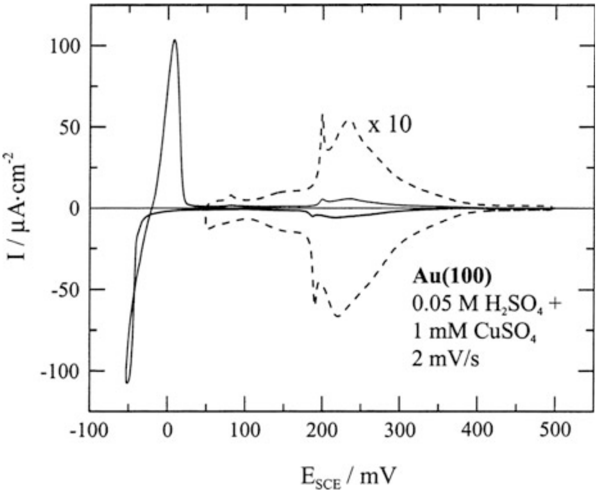

monolayer. The broad shoulder at potential values more positive than 0.2 V was assigned to a random adsorption of Cu atoms.

Different voltammetric features appear in the case of Cu upd on a Au(100) substrate. Figure 2.3 shows the cyclic voltammogram in 0.05 M $H_2S0_4 + 1$ mM $CuSO_4$ solution including also the Cu overpotential region [40]. A Cu monolayer formation was found in the region between 100 and 350 mV and two current density peaks pairs (corresponding to the Cu adsorption/desorption) were observed. The voltammogram obtained in the upd range between 50 and 500 mV is enlarged by a factor of 10 for clarity (dashed curve in the Figure). The charge under the upd peaks was about 400 μC cm^{-2}, which is the expected value for a Cu monolayer formed from divalent cations.

The results obtained by Behm et al., introducing chloride anions in the electrolyte, are shown in Fig. 2.4 [41]. For the sake of comparison, the Cu upd on Au(100) was studied by cyclic voltammetry in both pure sulfate and chloride containing solutions (Fig. 2.4). The voltammetric response was characterized, in agreement with other results [29, 42], by a broad adsorption peak with a small extra structure in solutions free of chloride anions (which splitted into two for lower sulfate concentrations and sweep rate [42]), related to the uptake of a full Cu monolayer. In contrast, the Cu upd in solutions with 10^{-4} M HCl was characterized by a very sharp current peak at 0.3 V. This sharp spike was correlated with the formation of an ordered adlayer superstructure. The location of the corresponding peak due to desorption indicated a reversible adsorption process.

Schiffrin and coworkers [43] have studied Cu upd on several Au surfaces with different single crystal surfaces to demonstrate the effect of step density and step orientation on this process. Figure 2.5 exhibits Cu upd cyclic voltammograms for Au(332), Au(775) and Au(554) surfaces. With the Au(332) surface, two broad, overlapping peaks in the first adsorption/desorption region are observed at 0.52 and 0.56 V vs RHE respectively (Fig. 2.5a). The relative intensity of the peak centered

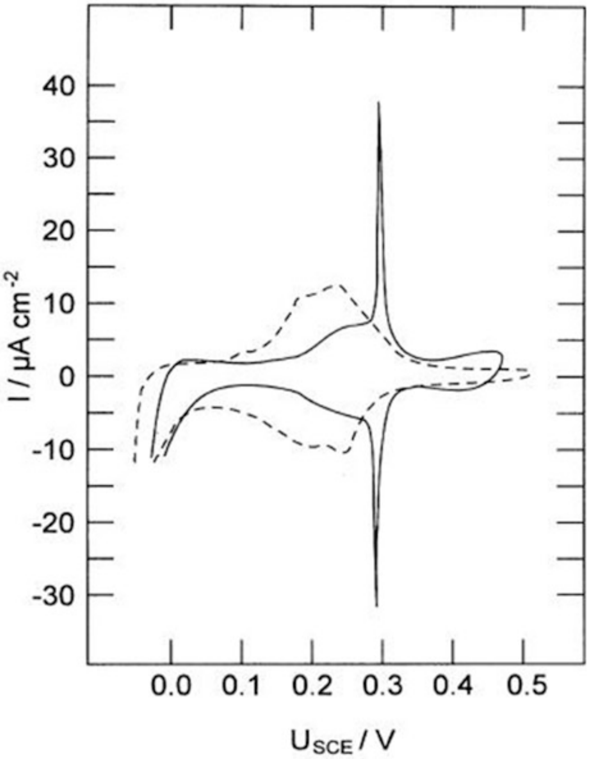

Fig. 2.4 Cyclic voltammograms for Cu upd on Au(100) in 0.01 M H_2SO_4 + 10^{-3} M $CuSO_4$ solution without (*dashed line*) and with 10^{-4} M HCl (*solid line*). $|dE/dt| = 2$ mV s^{-1} (Reprinted with permission from Ref. [41])

at 0.56 V decreases with decreasing step density (Fig. 2.5b, c). The peak at 0.52 V, on the other hand, was assigned to the formation of the (√3 × √3)R30° structure on the (111) terraced regions, which becomes more clearly defined as the (111) terrace width is increased in the order Au(332), Au(775), Au(554), respectively. In summary, on the basis of the comparison with voltammograms for the Au(111) and Au(110) low index surfaces, these two peaks were assigned to Cu deposition on the (110) step sites and the formation of a (√3 × √3)R30° phase on the (111) terraces, respectively. The second upd peak in the region of 0.34–0.40 V was assigned to the (√3 × √3)R30° → (1 × 1) phase transition, which occurs at the most positive potentials on the most stepped surface, Au(332). The increase in step density and the corresponding reduction in (111) terrace width favours this transition and shows the influence of structural or electronic effects on the energetics and/or kinetics of the phase transition.

The structure of the metal adlayer may also be found to be strongly dependent on the anion species of the electrolyte, as mentioned before, something that was

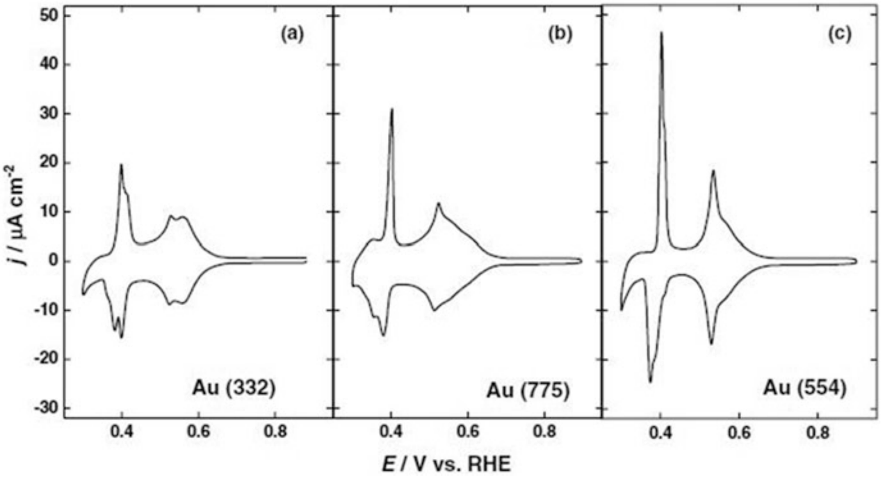

Fig. 2.5 Cyclic voltammograms of Cu upd in 0.05 M H_2SO_4 + 1 mM $CuSO_4$ on different stepped surfaces. (**a**) Au(332), (**b**) Au(775) and (**c**) Au(554). $|dE/dt| = 5$ mV s^{-1} (Reprinted with permission from Ref. [43])

initially evidenced from cyclic voltammograms and later confirmed by direct structural information from ex-situ and in-situ experiments. We will return to this point below when addressing the study of Cu upd on Au(111) by in-situ Scanning Tunneling Microscopy.

In early times, upd of metal adatoms was studied on polycrystalline inert metals, such as Pt and Au, using radiotracer measurements.[2] Some of these works are those from Bowles, who investigated the adsorption on Pt of the following metal adatoms: Tl [44, 45], Sn [46], Cu, Cd, Sn, Tl and Bi [47], Cu [48], Bi [49]; and from Horányi et al. who analyzed the influence of Cu upd on the adsorption of chloride and bisulfate anions using also Pt electrodes [50, 51].

2.3 Radiotracer Methods

Radiotracer methods are particularly useful in the detection and identification of adsorbed layers on substrates surfaces. They allow to determine directly the coverage vs. current or potential relationship under steady state conditions (potentiostatic or galvanostatic) in the course of electrode processes without the knowledge of the adsorption isotherms. These methods, coupled with electrochemical techniques, provide direct in-situ measurements of surface concentrations with simultaneous control of electrochemical parameters, such as potential, current or charge. They are also used to study the adsorption of anions using radiolabeled

---

[2] See pre-history of upd in Chap. 1.

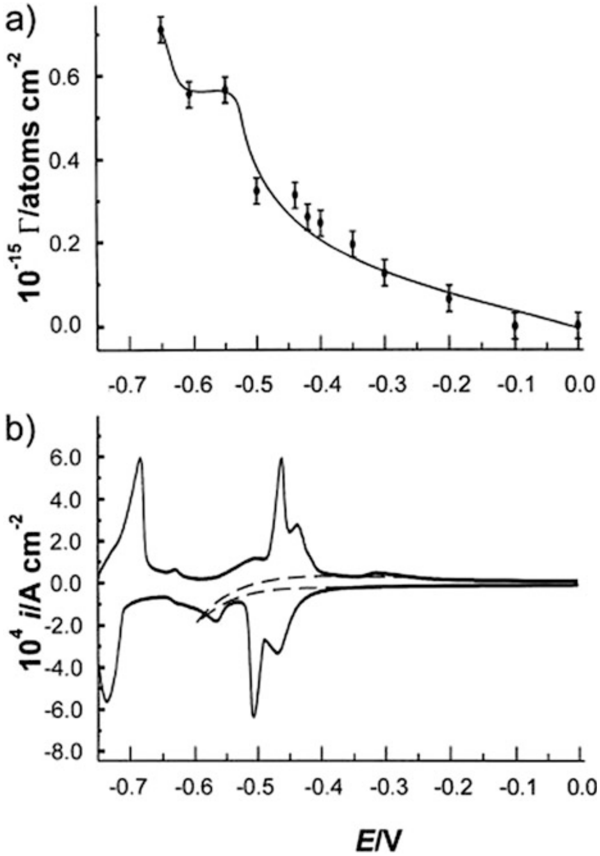

Fig. 2.6 (**a**) Surface concentration of Tl on Au(111) determined radiometrically, $C_{\mathrm{HClO_4}} = 0.1$ M, $C_{\mathrm{Tl^+}} = 10^{-3}$ M, (**b**) Cyclic voltammogram for the same system (*solid line*) and in thallium free solution (*dashed line*). $|\mathrm{d}E/\mathrm{d}t| = 200$ mV s^{-1} (Reprinted with permission from Ref. [53])

species in the course of the M upd phenomenon contributing to a better understanding of the process. The radiometric methods for determining the surface concentration of adsorbed species may be precise and versatile, depending on the specific activity of the isotopes used and the signals coming from the adsorbed layer, so that the signal from solution phase can be easily separated. Further information about this technique can be found in Chap. 4 of the book Radiotracer Studies of Interfaces, edited by G. Horányi [52].

Some illustrative examples of the use of radiotracer techniques are discussed now.

Sobkowski et al. [53] have employed a radiotracer technique combined with cyclic voltammetry to analyze thallium upd on (111), (110) and (100) single crystal silver electrodes from perchloric acid solutions. They compared the radiometric measurements of the amount of thallium accumulated at the metal/solution interface with the voltammetric curves. Figure 2.6a, b show the Tl surface concentration on Au(111) measured radiometrically and the corresponding cyclic voltammograms for the system. They found for Ag(111) electrodes that the accumulation of the adsorbate at the interface occurred at potentials more positive than

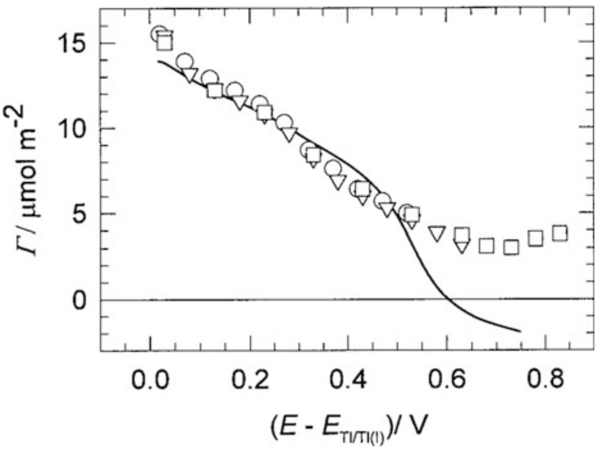

Fig. 2.7 Comparison of the positive-going potential dependence of Tl surface concentration calculated from the voltammogram (*full line*) in 1×10^{-4} M Tl$^+$ + 0.1 M KOH solution, $|dE/dt| = 5$ mV s^{-1} (*solid curve*) and measured by the radiotracer method in the same blank solution containing 1×10^{-4} M Tl$^+$ (○) and 1×10^{-5} M Tl$^+$ (□ first and ▽ third cycle of measurements). The Nernst potential for Tl/Tl$^+$ is −0.57 V in 1×10^{-5} M Tl$^+$ and −0.63 V in 1×10^{-4} M Tl$^+$ solutions (Reprinted with permission from Ref. [54])

those at which the voltammetric upd peaks take place, suggesting that the discharging process is preceeded by the adsorption of thallium. Such an observation was possible owing to the specific feature of the radiometric method, which allows to record both the thallium deposited on the electrode surface and the accumulation of Tl species at the interface. Hence, the voltammetric peaks represent the process of discharge of thallium ions, which were earlier adsorbed. In these experiments, the monolayer surface concentration was determined to be independent of the crystallographic orientation of silver electrodes, suggesting the formation of a nonepitaxial Tl monolayer.

Poškus and Agafonovas [54] have investigated thallium upd and adsorption on polycrystalline gold in alkaline thallium solutions using radiotracer and voltammetric methods. While the radiotracer measurement allowed to obtain the total concentration of thallium atoms and ions at the electrode surface, cyclic voltammetry allowed to calculate the thallium surface concentration only due to the upd process. The authors found that in the potential region between the Tl/Tl$^+$ equilibrium potential and the main upd peak, both measurements are close, indicating that the thallium surface concentration is mainly due to thallium upd. However, at more positive potentials, in contrast to acidic solutions, the potential dependence of the thallium surface concentration above the main upd peak measured by the radiotracer method does not drop to zero but passes through a minimum, suggesting that the adsorption of thallium cations is induced by the specific adsorption of hydroxyl anions. This behaviour is shown in Fig. 2.7.

Radiometric studies for Cu upd on polycrystalline gold were performed by Zelenay et al. [55], to analyse bisulfate adsorption on Cu upd deposits on gold in

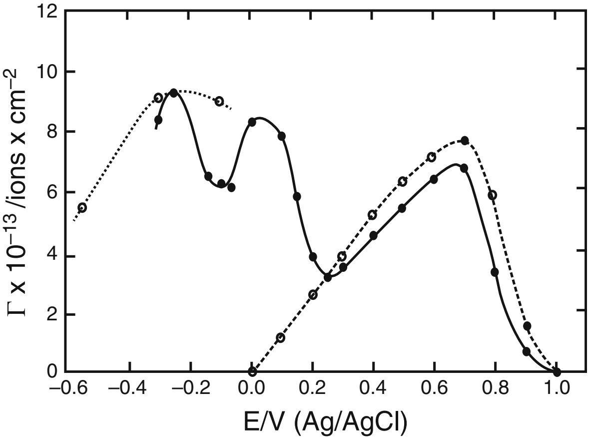

Fig. 2.8 Bisulfate adsorption vs E in the system Au (poly) / 0.05 M $KClO_4$ + 5 × 10^{-4} M Cu $(ClO_4)_2$ (containing 8.7 × 10^{-5} M Na_2SO_4) (●—), as obtained from radiometric experiments. For comparison, bisulfate adsorption data for gold (○—) and copper (○ · ·) electrodes in 0.05 M $KClO_4$ are also included (Reprinted with permission from Ref. [55])

neutral perchlorate medium, i.e. 0.05 M $KClO_4$ + 5 × 10^{-4} M $Cu(ClO_4)_2$ solution containing 8.7 × 10^{-5} M Na_2SO_4 (^{35}S labeled). Since this method allows to measure absolute surface concentrations on smooth electrode surfaces with a detection limit of a few percent of a monolayer, it provides an insight into how anions interfere with the different stages of the M upd. Their Γ vs E measurements are presented in Fig. 2.8, showing a first maximum in the curve at potentials more positive than the Cu upd region, where no Cu deposits are present on the Au electrode. The amount of adsorbed bisulfate was however lower than that obtained for solutions without Cu^{2+} ions. Therefore, it was assumed that a possible formation of negatively charged hydroxy complexes of copper followed by their physisorption on the electrode surface cannot be excluded. The surface concentration of the anions rises sharply as the upd layer of copper is formed, indicating that the adsorption of bisulfate becomes interconnected with copper electrodeposition. A second maximum on the curve was observed when a Cu monolayer was formed on the surface until a third one appeared at more negative potentials when a few layers of bulk Cu deposit is formed. In the latter case, the behaviour of bisulfate adsorption is similar to that taking place on a solid polycrystalline copper surface. The authors also correlated the anion surface concentrations obtained through the radiometric experiments with the current-potential curves for the copper electrodeposition process.

2.4 Potential Step

The potential step technique has been applied to study the kinetics of M upd, as it is the case for example of the underpotential deposition of Cu on Au(111) in sulphuric acid solutions [56]. In these experiments, the potential was first held at a value where no copper was present on the surface for a few minutes, and then it was cycled to the desired value in the upd range. After a waiting time of 60 s, potential steps were applied and the resulting current transients were obtained in the potential

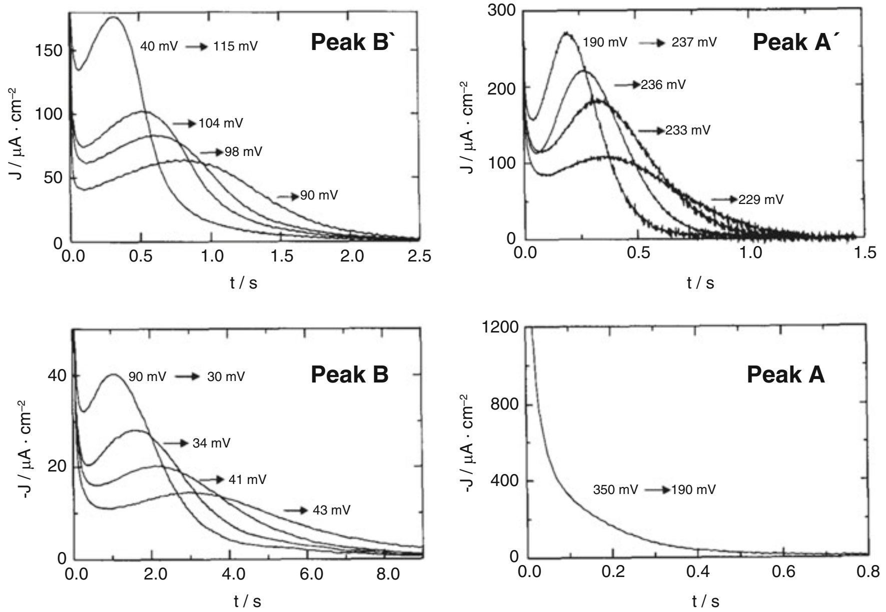

Fig. 2.9 Current transients for peaks A, A′, B, B′ of the cyclic voltammogram in the system Au(111)/ 1 mM $CuSO_4 + 0.05$ M H_2SO_4 (See Fig. 2.2). Potential steps are indicated in the figures (Reprinted with permission from Ref. [56])

regions corresponding to the four individual peaks found in the voltammogram of Fig. 2.2a, as given in Fig. 2.9. A typical shape of the current transient for the first adsorption peak A, showed after double-layer charging, a monotonic decay going to zero for long times. The experimental data were then analized to determine the mechanism of nucleation and growth of the Cu upd process. Linearization of the measured transient by the Cottrell equation ($I(t) \propto t^{-1/2}$) or by means of an exponential law ($I(t) \propto \exp[-kT]$), yielded nonlinear relationships, indicating that there is no pure diffusion control. The rising transients for peak B showed a current maximum, which shifted to shorter times when the overpotential increased. After long times all transients merged at a residual current value close to zero, which was associated by the authors to the side reaction of Cu^+ formation [57]. Transients for the corresponding desorption peak B′ exhibited a similar appearance to those of peak B, but in this case, the current fell to zero at longer times and no offset due to the Cu^{2+}/Cu^+ reaction was observed, as the potential was already too positive for this reaction to occur. Finally, the transients recorded for peak A′ have the same shape as those of peaks B and B′. The shape of the transients for peaks B, B′ and A′ suggest the presence of a nucleation and growth process.[3] The authors used the well known Bewick-Fleischmann-Thirsk (BFT) model for nucleation and growth [58] and found a good agreement

---

[3] See discussion of nucleation and growth in Chap. 3.

between theory and experiment for instantaneous nucleation at long times. On the other hand, the rising parts of the transients were only poorly reproduced by the model due to its superposition with a falling transient at short times, directly after double-layer charging. They explained this discrepancy considering that adsorption at defect sites should be taken into account as a parallel reaction. Thus, they concluded that the measured current transients obtained for deposition and dissolution of Cu adlayer on Au(111) in sulphuric acid solution could be described by a model which assumes a two-dimensional nucleation and growth mechanism accompanied by an adsorption (desorption) process, with both proceeding at different electrode sites.

2.5 Equilibrium-Coverage-Potential Isotherms

Structural features of the upd layer were first derived, indirectly, from equilibrium-coverage-potential isotherms using single crystal substrates [57, 59].

Schulze and Dickertmann [57] analyzed M monolayer formation of Cu, Bi, Pb, Tl and Sb at Au(hkl) electrodes with (hkl) = (111), (110) and (100) by means of their voltammetric desorption spectra, obtaining characteristic peaks that depend on the nature of the adsorbate as well as on the substrate orientation. They found that at low coverages, peak charge data obtained by integration of current/time curves yielded surface concentrations which fitted well with ordered structures. Under these conditions, a “mono-molecular” adsorption layer was found for Cu^{2+}, Pb^{2+} and Bi^{3+}.

The adsorption equilibrium isotherm provides a description of the energetics of adsorbates at the electrode-solution interface. The surface concentration of adsorbate is obtained as a function of solution concentration, electrode potential and the interactions of the adsorbate with other species.

The multi-peak structures of cyclic voltammograms in the upd range correspond to steps in the coverage-potential isotherms. This fact indicates a stepwise formation of two dimensional upd adlayers with different superlattice structures depending of substrate matrix and potential [60] as was pointed out above. The coverage can be determined by integrating the charge under the cathodic and/or anodic peaks in the cyclic voltammograms. The charge obtained can be transformed into a surface coverage assuming that the deposited metal has no partial charge, that the M layer packs into a given structure, and that the electrochemically active area of the electrode surface is known.

Another way to determine the adsorption isotherms is measuring the desorption of the adsorbed metal by potential steps. Figure 2.2b shows the dependence of Cu coverage (normalized charge due to Cu upd) on potential in the system Au(111)/1 mM $CuSO_4$ + 0.05 M H_2SO_4 [39].

2.6 Twin-Electrode Thin-Layer

Another powerful tool for studying upd systems is the twin-electrode thin-layer (TTL) technique, which was introduced by Schmidt et al. using polycrystalline substrates [61, 62]. This method allows independent and precise charge density (q) and surface excess (Γ) measurements. Thus, the metal ion flux can be well separated from anion adsorption-desorption processes. Detailed design and operation of the apparatus have been described elsewhere [61–63]. A schematic view of the TTL cell is presented in Fig. 2.10. The main part of the thin layer cell consists in two planar-parallel electrodes, the working or indicator electrode (IE) and the generator electrode (GE), closely spaced by a constant distance of about 50 µm. Both electrodes are metal rods, fitted in insulating holders, e.g., Teflon, and separated at a desired distance by an insulating spacer (50 µm thickness). The small electrolyte volume between them constitutes the "thin layer", which is separated by small capillaries from the main part of the electrochemical cell containing the counter and reference electrodes. The GE is composed of the same metal as that to be deposited on the IE, and both electrodes may be independently polarized by an appropriate bipotentiostat.

The metal ion activity ($a_{\mathrm{M}^{z+}_{(\mathrm{aq})}}$) in the thin layer cell is given by the application of a constant potential to the GE according to the Nernst equation for a 3D M phase. Therefore, any $a_{\mathrm{M}^{z+}_{(\mathrm{aq})}}$ changes within the thin layer due to metal ion adsorption or desorption at the IE are rapidly compensated by M dissolution or deposition at the

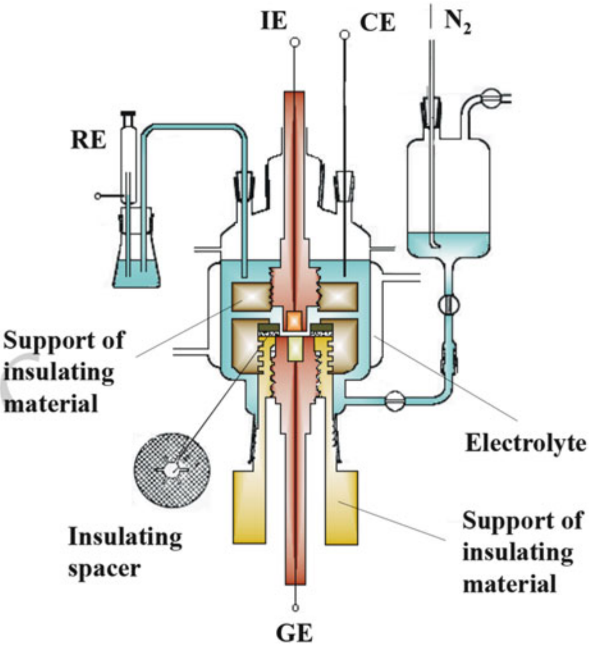

Fig. 2.10 Schematic view of the twin-electrode thin layer cell. Electrodes: *IE* (working or indicator electrode), *GE* (generator electrode), *RE* (reference electrode), *CE* (counter electrode)

reversible GE. The potential of the IE may be scanned at a constant rate between defined starting and final potentials, for which equilibrium conditions are adjusted. The integrals of the corresponding current-time transients in the IE circuit are related to changes in q, whereas those of the current-time transients in the GE circuit correspond directly to Γ changes at IE. q_o-values (due to the double layer charging) are determined in $M^{z+}_{(aq)}$ ion-free solutions. From independent $q(E, \mu_{M^{z+}_{(aq)}})$ and $\Gamma(E, \mu_{M^{z+}_{(aq)}})$ measurements, the electrosorption valency[4] can be directly determined from Δq–Γ plots with $\Delta q = q - q_o$. In the absence of specific adsorption, q_o is relatively small, and it can be assumed that γ_v (electrosorption valency) $\to z$. In contrast, if cosorption or competitive sorption processes occur in parallel with M upd at the interphase, then $\gamma_v \neq z$ gives information about the coupling between q_o and Γ.

Figure 2.11a, b show the cyclic voltammogram for Ag upd on Au(111) in sulfate solutions and the Γ–ΔE isotherm determined by the TTL-technique over the entire upd range studied, respectively [13]. A charge density of approximately 130 μC cm^{-2} is obtained for the first upd peak corresponding to a coverage of $\theta_{Ag} \approx 0.58$. A total charge of about $zF\Gamma \approx 160 \pm 5$ μC cm^{-2} at $\Delta E = 20$ mV was experimentally found, which does not correspond to the theoretical value for a complete Ag monolayer ($zF\Gamma = 222$ μC cm^{-2}). This fact may be attributed to additional adsorption of Ag in the upd ranges $0 \leq \Delta E(\mathrm{mV}) \leq 20$ and $\Delta E > 720$ mV.

For the same system, the Δq–Γ plot (Fig. 2.12) gives a value of $\gamma_v = z = 1$, suggesting the absence of anion cosorption or competitive sorption phenomena. However, Ag upd on Au(111) takes place at more positive potential values than the potentials of zero charge of Au(111) ($E^{Au(111)}_{PZC} = 470$ mV) and Ag(111) ($E^{Ag(111)}_{PZC} = -478$ mV) surfaces [64–66], therefore the presence of adsorbed anions cannot be excluded. A mechanism proposed by Gewirth et al. [15] for the Ag upd phenomenon is that Ag must penetrate the anion layer in order to approach the Au(111) surface, while this anion layer remains and is also present after Ag adatom formation.

A similar analysis was performed for the system Au(100)/Ag$^+$, SO_4^{2-} [13]. Figure 2.1a shows the cyclic voltammogram of this system. The Γ–ΔE isotherm measured under TTL-conditions (Fig. 2.13) indicates a stepwise formation of the Ag monolayer, in agreement with the voltammetric behavior. A value of $zF\Gamma \approx 80$ μC cm^{-2} is obtained for the first Ag upd peak, corresponding to a coverage of $\theta_{Ag} \approx 0.42$. At $\Delta E = 20$ mV, the experimental value of $zF\Gamma \approx 160$ μC cm^{-2} is significantly smaller than the theoretical one for a complete

---

[4] The concept of electrosorption valency $\gamma_v = \frac{1}{F}\left(\frac{\partial q}{\partial \Gamma}\right)_E$ is discussed in detail in Chap. 3. In the case that upd involves a straightforward full discharge of the corresponding cation, its value is equal to its valency.

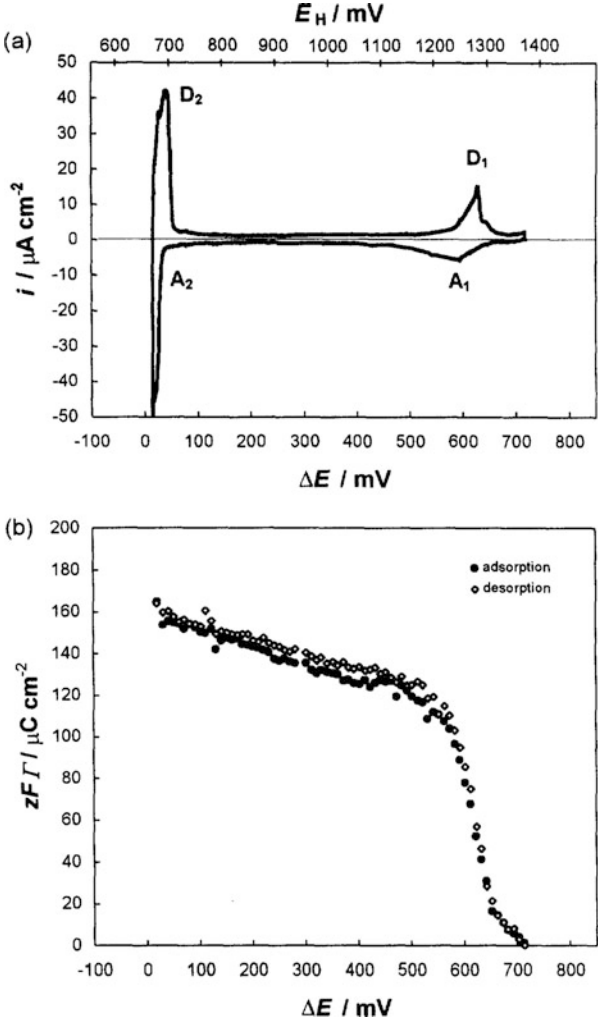

Fig. 2.11 (**a**) Cyclic voltammogram for the upd of Ag in 5×10^{-3} M $Ag_2SO_4 + 0.5$ M H_2SO_4 solution on Au(111) substrate. A_n and D_n with $n = 1, 2$ denote cathodic adsorption and anodic desorption peaks, respectively. $|dE/dt| = 7$ mV s^{-1}, (**b**) $\Gamma(E)$ isotherm measured under TTL conditions in the system Au(111)/ 4.5×10^{-5} M $Ag_2SO_4 + 0.5$ M H_2SO_4. $T = 298$ K (Reprinted with permission from Ref. [13])

Au(100)−(1 × 1) Ag monolayer (192 μC cm^{-2}). The authors attributed this difference to an additional Ag adsorption in the potential ranges $0 \leq \Delta E(\mathrm{mV}) \leq 20$ and $\Delta E > 720$ mV.

Similarly to the previous system, Au(111)/ Ag^+, SO_4^{2-}, the electrosorption valency measurements with the Au(100) susbtrate (Fig. 2.14) show $\gamma_v = z = 1$, indicating that coadsorption or competitive adsorption of anions can be excluded. However, taking into account the potentials of zero charge of Au(100) ($E_{PZC}^{Au(100)} = 240$ mV) and Ag(100) ($E_{PZC}^{Ag(100)} = -648$ mV) [64–66], it could also happen that a nearly constant anion layer may be present during Ag upd.

Fig. 2.12 Determination of the electrosorption valency, γ_v, from independent Δq and Γ measurements obtained by TTL technique. System: Au(111)/ 4.5×10^{-5} M $Ag_2SO_4 + 0.5$ M H_2SO_4. $T = 298$ K (Reprinted with permission from Ref. [13])

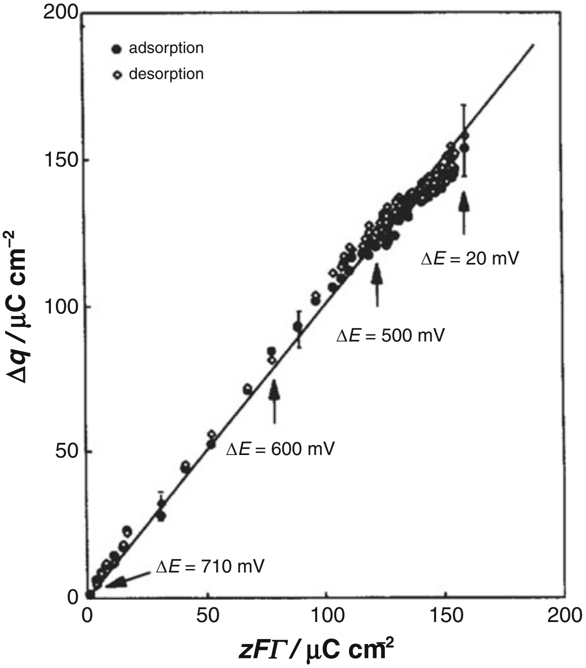

Fig. 2.13 $\Gamma(E)$ isotherm measured under TTL conditions in the system Au(100)/4.2×10^{-4} M $Ag_2SO_4 + 0.5$ M H_2SO_4. $T = 298$ K. These isotherms correspond to the voltammetric profile shown in Fig. 2.1a (Reprinted with permission from Ref. [13])

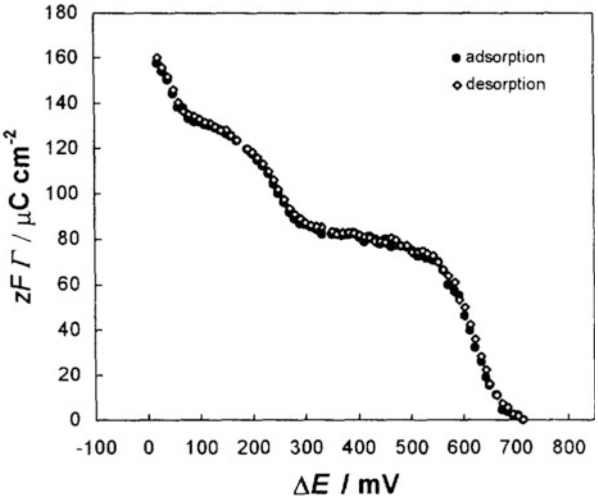

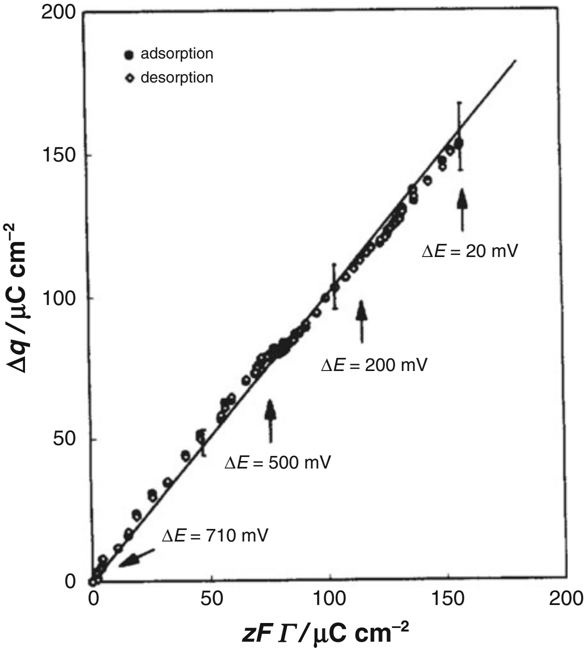

Fig. 2.14 Determination of the electrosorption valency, γ_v, from independent Δq and Γ measurements obtained by the TTL technique. System: Au(100)/ 4.2×10^{-4} M $Ag_2SO_4 + 0.5$ M H_2SO_4. $T = 298$ K (Reprinted with permission from Ref [13])

2.7 Rotating Ring Disk Electrode

The Rotating Ring-Disk Electrode (RRDE) technique has also been used to study the upd phenomenon. In the late 1960s and early 1970s, Bruckenstein and coworkers [67–70] proved that this method was a powerful and useful tool to study adsorption processes at solid electrodes. Its main advantage is the well characterized and controlled mass transfer to the electrode through forced convection induced by electrode rotation which allows, in many cases, an easy separation and identification of mass transfer and intrinsic electrode kinetic controlling effects.

The RRDE is a disk electrode around which is placed an insulating gap made of Teflon, polyethylene or epoxy resin. A ring electrode is placed around the disk in a centrally symmetrical position. This geometry permits precise hydrodynamic control of the flux of material to and from a reacting surface. The preparation of ring-disk electrodes as well as the rigorous theory describing their behaviour together with some practical applications are described by Opekar and Beran [71].

Two types of experiments can be performed with a RRDE: collection experiments (the most common), where the species generated at the disk are detected at the ring, and shielding experiments, where the flow of bulk electroactive species to the ring is perturbed due to reaction on the disk [71, 72]. The applications of the first type of experiments to upd are explained in more detail here.

The amount of upd species deposited on the disc can be estimated using the collection mode, where the disc acts as the generator while the ring acts as the collector [73, 74]. In this case, the ring potential is held at a sufficiently cathodic potential value, which allows the massive deposition of the metal ions. When the surface of the ring is totally covered by the metal, the current stabilizes and reaches a constant value, dependent on the rotation rate, which is considered as the baseline. Then, the disc is polarized either by potential scanning or by a potentiostatic pulse to a proper potential for the deposition of one monolayer of the metal. After that, the disc potential is scanned in the positive direction to dissolve the formed monolayer. The increase of metal ions in the diffusion layer is detected as a rise in the ring current, which returns to its initial constant value after total dissolution of the monolayer. The current variation at the ring can be used to estimate the charge due solely to monolayer dissolution without any influence of surface oxidation.

Bruckenstein and coworkers have contributed a great deal to the practical application of the RRDE. They studied the kinetics and the voltammetric properties of several systems such as Pt/Cu^{2+} [68, 69], Pt/Bi^{2+} [75], Au/Pb^{2+} [76], Au/Ag^{+} [77], Au/Hg^{2+} [78], between others.

This technique has been used to separate the upd mass flux from the charge flux and thus thermodynamic data can be obtain independently from kinetic and double layer effects [73]. It can be employed to obtain both equilibrium and dynamic properties for low concentrations of depositing ions ($\leq 10^{-4}$ M). In order to obtain accurate results, other conditions are needed: the chemical nature of the ring electrode must be the same as that of the upd metal deposited on the disc, therefore plating the ring with at least ten layers of the upd metal is required; suitable rotation speed (lower rotation speeds at the higher concentrations); sufficiently negative ring electrode potential in order to ensure convective-diffusion controlled reduction of the upd species in solution at the ring electrode.

Machado and coworkers [79] have used cyclic voltammetry at stationary and rotating ring-disk electrodes in order to analyze the underpotential deposition of Cu and Ag on polycrystalline Au surfaces from sulphuric acid solutions. The charge densities obtained by the later technique were calculated by the collection mode. For a better understanding, their own voltammetric results are also presented here. Figure 2.15 exhibits the voltammetric response of the Au surface (stationary electrode) in Cu^{2+} containing solution, when holding the potential scan at 0 V vs RHE during 300 s to allow Cu deposition on the electrode surface, together with the steady state profile of the blank solution. Peak 4 is related to bulk Cu dissolution and peaks 1–3 represent the upd Cu profile. The sum of the charge densities calculated for the three upd Cu peaks reaches 405 $\mu C\ cm^{-2}$. The RRDE was used to separate charge and mass fluxes, allowing to estimate the charge on the disk due solely to the metal deposition reaction. The total charge values obtained for the redissolution of the submonolayers using different deposition times are shown in Table 2.1, where the charges were evaluated by two methods. In the first one, the voltammetric peaks during the potential scan on the disk were integrated to obtain the oxidation charge values. In the second method,

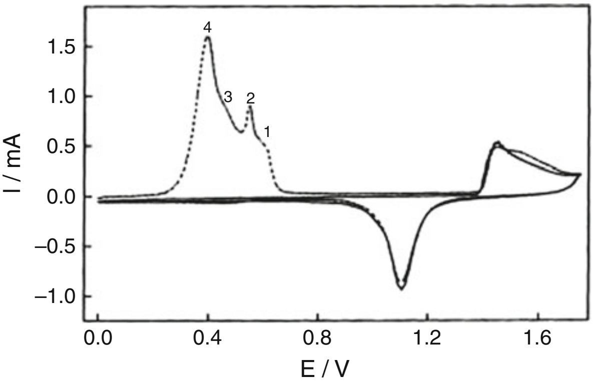

Fig. 2.15 Steady-state voltammetric response for the system Au/0.5 M H_2SO_4 at 1 V s^{-1} (*continuous line*) and first cycle voltammogram obtained after the addition of 5×10^{-5} M $CuSO_4$ and holding at 0 V for 300 s (*dotted line*) (Reprinted with permission from Ref. [79])

Table 2.1 Dissolution charges densities obtained for Cu upd from the two methods described in the text: cyclic voltammetry and RRDE. Cu was deposited at 0.17 V during several time intervals

T_{dep}(s)	$q^{(v)}_{disk}$ (μC cm^{-2})	$q^{(R)}_{disk}$ (μC cm^{-2})
0	26	28
10	53	57
20	91	96
60	135	146
90	233	244
120	292	304
300	322	326
600	376	374
1200	385	386

$q^{(v)}_{disk}$, disk charges calculated by the voltammetric peaks of the disk response; $q^{(R)}_{disk}$ disk charges calculated through the variation of ring currents

Reedited with permission from Ref. [79]

current variations observed on the ring were associated solely with the amount of Cu^{2+} which leaves the disk surface generating an increase in the ring deposition current and with the ring current after the whole Cd ML was dissolved on the disk. Both results show a good agreement between the values found using the two procedures, i.e. 386 μC cm^{-2}.

Comparing the results of charge density values related to the oxidation of a complete Cu upd monolayer, from stationary (405 μC cm^{-2}) and rotating ring-disk electrodes (386 μC cm^{-2}), very close to the theoretical value of 390 μC cm^{-2}, the authors suggested an epitaxial deposition of Cu on polycrystalline Au in a two-electron reduction process.

The same authors also investigated the Ag/Au system. The voltammetric response of the Au electrode in the solution containing Ag^+ ions is presented in Fig. 2.16, after holding the potential scan at 0.5 V vs RHE during 600 s to allow Ag monolayer deposition on the electrode surface, together with the steady state profile

Fig. 2.16 Steady-state voltammetric response for the system Au/ 0.5 M H_2SO_4 at 0.5 V s^{-1} (*continuous line*) and first cycle voltammogram obtained after the addition of 5.6×10^{-5} M $AgNO_3$ and holding the potential scan at 0.5 V for 600 s (*dotted line*) (Reprinted with permission from Ref. [79])

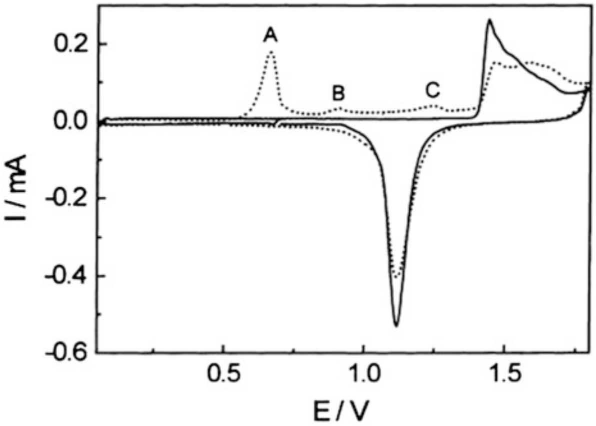

of the blank solution. Peaks B and C correspond to the dissolution of Ag upd, while the peak A is related to the bulk Ag phase. As it is shown, Ag upd occurs at a more positive potential range than that of Cu, indicating that the oxidation of the Au surface is affected by the presence of the adsorbed Ag layer. For this reason it becomes difficult to determine the charge density for a full Ag monolayer, mainly due to the possible overlapping of the Ag upd peak with Au oxidation. The authors found a value of 108 μC cm^{-2}, which corresponds approximately to half a monolayer of Ag adatoms.

The RRDE measurements, which allowed to separate the oxidation charge of the monolayer from that associated to Au oxidation, indicated a value of 115 μC cm^{-2}, also in agreement with that required for a half monolayer. This deposition mode is different from the Cu/Au system and the authors concluded that co-adsorption of sulfate or hydroxide anions hinder the formation of a full monolayer of Ag on polycrystalline Au.

Jüttner et al. have used cyclic voltammetry, charge isotherms and RRDE methods to analyze the upd of Cu on Au(111) surfaces in sulphuric acid solutions of different Cu^{2+} concentrations [24]. From the voltammetric measurements and charge isotherms, they concluded that the ideal metal-monolayer model was valid at low underpotentials at a high degree of adatom coverage, since the electrosorption valency γ_v is equal to the valence number z, i.e. $\gamma_v = z = 2$, indicating a full M discharge. The formation of Cu^+ ions and co-adsorption of sulfate ions produced significant deviation from the ideal behaviour ($\gamma_v \sim 1$) at higher underpotentials, where the $(\sqrt{3} \times \sqrt{3})R30°$ structure was present. The authors explained this behaviour in terms of a partial discharge of Cu^{2+} to Cu^+, the adsorption of which was stabilized by co-adsorption with sulfate ions. Charge-transfer controlled formation of Cu^+ at the interface as a reaction intermediate was detected in the transition range of underpotential and overpotential copper deposition using the RRDE measurement technique.

2.8 Electrochemical Quartz Crystal Microbalance

The electrochemical quartz crystal microbalance (EQCM) is one of the most sensitive electrochemical techniques and is particularly well suited to study underpotential deposition of metallic layers on a gold coated crystal. The technique has now become a valuable procedure in electrochemical surface science, complementary to charge evaluation procedures such as cyclic voltammetry and chronoamperometry. Usually, simultaneous cyclic voltammetry and EQCM experiments have been used in order to determine the corresponding variations of the faradaic charge and mass during the deposition process.

Immersion of a quartz crystal oscillator in an electrolyte solution, with simultaneous control of the applied potential of the overlaying metallic film enables simultaneous and in-situ determination of the mass variation in relation to surface charge density associated with an electrosorption or electrodeposition process. This system is sensitive enough to detect the presence of submonolayer amounts of species on the surface, i.e. it is capable of weighing a change of mass in the charge density on the electrode surface, together with the simultaneous measurement of electric charge. Thus, the EQCM may provide information of the quantities of two species, such as adatoms and adsorbed anions, as a function of electrode potential.

The first studies on upd using a quarzt crystal microbalance (QCM) were performed by Bruckenstein and Swathirajan [80], who analysed the underpotential deposition of lead and silver on polycrystalline gold in acetonitrile. In this case, they generated the monolayer deposits on the QCM and made ex-situ mass determinations. This method consisted on measurements of the resonance frequency of a piezoelectric quartz crystal upon whose faces gold electrodes had been deposited, and the crystal frequency changed as upd species were deposited. The surface coverages of underpotentially deposited species were calculated through the relation derived by Sauerbrey [81] between the frequency change of the oscillating quartz crystal and the change of the attached mass. They found a good agreement between these results and those obtained by the rotating ring disk (Ag) and rotating disk (Pb) techniques.

Later on, Bruckenstein and Shay published an important contribution on the experimental aspects of use of the QCM in solution [82] and Melroy et al. [83] were the first who evaluated in situ Pb upd deposits on Au electrodes by the EQCM technique. They obtained the electrosorption valency (γ_v) for Pb deposition onto Au, which was in good agreement with literature values, indicating the capabilities of the EQCM to be used in situ for measurement of monolayer mass changes.

Continuing on the study of upd processes with the EQCM, Deakin and Melroy [84] reported results related to the upd of several metals (Pb, Bi, Cu, and Cd) on polycrystalline Au in 0.1 M $HClO_4$. The coverages of the M upd layer on the Au surface were calculated from the frequency change of the QCM as a function of potential, and where in good agreement with previous values obtained using other techniques. The electrosorption valencies were calculated from the slope of the charge versus coverage plots, which provide a sensitive measure of γ_v at any potential.

It must be pointed out that adsorbed anions may produce significant responses in the EQCM frequency changes [85] and therefore, they should be considered in the interpretation of mass changes observed in the processes of monolayer formation.

The present method was used to study the formation of copper and silver adatoms on Au(111) electrodes [16, 86, 87] and was found to provide useful information on upd processes, complementing results obtained by other techniques.

Ikeda et al. [86] showed that copper adatoms formed in the first and second upd processes on Au(111) in sulphuric acid solution are close to 2/3 of one monolayer and one monolayer respectively, and that the ratios of hydrated bisulfate anions to Cu adatoms are approximately 0.5 and 0.3, at the corresponding Cu coverages.

In a later work [87], it was found that perchlorate anions are specifically adsorbed on Au(111) and that the Cu adatoms on the surface cause an enhanced coadsorption of both sulfate and perchlorate anions. Figure 2.17 shows the cyclic voltammograms for Au(111) electrodes in both solutions and the corresponding coverages of Cu as well as those of anions. The deposition and dissolution phenomena of Cu in 0.1 M $HClO_4$ consisted of a two-stage deposition process characterized by S_1 and P_2 peaks, and the corresponding dissolution was characterized by P'_{2A}, P'_{2B} and P'_1 peaks (Fig. 2.17a). This voltammetric behaviour was different from that observed in 0.05 M H_2SO_4, which consisted of two sharp cathodic peaks (P_1 and P_2) and the corresponding anodic peaks (P'_2 and P'_1). The composition of the Cu adlayer (θ_{Cu} and θ_{anion}, coverages of Cu adatoms and coadsorbed anions respectively) during its formation or removal as a function of potential was determined and shown in Fig. 2.17b, c. The coverages of both anions on a Cu-free Au(111) surface, which are also exhibited in Fig. 2.17c, decrease monotonically when the potential is changed to more negative values. For the first Cu upd region, the reversible anodic and cathodic peaks of the voltammogram correspond well to the reversible changes in θ_{Cu} and θ_{anion}, producing in this deposition stage an enhancement of anion adsorption. The authors showed that the maximum HSO_4^- anion coverage when $\theta_{Cu} \sim 0.66$, led to a ratio $\theta_{Cu}/\theta_{anion} \sim 2$ (Fig. 2.17d), indicating a good agreement with the ($\sqrt{3} \times \sqrt{3}$) structure determined for the first Cu upd layer in H_2SO_4 solution by various methods [27, 38, 88, 89]. On the other hand, the weakly adsorbed ClO_4^- adsorbates (represented by a broad shoulder S_1) rearranged continuously and therefore no ordered structure was reported. In contrast, asymmetric features of the voltammograms for the second Cu upd region in H_2SO_4 and for the whole process in $HClO_4$ correlated with a large hysteresis in changes of θ_{Cu} and θ_{anion}, probably originating from a slow rearrangement of both species. The authors attributed these differences to the strong adsorption of HSO_4^- and the weak one or mobility of ClO_4^-.

Uchida et al. [16] discussed quantitatively the composition of the Ag adlayer on Au(111) in H_2SO_4 solution including Ag adatoms and coadsorbed anions, employing the EQCM. They pursued to clarify the relation between the amount of Ag adatoms and that of adsorbed hydrated anions during the formation and

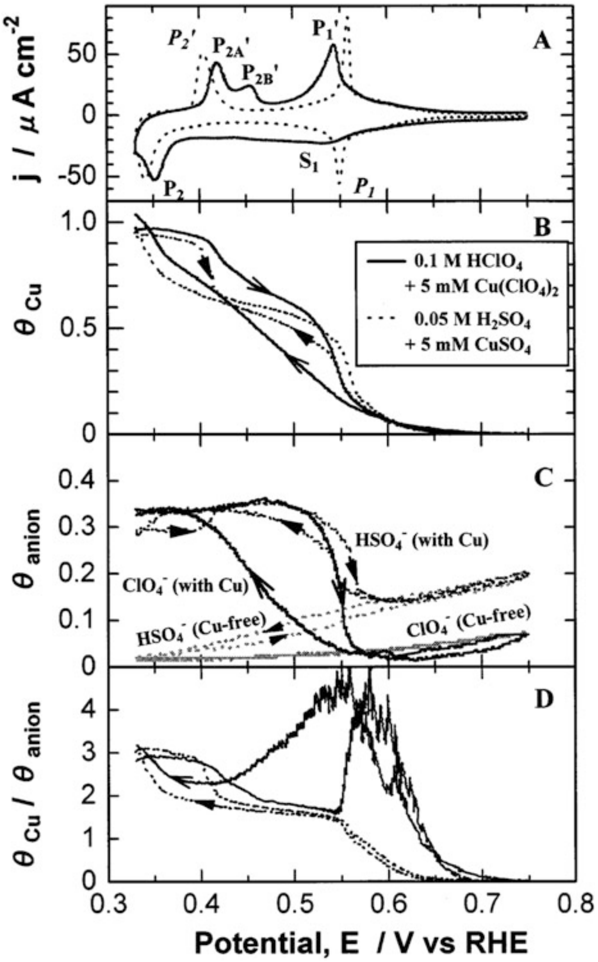

Fig. 2.17 (**a**) Cyclic voltammogram of the system Au(111)/0.1 M $HClO_4$ + 5 mM $Cu(ClO_4)_2$ (*solid line*) and Au(111)/0.05 M H_2SO_4 + 5 mM $CuSO_4$; (**b**) changes in the coverage of Cu adatoms, θ_{Cu}; (**c**) changes in the coverage of anions, θ_{anion}. θ_{anion} for Cu-free Au(111) are shown by grey curves; (**d**) changes in the molar ratio $\theta_{Cu}/\theta_{anion}$. The results of (**b**), (**c**) and (**d**) stemm from EQCM measurements (Reprinted with permission from Ref. [87])

removal of a Ag adlayer. They suggested that the formation of the first Ag upd structure began accompanied with the desorption of anions, where the Ag adatoms were deposited at vacant sites through a “template” of adsorbed bisulfate, while in the region between the first and second upd peaks, bisulfate anions tended to desorb from the Ag-free Au(111) surface. However, they found that a large amount of anions was adsorbed on the Ag adlayer on Au(111). They suggested that a rearrangement of adsorbed anions may occur at the surface resulting in, for example, an adsorption of anions on top of Ag adatoms, as proposed by an EXAFS study [90]. At the potential close to bulk deposition, the coverage of Ag increases to one monolayer, corresponding to the formation of the first close-packed Ag adlayer on Au(111). Therefore, this process involved the rearrangement of Ag atoms and adsorbed anions and the substitution of the later by Ag adatoms.

More recently, Inzelt and Horányi [91] showed that the EQCM can be also used to study alloy formation in the course of Cd upd on gold from $HClO_4$ supporting electrolyte. The alloy formation/dissolution processes produced the roughening of the surface, which was reflected by an increase in the total amount of adsorbed anions and adatoms, resulting in frequency changes.

2.9 Scanning Probe Microscopy

A detailed understanding of the mechanisms by which electrochemical phase formation processes take place cannot be achieved with purely electrochemical methods, but requires local information on the structural, chemical and morphological properties of the interface at the atomic scale. The analysis of the initial steps of metal phase formation has strongly benefited from the advent of the Scanning Probe Microscopy (SPM) techniques, such as Scanning Tunneling Microscopy (STM) and Atomic Force Microscopy (AFM), allowing the visualization of the deposit morphology at the atomic scale. Indeed, studies of many upd systems performed previously by conventional electrochemical techniques to evaluate thermodynamics and kinetics, were complemented by structural information of upd layers obtained by in situ STM and AFM techniques. These high-resolution microscopies have similar components but different sensing probes, and therefore various types of interaction of the tip with the surface are exploited in the different types of probe microscopes.

2.9.1 Scanning Tunneling Microscopy

Binnig and Rohrer developed the STM operating in ultrahigh vacuum in 1981 [92, 93] and later, in 1986, Sonnenfeld and Hansma demonstrated for the first time that it could be employed in electrolyte solutions [94]. This aspect is highly important since the interfacial environment of the electrochemical processes does not appear to be essentially disturbed during the structural imaging. Several works refer to the use of this technique in electrochemical systems [95–99]. In situ STM has been widely used as a powerful tool for exploring the structure of M adlayers, providing valuable insight into metal phase formation processes of different dimensionality at an atomic level. With this technique, the growth morphology of metal deposits can be followed from isolated atoms to connected films.

The most important feature of in situ STM is real-space visualization under reaction conditions of bare and adsorbate-covered surfaces at the atomic scale. This provides data on the structure of upd layers as a function of coverage, on the reconstruction and modification of the substrate caused by the electrodeposited species, on the formation of surface alloys, on possible epitaxial correlations between 2D and 3D phases, and on the mechanisms involved in all these processes.

STM is based on the phenomenon of quantum mechanical tunnelling. A sharp metal tip, often made of Pt, W or Pt-Ir, is brought close ($\leq$10 Å) to the planar sample surface via a controlled approach piezo-electric motor. When the two surfaces are close enough so that their wave functions overlap, a finite probability exists that electrons will cross the barrier between the surfaces when a bias is applied between the sample and tip. The resulting tunnelling current I_{tun}, depends sensitively on the distance between tip and surface, and can be expressed by:

$$I_{\mathrm{tun}} \approx D_{\mathrm{S}}(E_{\mathrm{F,S}}) D_{\mathrm{T}}(E_{\mathrm{F,T}}) V_{\mathrm{b}} \exp[-2\kappa d] \tag{2.1}$$

where $D_{\mathrm{S}}(E_{\mathrm{F,S}})$ and $D_{\mathrm{T}}(E_{\mathrm{F,T}})$ are the density of states of the sample and tip at their respective Fermi level energies, d is the tip-sample separation, V_{b} is the bias voltage, i.e. the applied voltage difference between sample and tip, and the exponential term is the probability of tunnelling through the potential barrier [100], with κ given by:

$$\kappa \approx \left[2 m_{\mathrm{e}} \overline{\phi} / \hbar^2\right]^{1/2} \tag{2.2}$$

where m_{e} is the electron mass, $\overline{\phi}$ is the mean of the tip and sample barrier heights, and $\hbar = h/2\pi$, where h is Planck constant. Equation (2.1) is an oversimplification but sufficiently explains the operation of the instrument. The high sensitivity of the instrument, which can attain a vertical resolution of a few 0.01 nm is attributable to the strongly non linear dependence of the tunneling current on the distance between the tip and the surface.

The STM can be operated in two modes to produce images. The sample surface can be mapped in the *constant current mode* by recording the feedback-controlled motion of the tip up and down, such that a constant tunneling current is maintained at each x-y position. The structure can also be mapped in the *constant height mode* by recording the modulation of the tunneling current as a function of position, while the tip remains at a constant height above the surface. The later mode is preferred for atomic-scale images but it can only be used on very smooth surfaces. The former is required to obtain topographic images of relatively rough surfaces.

For in situ electrochemical experiments, the STM tip surface exposed to the electrolyte must be insulated by coating all but its very end with an insulator (soft glass, APIEZON wax, polymers) so that the tunneling current will not be overcome by the electrochemical background current (faradaic current) flowing through the tip. Lateral atomic resolution at metal surfaces in the electrolyte may only be achieved with optimum tunneling tips, combining ideal tip geometry with an excellent quality of the lateral tip insulation. The microscope must be coupled with a bipotentiostat, which allows that the potential of the substrate and the tip can be varied independently with respect to a reference electrode [101]. The principal limitation of the STM is that it cannot be used for non conducting samples.

An illustrative example of a surface topography showing an in situ STM image of an electrochemically polished Au(111) surface, under potentiostatic control,

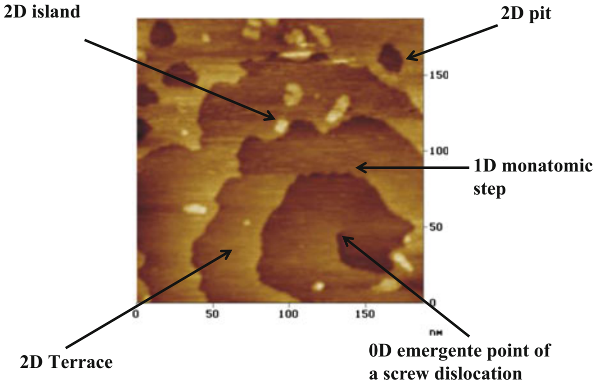

Fig. 2.18 Example of an in situ STM image showing surface defects of an electrochemically polished Au(111) surface in the system Au(111)/ 5×10^{-3} M $AgClO_4 + 0.5$ M $HClO_4$ at $E = 200$ mV (vs Ag/Ag^+ Nernst equilibrium potential). $T = 298$ K (Reprinted with permission from Ref. [13])

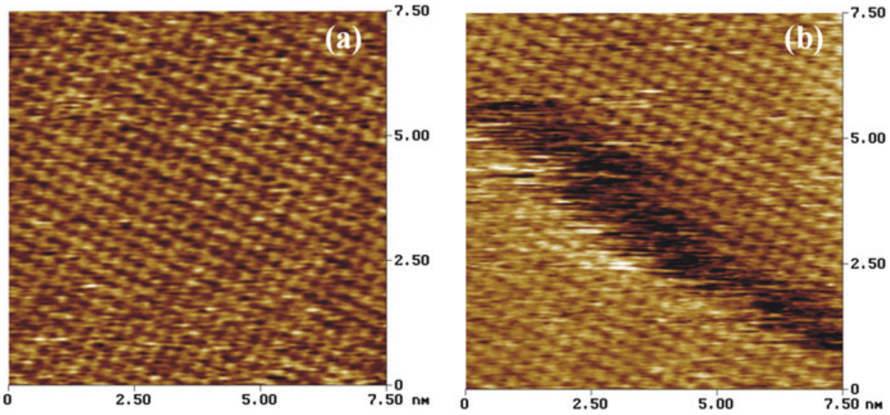

Fig. 2.19 Examples of in situ STM images with atomic resolution of an electrochemically polished Au(100) surface in 0.5 M $HClO_4$ at $E = 750$ mV (vs reversible hydrogen electrode). (**a**) on a terrace (**b**) on two terraces separated by a monatomic step. $T = 298$ K

with different inhomogenities is presented in Fig. 2.18. 1D monatomic steps, 0D emergence point of a screw dislocation, 2D pits, etc., are surface defects that can be directly observed by STM and play an important role in the formation of low dimensional M phases in the upd range.

On the other hand, Fig. 2.19a illustrates an example of in situ STM imaging of a Au(100) surface in perchlorate electrolyte with lateral atomic resolution. A quadratic structure with an average interatomic distance of $d_{o,Au} = 2.8 \pm 0.1$ Å can be observed, which is in good agreement with crystallographic data of $d_{o,Au} = 2.8840$ Å [12] and previous in situ STM images [102]. Figure 2.19b shows the atomic structure of two Au terraces separated by a monatomic step which looks frazzled in STM images. This phenomenon has also been observed at the edges of Cu islands deposited on Ag(111) [103] and has been interpreted as being due to the movement of kink sites on steps edges and, as a consequence of this movement, the STM tip finds the location of a step edge always at slightly different positions for each scan line [104, 105].

The Ag upd process on Au has also been studied by in situ STM in different electrolytes by various authors. In particular, Itaya et al. [17, 106, 107] found for annealed Au(111) substrates expanded and commensurate Au(111)−(√3 × √3)R30° Ag and Au(111)−(4 × 4)Ag structures at relatively high underpotentials in sulphuric and perchloric acid solutions, respectively. At low underpotentials, a condensed commensurate Au(111)−(1 × 1)Ag overlayer was observed in both solutions. Gewirth et al. [14, 108] used in situ AFM, which will be addressed later, together with cyclic voltammetry to study the underpotentially deposited monolayers of Ag on Au(111) surfaces in different electrolytes. In this case the working electrode was a Au film evaporated onto mica. These authors recognized a strong anion influence on the overlayer structure and found the following structures depending on the nature of the electrolyte: Au(111)−(3 × 3)Ag (sulfate), Au (111)−(4 × 4)Ag (nitrate), Au(111)−(1 × 1)Ag (acetate) and an unassigned open structure (perchlorate). The results of Itaya and Gewirth do not agree in sulfate media. García et al. [13], using mechanically and electrochemically polished Au (111) substrates in sulfate and perchlorate solutions, found a Au(111)−(4 × 4)Ag structure. The theoretical charge for this adlayer is $zF\Gamma = 125$ μC cm^{-2} ($\theta_{\mathrm{Ag}} = 0.56$) which is in good agreement with the experimental value of $zF\Gamma = 130 \pm 5$ μC cm^{-2} for the first Ag upd peak obtained by TTL-measurements. A Ag(1 × 1) structure was imaged at low underpotentials in concordance with all the authors. Later on, the in situ STM images of underpotentially deposited Ag on flame-annealed Au(111) electrodes obtained by Kolb et al. [109], revealed a series of ordered adlayer structures of increasing coverage with decreasing potential, namely (√3 × √3)R30°, a distorted hexagonal stripe pattern and a (3 × 3) before a close-packed (1 × 1) layer.

Changes in the atomic structures of Ag upd on Au(100) were studied by in situ STM with lateral atomic resolution in sulfate and perchlorate solutions [13]. In both cases, a quadratic structure with an interatomic spacing of $d_{\mathrm{o,Au}} = 0.29 \pm 0.01$ nm was observed at relatively high underpotentials, e.g. $\Delta E = 650$ mV, corresponding to the bare and unreconstructed Au(100) surface (Fig. 2.20a). At lower underpotentials, between the adsorption peaks A_1 and A_2 of the cyclic voltammograms (cf. Fig. 2.1a), different domains with a well ordered expanded quasi-hex Ag structure on Au(100) terraces were formed (Fig. 2.20b), that was observed in both solutions.

This expanded structure is better seen in Fig. 2.21a and could be described as a Au(100)-c(√2 × 5√2)R45° Ag superstructure according to the model in Fig. 2.21b.

The average distance between the nearest neighbour Ag atoms was $d_1 = 4.1 \pm 0.1$ Å. This expanded quasi-hex structure was also reported by Ikemiya

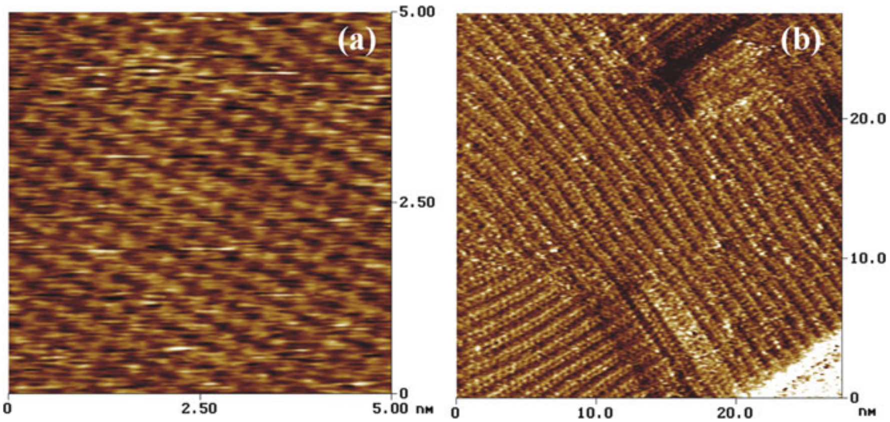

Fig. 2.20 In situ STM images with lateral atomic resolution in the system Au(100)/ 5×10^{-3} M $AgClO_4 + 0.5$ M $HClO_4$ at $T = 298$ K, (a) $E = 650$ mV, (b) $E = 450$ mV (vs Ag/Ag^+ Nernst equilibrium potential) (Reproduced with permission from Ref. [13])

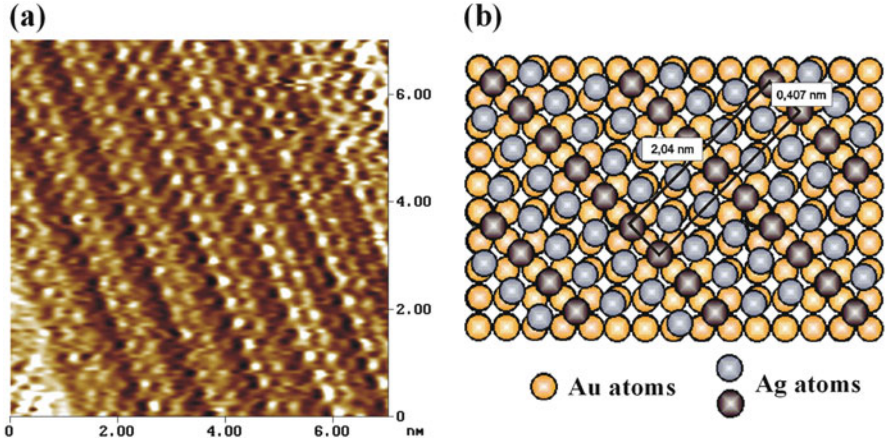

Fig. 2.21 (**a**) In situ STM image of the Au(100)-c(√2 × 5√2)R45° Ag superstructure at a higher magnification, (**b**) schematic representation of the overlayer structure (Reproduced with permission from Ref. [13])

et al. using in situ AFM [110]. The theoretical charge value for this expanded superstructure is $zF\Gamma = 115$ μC cm^{-2}, whereas the experimental value was $zF\Gamma = 80$ μC cm^{-2} [13, 111]. The authors ascribed this difference to the onset of Ag upd on Au(100) already at $\Delta E > 720$ mV interfering with oxygen adsorption and Ikemiya suggested that this discrepancy was caused by a partial discharge of Ag adatoms but such a claim could not be confirmed from simple charge measurements [1]. On the other hand, the expanded Ag structure correlated well with the Γ found, and therefore it appears that it was not stabilized by coadsorbed anions as it is the case of the Au(111)-($\sqrt{3} \times \sqrt{3}$)R30° Cu structure [112], although a cosorption of anions in the Ag upd range could not be excluded.

When the electrode potential was further scanned in the cathodic direction, a condensed and commensurate Au(100)-(1 × 1)Ag phase was found. This structure was also observed in other STM work [113], although the authors could not exclude that the (1 × 1) structure arises as a result of alloying, i.e. it could be related to 2D upd Au(100)-(1 × 1)Ag domains or to Au-Ag surface alloy domains, which can coexist due to the onset of an inhomogeneous surface alloy formation process.

The system Au(111)/Cu has been characterized by almost all electrochemical and analytical techniques. The summary of both ex situ and in situ analytical and structural studies on Au(111)/Cu can be found in the review by Herrero et al. [6].

Magnussen et al. [30] obtained the first atomic images for Cu adlayers on Au (111) in a sulfuric acid solution. They found different structures before bulk Cu deposition. The first, at the most positive potentials, was the bare Au(111) surface. The next structure formed, after the first upd peak, was a ($\sqrt{3} \times \sqrt{3}$)R30° adlattice, which transformed into a second phase of (5 × 5) structure. However, subsequent work proposed that the appearance of this structure may be due to chloride contamination [29], suggesting that the upd process is extremely sensitive to anion coadsorption. Finally, a (1 × 1) monolayer was found just prior to bulk deposition. Figure 2.22 shows the cyclic voltammogram of the system Au(111) in 0.05 M H_2SO_4 + 1 mM $CuSO_4$ together with in-situ STM images of the structures found.

Completely different adlayer structures were reported for Cu upd in perchloric or chloride solutions [114, 115]. It was shown that instead of the structure found with sulfate-containing electrolytes, a (5 × 5) structure emerged due to the presence of $C1^-$ ions on the surface. Behm et al. [115] analysed the effect of different amounts of chloride on the adsorption behaviour and adlayer structure in Cu upd on Au(111) in perchloric acid solutions. They showed that, depending on anion concentration and applied potential, two (quasi-) hexagonal adlayer structures – a commensurate (2 × 2) and an incommensurate (5 × 5) structure – with average Cu adatom spacings of 3.3 and 3.67 Å, respectively, were observed. Both structures involved cooperative adsorption of Cu and Cl^-, but the (5 × 5) adlattice predominated in most of the potential range and anion concentrations studied, while the (2 × 2) adlattice became evident at particular potentials and if anion concentration did not exceed 10^{-6} M.

More recently, Sieradski et al. [116] reported new in situ STM structural results for the upd system Au(111)/Cu/$SO_4{}^{2-}$. For some time the structure after the first Cu upd peak was controversial despite different studies that reported a ($\sqrt{3} \times \sqrt{3}$)R30° structure, which was interpreted as a Cu adlayer with a coverage of 0.33. In some cases, this structure was found to transform into a (5 × 5) structure induced by the presence of chloride contamination, as pointed out above. However, EQCM and chronocoulometric results showed that the coverage of Cu at these potentials was 0.67 and that the (bi)sulfate coverage was 0.33. Later on, in situ X-ray scattering measurements [88] led to a new interpretation of the previous STM and AFM

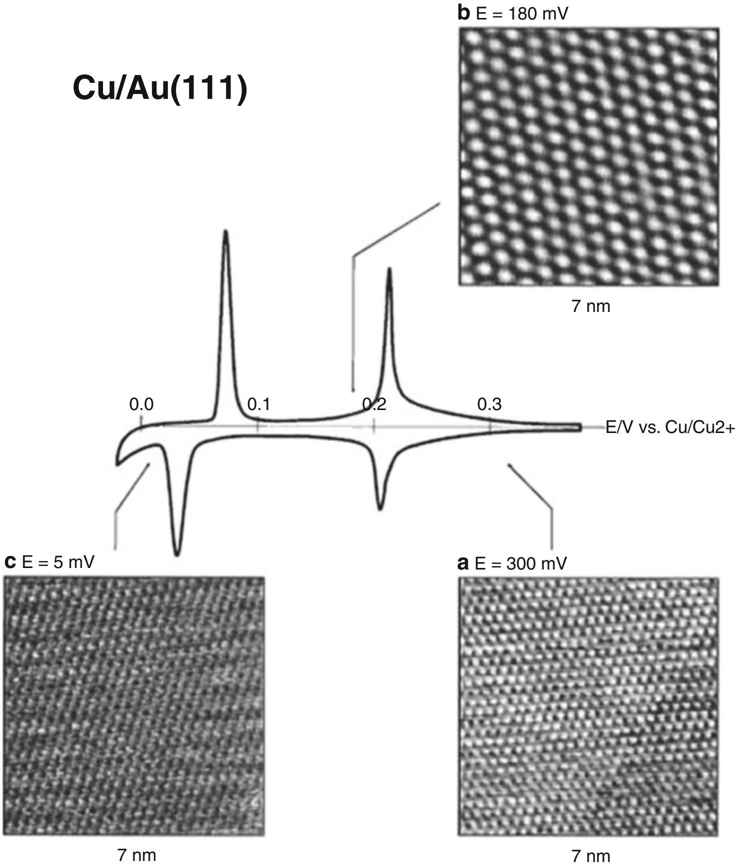

Fig. 2.22 Cyclic voltammogram in the system Au(111)/ 0.05 M $H_2SO_4 + 1$ mM $CuSO_4$ ($|dE/dt| = 5$ mV s^{-1}), and in-situ STM images of the three structures observed at different potentials: (**a**) $E = +0.30$ V, atomic structure of the bare Au(111), (**b**) $E = +0.18$ V, ordered adlayer with the $(\sqrt{3} \times \sqrt{3})R30°$ structure, ascribed to coadsorbed sulfate. (**c**) $E = +0.005$ V, Cu monolayer in registry with Au(111) (Reprinted with permission from Ref. [98])

results, allowing to determine the interfacial structure of the first deposition stage: a honeycomb lattice of Cu atoms (2/3 ML coverage) with sulfate molecules adsorbed in the centers (1/3 ML coverage) above the plane of Cu atoms. Taking into account these X-ray measurements, Sieradski et al. reported not only new structural results for Cu upd on Au(111) but also showed the great capabilities of the in-situ STM technique. In Fig. 2.23, the structure of the Cu layer underneath the sulfate was possible to be imaged by manipulating the tip potential and by switching the sign of the tip bias. Namely, by adjusting the voltage of Au-coated STM tips the authors were able to image the low-density copper honeycomb structure at intermediate underpotentials.

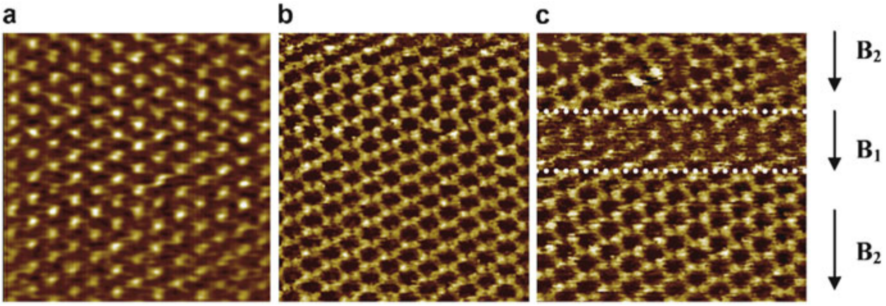

Fig. 2.23 In-situ STM images of the low-density phase in the system Au(111)/1 × 10^{-3} M Cu $(ClO_4)_2$ + 1 × 10^{-3} M $HClO_4$ + 3 × 10^{-2} M Na_2SO_4, at $E = 0.15$ V vs Cu/Cu^{2+} with different bias sign (tip potentials): (**a**) $B_1 = 30$ mV, sulfate (√3 × √3)R30° structure, (**b**) $B_2 = -$ 30 mV, Cu honeycomb structure, (**c**) both structures are observed as the bias is changed during the imaging scan (Reprinted with permission from Ref. [116])

2.9.2 Atomic Force Microscopy

Nowadays, the AFM, invented by Binnig and coworkers in 1986 [117–119] is the most commonly used scanning probe technique for material characterization. The major advantages of AFM are the high resolution in three dimensions and the real space visualization of both conductive and insulating samples surfaces. Therefore, a large range of topographies and many types of materials can be imaged. The latter advantage is due to the fact that AFM, unlike STM, is not based on quantum mechanical tunneling. AFM also uses a sharp tip to map surface morphology, but in this case the feedback mechanism is the force measured between the tip and the sample, not a tunneling current. The force transducer is a deflecting cantilever on which a sharp tip is mounted [120].

This microscope was developed to exploit attractive or repulsive interatomic forces between atoms in the tip and in the substrate, and operates as follows: in order to measure these forces, a sharp tip is mounted on a cantilever made of silicon or silicon nitride (both covered with a native oxide layer of 1–2 nm thickness), which deflects due to forces acting on the tip, and this vertical bending (deflection) is monitored optically by interferometry or beam deflection. That is, the cantilever bending is detected by a laser focused on its back. This laser is reflected by the cantilever onto a distant photodetector. The movement of the laser spot on the photodetector gives an exaggerated measurement of the movement of the tip, which is moved over the sample by a scanner, usually a piezoelectric element [121, 122]. However, in most instruments the sample is generally scanned instead of the tip because any cantilever movement due to scanning would add unwanted vibrations. The measured cantilever deflections are used to generate a map of the surface topography.

AFM has also provided substantial atomic-level insight into the electrode surface structure and into processes occurring on electrode surfaces. Gewirth and coworkers [123] showed for the first time that AFM could be used to investigate electrochemical processes in situ with atomic resolution.

AFM has been used to image surfaces by probing both the attractive and repulsive forces experienced by the tip as a result of its proximity to the sample surface [100]. The most commonly used modes of operation of an AFM are: *contact mode*, *non contact mode* and *tapping mode*. In the first mode of operation, the tip is in physical contact with the surface at all times, then the probe-sample interaction occurs in the repulsive regime and the probe predominately undergoes repulsive van der Waals forces (<0.5 nm probe-surface separation). In the tapping or intermittent mode of imaging, the cantilever is allowed to oscillate at a value close to its resonant frequency. The probe lightly "taps" on the sample surface during scanning, contacting the surface at the bottom of its swing (0.5–2 nm probe-surface separation). In this way, as the probe is scanned across the surface, lateral forces are greatly reduced compared with the contact mode. In the non contact mode, the probe does not touch the sample surface, but oscillates above the adsorbed fluid layer on the surface during scanning, unless the experiment is carried out in a controlled UHV or environmental chamber. The cantilever is again oscillated as in intermittent contact mode, but at much smaller amplitude. As the probe approaches the sample surface, long-range interactions take place between atoms in the probe and the sample, such as attractive van der Waals and electrostatic forces (0.1–10 nm probe-surface separation).

The first study of Ag upd on Au(111) substrates by AFM was reported by Gewirth and coworkers [14]. They recognized different structures for Ag upd depending on the nature of the electrolyte. The AFM images showed a (3×3) structure in sulfate, a (4×4) structure in nitrate and carbonate, an incommensurate structure in perchlorate and a (1×1) structure in acetate containing solutions. The authors demonstrated that the size of the anion affected the structure of the upd adlattice, with larger anions leading to more open structures, and they ascribed this variability to differing repulsive interactions arising from anions coadsorbed with the metal adatoms. The structure of the Ag adlattice on Au(111) in sulfate containing solutions was questioned by STM studies indicating that a $(\sqrt{3} \times \sqrt{3})R30^\circ$ adlattice was formed instead, as was explained above. Other AFM studies revealed also a (3×3) structure, which corresponded to 44 % surface coverage by Ag. This structure was confirmed also by LEED, while ex-situ Auger electron spectroscopy measurements confirmed that sulfate was coadsorbed with Ag [15, 108].

For the system Au(100)/Ag^+ in both $HClO_4$ and H_2SO_4 solutions, AFM studies revealed in the upd region the pseudomorphic (1×1)Ag layer for the first monolayer formed through the $c(\sqrt{2} \times 5\sqrt{2})R45^\circ$ Ag structure ($\theta = 0.6$) [110]. The latter structure was found in both electrolytes, in contrast with the Ag upd adlayers on Au (111) which depended on the anion species being in solution. It was suggested that the upd Ag adlattices on Au(100) were less sensitive to the tetrahedrally shaped anions as compared with the Au(111) surfaces. The expanded and commensurate Ag adlayer Au(100)$-c(\sqrt{2} \times 5\sqrt{2})R45^\circ$ Ag was also observed at relatively high underpotentials by in-situ STM as noted previously [13].

In relation to the Cu upd process on Au(111), the first AFM work was reported by Manne et al. [32], and they demonstrated the sensitivity of the upd adlattice structure

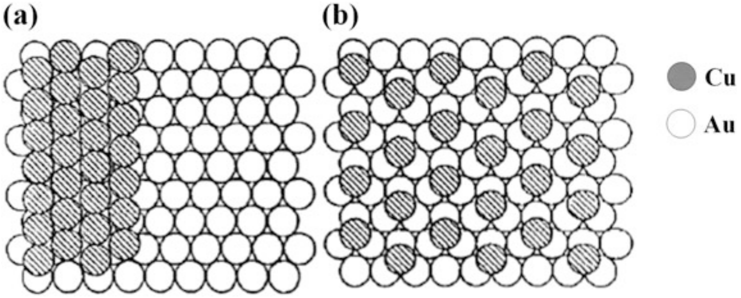

Fig. 2.24 Schematic representation of the Cu adlayer on Au(111) in (**a**) perchlorate solution with only part of the monolayer exhibited, (**b**) sulfate solution showing the (√3 × √3)R30° overlayer structure (Reprinted with permission from Ref. [32])

to anions in solution which become coadsorbed. The Au(111) surface prior to the deposition of Cu in 0.1 M $HClO_4 + 1$ mM $Cu(ClO_4)_2$ as well as in 0.1 M $H_2SO_4 + 1$ mM $CuSO_4$ solutions exhibited the atom-atom spacing of the close-packed Au(111) lattice of 2.9 Å. However, for the first deposited Cu upd layer in a perchloric acid electrolyte, the Cu atoms were in a close-packed lattice with a spacing of 2.9 ± 0. 2 Å, rotated 30º ± 10° relative to gold, i.e. it was not commensurate with the underlying gold lattice. The authors attributed this rearrangement to the strain of incorporating Cu atoms, which show a covalent radius larger than that of Au atoms ($r_{Cu} = 1.75$ Å, $r_{Au} = 1.42$ Å). For a sulfate electrolyte, they were in a more open lattice with a Cu-Cu spacing of 4.9 ± 0.2 Å, with a 30º ± 10° rotation relative to the underlying Au lattice, due to stabilization of the Cu monolayer by coadsorption of SO_4^{2-}. This is equivalent to a (√3 × √3)R30° overlayer structure. The schematic representation of both Cu structures are shown in Fig. 2.24.

2.10 Low-Energy Electron Diffraction, X-Ray Photoelectron Spectroscopy and Auger Electron Spectroscopy

The upd processes of different systems have been also investigated over the years employing several optical methods that often yielded complementary information to that provided by electrochemical analysis and non optical techniques, such as STM and AFM.

Various powerful and well established ex-situ techniques such as low-energy electron diffraction (LEED), X-ray photoelectron spectroscopy (XPS), and Auger electron spectroscopy (AES) are surface-characterization tools which have been used to analize elements and adlattices of thin layers on substrates. Their common feature is the capability of probing the third, in-depth dimension perpendicular to a surface from the nanometer range down to monoatomic layers. However, the fact that the experiments are not carried out in situ because the electrode is removed from the electrochemical cell and transferred into a vacuum environment (UHV chamber), together with the lack of electrode potential control, introduces some uncertainty about the relevance of the data related to the structure actually present at the interface.

LEED is based on the fact that elastically scattered electrons from a monochromatic beam of electrons incident on a surface have a spatial distribution that reflects the underlying symmetry of the surface [124, 125]. The diffracted electrons are registered using a position-sensitive detector and observed as bright spots on a screen. In this method, the energy of bombardment of the sample by electrons is low (20–200 eV) and they are diffracted to produce a pattern unique to each substrate and adsorbed layer. Therefore, it is used to study the structure and morphology of two dimensional planar surfaces. The technique may be used in a qualitative or quantitative way. In the first one, the diffraction pattern is recorded and the analysis of the spot positions gives information on the symmetry of the surface structure. In the presence of an adsorbate, the qualitative analysis may reveal information about the size and rotational alignment of the adsorbate unit cell with respect to the substrate unit cell. In the second way, intensities of diffracted beams are recorded as a function of incident electron beam energy to generate the so-called I-V curves, which through comparison with theoretical curves, may provide accurate information on atomic positions on the surface. It is also important to consider that the size and the local geometry within the surface unit cell can be obtained from the spot positions and intensities, while the spot profile, that is, the shape and width of a diffraction spot, is determined by the long-range relative arrangement of the unit cells at the surface. Vertical displacements of the surface unit cells (steps, facets) lead to splitting of the spots and changes in the spot profile as a function of electron energy [124].

The other method, AES, has widespread use in determining the elemental composition of solid surfaces. The surface to be analysed is irradiated with a beam of electrons of sufficient energy, typically in the range 2–10 keV and, after ionization, the atom can relax by either the ejection of a characteristic X-ray photon or the ejection of an Auger electron [126–128]. In AES, electron bombardment creates a vacancy in the electronic level close to the nucleus. This vacancy is filled by an electron coming from a higher electronic level, and the excess energy is then dissipated through ejection of a secondary electron (an Auger electron). The resulting energy spectrum consists of Auger peaks that are characteristic for each element. That is, as the Auger energy is only a function of atomic energy levels and therefore, each element has its own set of atomic binding energies, an analysis of Auger energies provides elemental identification. For further reading on this technique specific works are indicated [127–129].

The XPS, or electron spectroscopy for chemical analysis (ESCA), is another widely used UHV techniques and can provide complete information on chemical composition and structure both of surface and subsurface layers [130]. The information obtained is related only to surface structures or layers, due to the limited penetration of X-rays into solids (aprox. 5 nm). In this case, X-ray photons are employed to irradiate the sample that causes electron emission (photoelectric effect). These photons interact with electrons close to the nucleus and the energy of these electrons is characteristic of the element and not of the atomic environment. Thus, as the photon energy is related to the binding energy, most elements produce XPS signals with distinct set of binding energies allowing to identify and determine the concentration of the elements on the surface.

Given that the photon energy is greater than the binding energy of the electron to the atom, the electron is then ejected from the atom with a given kinetic energy, which is the quantity measured in the experiment, and the binding energy in a particular level can be determined by subtracting the energy of the incoming photon from the measured kinetic energy of the ejected electron [131, 132]. If the incident photon is sufficiently energetic, many different levels in the sample may be ionized and thus a spectrum is produced showing all accessible energy levels as a distribution of photoelectrons with the corresponding kinetic energies of the emited electrons. It is important to note that variations in the elemental binding energies arise from differences in the chemical potential and polarizability of compounds and therefore, they can be used to identify the chemical state of the materials being analized.

Some examples are presented here, where these three surface analytical probes were used as complementary techniques in studies of upd processes. Gewirth et al. [15] examined Ag upd on Au(111) in dilute sulphuric acid solutions and the possibility of coadsorption of sulfate anions, by electrochemical and ex-situ different techniques, including LEED and AES. A gold single crystal cleaned by Ar^+ ion sputtering and annealed was used in the combined ultrahigh vacuum/electrochemistry experiments. The LEED patterns showed either a Au(111)p(5 × 5)Ag or a Au (111)p(3 × 3)Ag structure, yielding open adlattices on Au(111) surfaces. The AES measurements, which provided insight into the identity of the species at the interface, indicated that there are significant contributions from sulfate in the upd Ag adlattice and that the presence of this anion affects the ability to measure the adlattice in the LEED experiment. The authors suggested that the sulfate adlattice is present on the surface prior to the onset of Ag upd, so that Ag species must in some way penetrate the sulfate adlattice to approach the Au(111) surface. A strong anion participation was also found for the system Au(111)/Cu/SO_4^{2-} employing in-situ STM, AFM and chronocoulometry together with the thermodynamics of the so-called perfectly polarized electrode [28, 30, 32]. However, this system differs from the previous one in that essentially all the sulfate becomes removed at the onset potential for Cu adlattice formation. In contrast, the sulfate adlattice was on the surface prior to the onset of Ag upd, and the metal adlattice grew in the presence of the anion.

The early LEED and RHEED (Reflection high-energy electron diffraction) studies for the determination of the structures of Cu adlayers deposited electrochemically up to one monolayer on Au(111) were performed by Kolb et al. [21, 38]. At very low coverages no superstructure patterns were observed, while at medium coverages, ordered layers of $(\sqrt{3} \times \sqrt{3})R30°$ and (2.2 × 2.2) type were found for Cu in sulfate and perchlorate solutions, respectively, due to the specific adsorption of the anions. In a previous work [22], the $(\sqrt{3} \times \sqrt{3})R30^o$ structure had also been observed by RHEED under normal vacuum for a submonolayer of Cu on Au(111).

AES measurements [21] also indicated that (bi)sulfate adsorption on Cu adlayers was stronger than that on the bare Au(111) substrate. A (1 × 1) structure was found for a Cu complete monolayer. However, in another work [133] employing the same techniques, it was shown that the first honeycomb structure evidenced a partial structural disorder after rinsing the electrode, leading to a loss of Cu adsorbate and to a partial rearrangement of the adlayer.

2.11 X–Ray Absorption Fine Structure

The use of synchrotron radiation and optical thin-layer cells allowed to perform in situ X-ray studies, so that another level of sophistication was achieved for in-situ determination of upd adsorbates structure on single crystal surfaces.

The use of X-rays is particularly suitable to study the electrode/electrolyte interphase because of their short wavelengths and significant penetration depth, properties that yield direct information of atomic distances and crystallographic structure [90]. Specifically, the X-ray absorption spectroscopy measures the absorption of X-rays as a function of the photon energy. The experimental data are presented as a plot of the absorption coefficient (κ) dependence on the incident photon energy, where this coefficient is determined from the decay in the X-ray beam intensity with distance ($\kappa = -\mathrm{d}\ln I/\mathrm{d}x$) [134]. The extended X-ray absorption fine structure (EXAFS) is related to the oscillatory variation of the X-ray absorption (expressed as absorption coefficient, κ) as a function of photon energy beyond an absorption edge. This absorption edge corresponds to a sharp increase in the absorption coefficient when the X-ray photon energy is tuned to the binding energy of some core level of an atom in the material. For atoms either forming part of a molecule or embedded in a condensed phase, the variation of the absorption coefficient at energies above the absorption edge (sufficiently high – 40–1000 eV), exhibit a complex fine structure (EXAFS) [135, 136]. Information on bond distances, coordination numbers, and atom identification can be determined. The use of synchrothon of X-ray sources provides high-intensity photon fluxes necessary to acquire sufficiently strong signals in a reasonable time, which was essential for the in situ structural analysis of the electrochemical interface. The electrochemical cell for X-ray absorption spectroscopy must be designed to minimize absorption losses at the window of the cell and the overlying electrolyte solution.

In relation with metal underpotential deposition processes, the EXAFS technique has been of great interest for studying these phenomena, since it has been able to elucidate definite structures involved in various potential regions as well as to show the occurrence of specific adsorption of ions.

An analysis of the underpotentially deposited Ag on Au(111) films on mica in 0.1 M $HClO_4$ containing 5×10^{-5} M Ag ions solution using EXAFS was reported by Gordon et al. [90], who pursued to investigate the local structure of the adsorbate. On the basis of the data analysis, they proposed a model, shown in Fig. 2.25, for the distribution of silver and oxygen (stemming from solution) on the

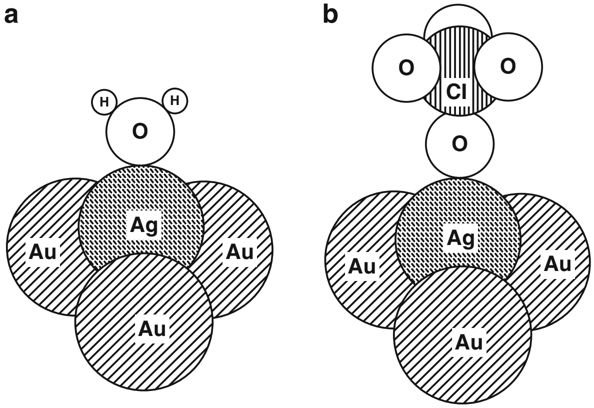

Fig. 2.25 Schematic illustration of the possible structure of an underpotentially deposited monolayer of Ag on a Au (111) substrate with either water (**a**) or perchlorate (**b**) bonded to the Ag adatoms through the oxygen, from EXAFS data analysis (Reprinted with permission from Ref. [90])

surface gold atoms, providing the data of bond lengths to gold and oxygen, suggesting that silver atoms sit at threefold sites on the gold surface with water (Fig. 2.25a) or perchlorate anion (Fig. 2.25b) bonded at a well defined distance.

Melroy et al. [137] also studied this system using sodium perchlorate as supporting electrolyte and showed that silver was on the surface on a fully reduced state. They concluded that the Ag monolayer is (1 × 1) commensurate with the Au (111) surface and that the Ag ad-atoms occupy threefold hollow sites, as proposed in the previous work [90]. They also observed backscattering from oxygen, presumably present in adsorbed water, which resides in either bridge or threefold hollow sites.

2.12 In-Situ Surface Differential X-Ray Diffraction

Rayment et al. [138, 139] studied the Ag upd on Au(111) in sulphuric acid media by in-situ surface differential X-Ray diffraction (SDD) in real time, using a conventional laboratory source of X-rays. Since this method has not been extensively used in the study of upd processes, only some features of SDD given by the authors will be indicated here. Basically, as X-Ray diffraction is an interference phenomenon, the adsorption of a plane of atoms on a set of diffracting planes will result in an interference, which will depend upon the spacing of the adsorbate plane with respect to the substrate planes and the atomic scattering factor of the adsorbate. The measurements consist in collecting the diffraction pattern of the bare substrate and that with the adsorbate layer on it, and then subtracting the former from the later. Thereby the change in the diffraction pattern due to the interference effect of the adsorbate on the diffraction from the substrate can be observed. Actually, a series of diffraction patterns are collected during the M upd as a function of potential, corresponding to different stages in the formation of the monolayer. Structural information such as adlayer spacing with respect to the spacings calculated for adsorption in different sites on the substrate surface, can be deduced from the characteristic interference profile.

The authors demonstrated that their SDD measurements together with cyclic voltammetry, revealed different phases of the Ag upd adlayer on Au(111) at different potentials, before the formation of the Ag(1 × 1) planar structure, since it was possible to monitor the adlayer spacing normal to the substrate as a function of potential. In a later work, Lee and Rayment [139] could monitor monolayer formation in situ and in real time by means of simultaneous electrochemical and structural measurements, and proved that the thin film electrode used for SDD analysis produced surface stress, which was responsible for some inconsistency in previous results. They found that Ag atoms were initially adsorbed in a mixture of bridge and atop positions, and after the completion of the upd monolayer a change in adlayer spacing was observed, which was consistent with a transition from initial adsorption in both bridge and atop sites to threefold hollow sites. They also showed that in the bulk region, there was a stepwise increase in differential intensity, with a constant adlayer spacing which is in agreement with a layer by layer growth of Ag on Au(111), as found by other authors [113].

2.13 Transmission X-Ray Surface Differential Diffraction

In order to use in-situ structural techniques under potentiodynamic conditions, Rayment and his group [140] developed the transmission X-ray surface differential diffraction technique and investigated the Ag adlayer structure on Au(111) in the underpotential region. From previous measurements using surface differential diffraction [138, 139], vertical positions of adsorbates from the substrate had been determined, but no information upon the lateral position of the adsorbate relative to the substrate was obtained. The authors demonstrated that this surface differential diffraction technique in the transmission mode allows to distinguish between different adsorption sites, resulting from the use of different anions in solution. By these experiments, it was possible to identify the adsorption site in three dimensions, confirming that Ag was adsorbed on multiple sites in a sulfate electrolyte whereas a single adsorption site (i.e. threefold hollow position) was found for acetate and fluoride solutions.

Results obtained with sulfate solutions allowed to explain the discrepancy between different Ag adlayer structures found in the literature. Summarizing, early AFM studies showed a (3 × 3) adlayer structure ($\theta = 1/3$) after the first deposition peak which was transformed to a (1 × 1) at lower underpotentials [14, 15]. The structures proposed from STM studies were a (√3 × √3)R30° one for the potential range 450–200 mV versus the Ag/Ag^+ couple, which transformed to a close packed (1 × 1) full monolayer at $E = 40$ mV [17]; a (4 × 4) open adlayer structure after the first deposition peak [13]; a (√3 × √3)R19.1° structure at potentials positive with respect to the first deposition potential and a (3 × 3) adlayer after the first deposition peak [109]. Despite the different adlayer structures found by AFM and STM in sulfate solutions, there was agreement that a stable adlayer was formed after the first adsorption peak, which contained Ag adatoms in a mixture of sites, threefold hollow ones and possibly both bridge and atop sites.

2.14 In-Situ Surface X-Ray Scattering

The in-situ surface X-ray scattering (SXS) technique was used to analyze also the Ag upd process on Au(111) in sulphuric acid solution [141]. This method, based on a synchrotron radiation source, is suitable to provide not only two-dimensional but also three-dimensional structural information about interphases with a very high resolution in situ. Due to the penetrating nature of X-rays, it can be used for in-situ structural studies of electrode surfaces. Basically, SXS involves measurements of the distribution of scanned X-rays in reciprocal space, and from this distribution of scattered X-rays an atomic model can be deduced and hence determination of surfaces structures may be possible [142].

In case of the system Au(111)/Ag^+, SO_4^{2-}, it was shown that initially a complete monolayer and then a “bilayer” of Ag, both with a (1 × 1) structure, were formed just before the bulk deposition started. The formation of a bilayer in the upd region was also proposed by Esplandiu et al. [109] from the charge obtained from cyclic voltammograms and STM studies, in contrast to previous works where the excess charge was attributed to the bulk deposition and the desorption of adsorbed sulfate and/or bisulfate anions during the upd process. The SXS measurements corroborated this assumption and indicated that electrochemically deposited Ag atoms both in the first and second layers were situated at the threefold hollow cubic closest packing (ccp) sites of the underlying Au and Ag layers, respectively.

2.15 Grazing Incidence X-Ray Diffraction

Grazing incidence X-ray diffraction or Grazing incidence X-ray scattering (GIXS) is another attractive tool to analyze surface structure and determine lattice spacings and atomic positions. In this case, a low angle of incidence of the X-rays upon the surface small angle (a grazing angle) enhances the electric field at the surface, thus increasing the ratio of scattering between the surface and the bulk [143]. In other words, since the refractive index of all materials at X-ray wavelengths is slightly less than unity, X-Ray beams are totally reflected for small glancing angles. Under the glancing angle condition, the electric field amplitude is doubled, resulting in an increase in scattered X-ray intensity. In addition, the background scatter originated from the bulk is reduced, since under grazing incidence conditions the penetration depth of X-rays is less than 10 nm. Therefore, this surface-sensitive technique results in an important tool to obtain microestructural information in directions parallel to the interface even on ultrathin epitaxial films [144, 145]. The cell used in this case must satisfy the same requirements as for EXAFS. Some advantages of this technique compared to EXAFS is that diffraction gives information on long-range order (not on the local environment of an element), and it is less sensitive to atomic vibrations, something which is useful when working with soft elements such

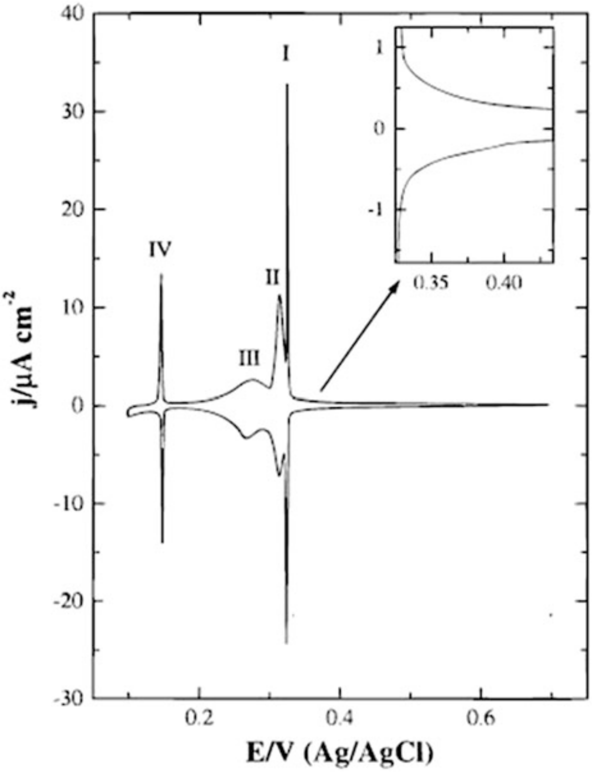

Fig. 2.26 Cyclic voltammogram of the system Au(111)/ 0.1 M $HClO_4 + 1.0$ mM NaBr + 1.0 mM CuO. $|dE/dt| = 1$ mV s^{-1} (Reprinted with permission from Ref. [147])

as lead [146]. Samant et al. demonstrated that GIXS can be used for in situ structural determination at the metal/solution interface, analyzing in situ the structure of electrochemically deposited monolayers of Pb on Ag(111) and Au(111) electrodes. They found that, when deposited on silver, Pb atoms become ordered in a hexagonal close-packed (hcp) geometry, with the lead lattice compressed 1.2 % relative to bulk lead. This layer was incommensurate with the silver substrate, with a 4.4° rotational epitaxy angle. On a Au(111) substrate, the underpotentially deposited lead monolayer was again found to order into a hcp geometry, incommensurate with the gold and compressed 0.7 % relative to bulk lead.

Later on, Herrero et al. [147] investigated the Cu upd in the presence of bromide anions employing cyclic voltammetry and GIXS together with other X-ray technique, CTR (Crystal Truncation Rod), which will not be addressed here, providing complementary information of the different interactions present. In order to understand the different structures found at different potential regions, a voltammetric profile for the system Au(111)/ 0.1 M $HClO_4 + 1.0$ mM NaBr + 1.0 mM CuO is shown in Fig. 2.26, which presents the four peaks characteristic of Cu upd on Au (111) electrodes in the presence of bromide.

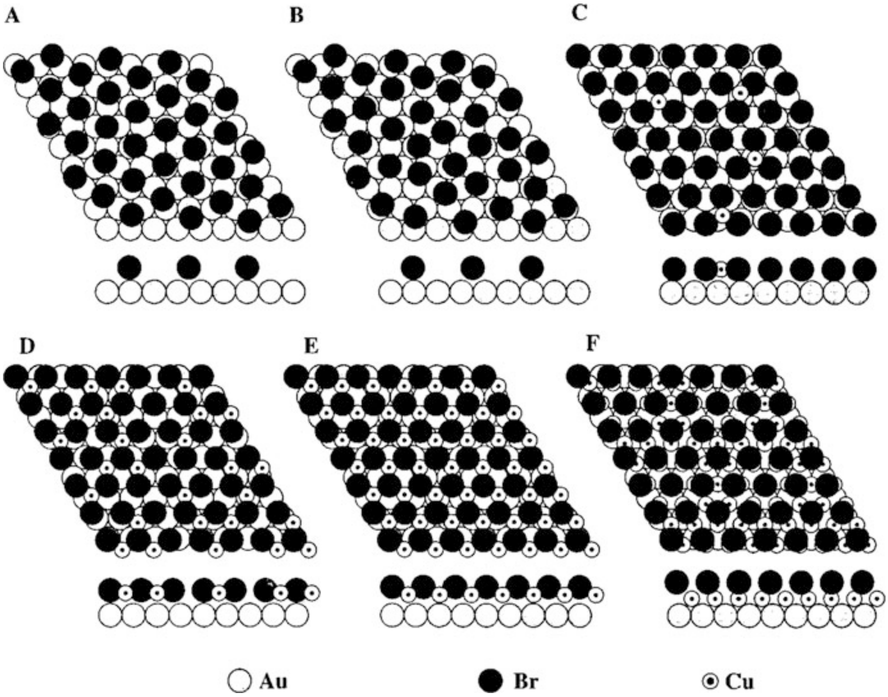

Fig. 2.27 Schematic representation of the overlayer structure of Cu deposited on Au(111) in the presence of Br^- anions at different potential values: (**a**) $E > +0.55$ V, (**b**) $+0.38 < E(\text{V}) < +0.55$, (**c**) $+0.32 < E(\text{V}) < +0.36$, (**d**) $+0.29 < E(\text{V}) < 0.32$, (**e**) $E = +0.29$ V, and (**f**) $E < +0.14$ V. For clarity, copper, gold, and bromide are not drawn to scale (Reprinted with permission from Ref. [147])

At potentials more positive than +0.55 V (vs Ag/AgCl), before Cu upd, bromide anions adsorb on the Au(111) surface forming an ordered and rotated hexagonal structure. The rotation angle of this structure with respect to the Au(001) direction and the Br – Br distance change with the applied potential. At potentials below 0.55 V, the bromide overlayer becomes disordered until an ordered one is formed at the beginning of Cu deposition (ca. 0.36 V) with an increase in bromide coverage. The X-ray measurements determined that Cu and bromide were mixed in the layer, with Cu atoms occupying some interstitial holes in the hexagonal bromide structure. As Cu deposition progressed (first adsorption sharp peak, I), a (4 × 4) bromide structure was found and then the Cu overlayer reached the Au(111) surface after lifting the anion layer. Between peaks II and III, the formation of a stoichiometric CuBr layer was observed and finally, after peak IV, there was a phase transition to give a (1 × 1) Cu layer with a bromide (4 × 4) structure adsorbed over the copper layer before bulk deposition. The schematic representation of such structures is shown in Fig. 2.27.

2.16 In Situ Infrared Spectroscopy

In situ Infrared Spectroscopy (IRS) at the electrochemical metal/electrolyte interface is a spectroscopic vibrational technique that provides information on molecular composition and symmetry, bond lengths and force constants, serving as complement of other surface-sensitive probes such as STM, EQCM, SEXAFS, etc. A better understanding of the physicochemical properties of the electrified interface can be achieved through this technique, because the obtained vibrational spectra of adsorbed species reflect the state of internal and external bonds, the lateral interactions within the adlayer, as well as the effect of the external electric field on the vibrational frequencies and intensities [148, 149]. When measuring IR reflectance spectra from a liquid/solid interface, two problems arise: one is that aqueous electrolytes are strong absorbers of IR radiation and hence the method is insensitive to changes occurring in the double layer; the other is that the sensitivity is relatively low to detect the small absorption due to a monolayer of adsorbed species. Such limitations may be overcome by using a very thin layer of solution, 10^{-4} to 10^{-3} cm, between the reflecting working electrode and the IR window, preventing the loss of IR energy by absorption in the solution. The sensitivity adequate for the detection of vibrational bands from submonolayer amounts of adsorbed species on electrodes, can be achieved by coupling of electrode potential modulation techniques to the optical signal [150].

2.17 Fourier Transform Infrared Spectroscopy

An important improvement of the IRS technique was achieved by the use of Fourier Transform instruments, because the high rate of collection of spectra in this case makes unnecessary the modulation of potential, thus giving the possibility of collecting spectra during the application of any desired potential program. This in situ – Fourier transform infrared spectroscopy (FTIRS) was used by Ashley et al. [33] to investigate the adsorption of sulfate (SO_4^{2-}) and bisulfate (HSO_4^{-}) ions on polycrystalline gold surfaces in sodium sulfate and also in sulfuric acid, with and without copper underpotential deposition. The authors related their findings with previous cyclic voltammetric studies obtained for a vapor-deposited polycrystalline gold substrate in a 0.5 mM $CuSO_4 + 0.5$ M H_2SO_4 solution. The cyclic voltammogram exhibited two adsorption/desorption peaks pairs at 0.20/0.22 V and 0.05/0.10 V, respectively, which up to that moment, were ascribed to $Cu^{2+} \rightarrow Cu^{+}$ for the first peak and to $Cu^{2+} \rightarrow Cu^{0}$ for the second peak. The PDIR (Potential-Dependent Infrared) spectra shown in Fig. 2.28, illustrated that the Cu upd exerts a strong influence on the behavior of sulfate, bisulfate and water on the interface, where the observed peaks were assigned to vibrations of surface anions.

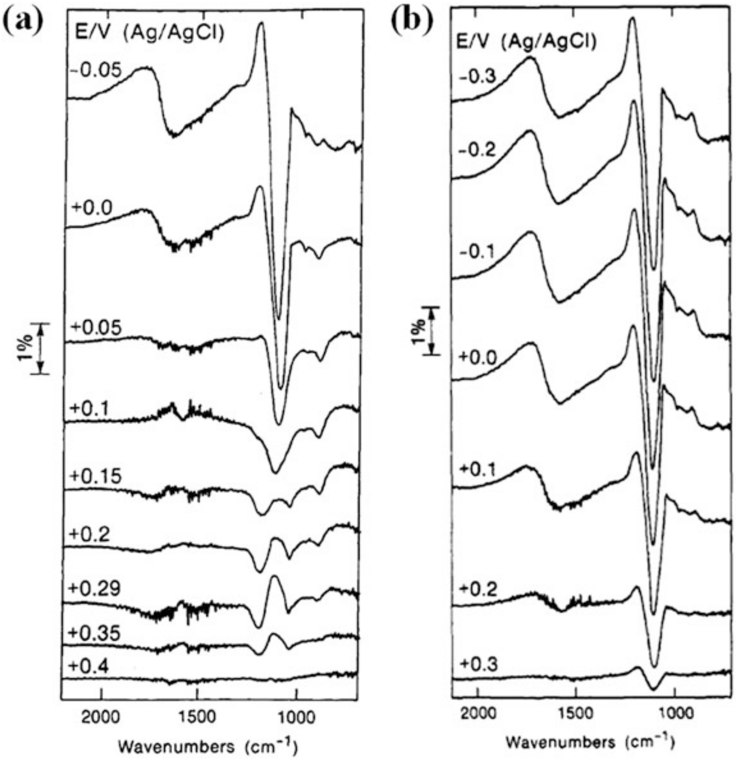

Fig. 2.28 PDIR spectra obtained on polycrystalline Au from (**a**) 0.5 mM $CuSO_4 + 0.5$ M H_2S0_4 and (**b**) 0.5 M H_2SO_4 (Reprinted with permission from Ref. [33])

The PDIR spectra (Fig. 2.28a) obtained within the potential region where bulk Cu was deposited (e.g. 0.00 and −0.05 V vs Ag/AgCl) were similar to those collected from 0.5 M H_2SO_4 on Au with no Cu present (Fig. 2.28b), where bisulfate species predominate. The results related to the Cu upd process on Au, indicated that adsorbed sulfate anion (located at ~1100 cm^{-1}) was present on Au at more positive potentials, and its coverage increased when underpotentially deposited copper was present on the gold substrate surface (Cu^+ upd region). When the applied potential was sufficiently negative to cause full discharge of Cu upd (when deposited Cu^+ was converted to Cu^0), IR spectra showed a loss of adsorbed sulfate and an increase in surface bisulfate species (bisulfate peaks located at – 1200, 1050, and 900 cm^{-1}), together with a reorientation of adsorbed water molecules. The bipolar water band near 1600 cm^{-1} also appeared when Cu^0 was formed. The results were explained in terms of surface electrostatic interactions during Cu upd, and also in terms of potential-dependent pH changes at the interface. These authors demonstrated the utility of IR spectroscopy technique regarding the possibility to analyze the interfacial behavior of electrolyte and solvent during upd processes.

2.18 Differential Reflectance Spectroscopy

The properties of adsorbed metal adatoms on metal substrates can be investigated also by differential reflectance spectroscopy (DRS). This optical method is employed to elucidate the optical and hence the electronic properties of metal adsorbates. It uses photons as a probing medium (i.e. ultraviolet, visible or infrared light), and is based on the interaction of these photons with strongly absorbing materials such as metals, alloys, and semiconductors, taking place in the first 10–20 nm of the surface[151]. This important feature allows DRS to probe 50–100 atomic layers into nontransparent solid surfaces having a characteristic probing depth different from other techniques such as XPS or XRD.

In the DRS technique, the normalized reflectance change $\Delta R/R$ due to the adsorption process is measured [3, 152, 153], and is defined in a general form according to:

$$\frac{\Delta R}{R} = \frac{[R(\theta) - R(0)]}{R(0)} \tag{2.3}$$

where $R(\theta)$ and $R(0)$ are the reflectances of the adsorbate-covered and bare surface, respectively. $\Delta R/R$ can be correlated with the optical properties of the adsorbate layer and those of the substrate and the solution, using a simple three-phase model with sharp boundaries. In general, the measurements are carried out at different wavelengths with fixed angles of incidence. In all cases, the measured changes are so large that optical effects from the solution side of the double layer can be neglected. For the system Au/Cu^{2+}, the reflectance change during metal deposition is mainly caused by an adsorbate induced change in the gold surface optical properties and not to absorption processes in the monolayer itself [154]. On the other hand, results from optical measurements of Cu atoms electrodeposited on Pt were presented as an example where the electroreflectance effect of Pt was negligibly small compared with the reflectance change caused by the adsorbate itself, while the influence of oxide formation or hydrogen evolution was excluded in this potential upd region. Kolb et al. [155] determined the optical constants for Cu underpotentially deposited on Pt, as a function of photon energy, angle of incidence, and adsorbate coverage, and found that the changes in the optical properties were ascribed to the Cu upd layer because the electroreflectance effect of Pt was negligibly small compared to the reflectance change caused by the adsorbate itself. It was also observed that these optical constants were quite different from those of bulk Cu, similarly to the case of Ag upd on Pt, where the deposition of 4–5 monolayers was required to obtain bulk metal properties [156]. The $\Delta R/R$ spectra (i.e. the reflectance change due to metal deposition) for a Cu monolayer on Pt single crystal electrodes revealed that the optical properties of the Cu monolayer also showed a pronounced dependence on the crystallographic orientation of the substrate. Discontinuities seen in the curve of reflectance change against coverage indicated a structural transition at such coverage.

In order to get further insight about the capabilities of this technique, Borensztein and Abelès [157] analyzed the surface reflectance spectroscopy technique and presented several application examples such as gas atoms or molecules adsorbed on metal surfaces in vacuum systems and very thin metal films deposited onto metallic surfaces, either in electrolytes or in ultrahigh vacuum. More information is available in the literature [158].

2.19 Optical Second Harmonic Generation

Optical second harmonic generation (SHG) is a non linear optical technique used to monitor surface structure in situ. In the optical methods defined above, the electrode is irradiated with light of a determinated frequency and the radiation is also detected at this frequency. However, non linear optical effects can result in the appearance of radiation at twice the fundamental frequency and this phenomenon requires a non centro-symmetric medium. Therefore, SHG can be observed in a localized region (a few atomic layers) at the interface between two adjacent centro-symmetric media (such as bulk metals and solutions), where a breakdown in symmetry occurs [159–161]. The SHG signal is sensitive to species at the interface but not very effective for their identification, but together with the electrochemical analysis of the system, can be used to detect adsorbed species, reaction intermediates, and changes in the nature of the electrode surface. For a further and a more comprehensive reading, several reviews about SHG are available including principles, theory, and applications [162–166]. Typical examples for the Au/Cu^{2+} and Au/Ag^{+} systems are mentioned below in order to provide the information that is obtainable from this technique.

Ashley and coworkers [167] used SHG together with the EQCM to study copper upd on polycrystalline gold in sulfuric acid electrolyte. The second harmonic signal from a polished bulk gold substrate was observed to decrease by $>60\ \%$ as a result of copper underpotential deposition on gold. The SH signals observed during copper upd, and subsequent removal of copper adlayers in a 1 mM $CuSO_4 + 0.5$ M H_2SO_4, are shown in Fig. 2.29. The substantial SH signal decrease during the negative potential scan was attributed to Cu upd on Au, before reaching a constant value at potentials more negative than 0.05 V vs Ag/AgCl. The authors pointed out that this decrease in SH intensity could result from an overall decrease in localized electron density at the interface when Cu became electrodeposited, until a full Cu monolayer was generated on the Au substrate, leading to a (1×1) commensurate structure. The SH signal remained constant on the positive scan, up to a potential of 0.3 V and then increased returning to the initial value. This observed hysteresis suggested that significant interfacial changes occurred due to the formation and dissolution of Cu adlayers, leading to different potential-dependent SHG magnitudes.

Koos and Richmond [168] have studied the structure and stability of underpotentially deposited Cu, Ag, Pb and Tl layers on Au(111) by SHG. They

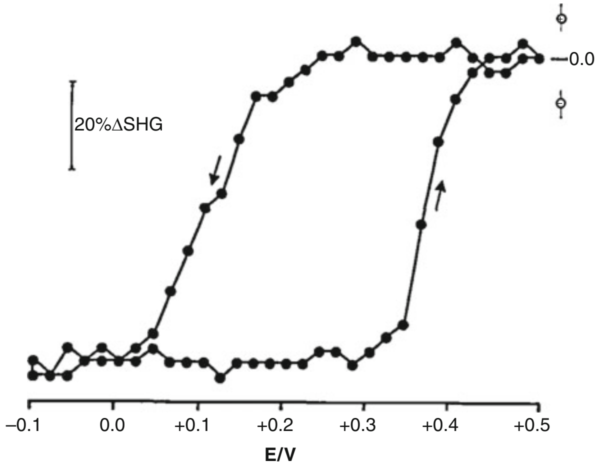

Fig. 2.29 Measured SHG intensity vs potential applied to the electrode surface. Electrolyte: 1 mM $CuSO_4 + 0.5$ M H_2SO_4. *E* is expressed vs Ag/AgCl reference electrode (Reprinted with permission from Ref. [167])

found similar patterns for the Au(111)/Ag surface and for Au(111) surface in the absence of Ag, originated by the ability of Ag adatoms to lattice match with the Au (111) surface, so that the surface electronic structure was not modified. Likewise, the optical responses from the Au(111)/Cu interface and the Au(111) surface were consistent with the known electronic structure of the metal and the geometric structure of the overlayers. In the case of Pb and Tl electrodeposition, a strong perturbation of the anisotropic second harmonic signal was observed and the authors attributed these changes to the inability of the large adatoms to lattice match with the substrate ($r_{Pb}/r_{Au} = 1.21$ and $r_{Tl}/r_{Au} = 1.18$), causing a substantial modification of the surface electronic structure.

Later, Walters et al. [169] reported surface kinetics results of electrodeposited Ag on Au electrodes for the cases of underpotential and bulk deposition, combining potential step and optical second harmonic generation techniques. They suggested that electrodeposited silver on polycrystalline gold followed a mixed 2D-3D growth mode and found evidence that the surface structures were predominantly flat and grew at a considerable slow rate. The SHG experiments showed also the difference between the bulk Ag structures deposited on Au from those supported by a submonolayer film of Ag on Au.

2.20 Surface-Enhanced Raman Spectroscopy

With the aim of getting more information about the properties of M upd layers, Surface-enhanced Raman Spectroscopy (SERS) has also been used to this purpose. SERS is a surface spectroscopic technique that, like Fourier transform infrared spectroscopy, is based on probing molecular vibrations of the molecules adsorbed on a substrate surface. Actually, the final letter S can also stand for Scattering, emphasizing the optical effect rather than the technique. It is applicable most usefully to adsorption on the coinage metals, copper, silver and gold, which are highly reflective in the visible, and provides in situ information about the chemical identity of the adsorbed species, protonation/deprotonation state, molecular structure, and orientation of adsorbates at surfaces [170, 171]. The enhancement is provided by plasmon resonances (family of effects associated with the interaction of electromagnetic radiation with metals) in the metal substrate. However, a chemical enhancement involving a resonance Raman-like process associated with chemical interactions between the molecule and the metal surface can also contribute to the major SERS effect [172]. SERS mainly comes about as a combination of the two effects. Therefore, a remarkable enhancement of the scattering intensity can be observed for species that are adsorbed on, or are microscopically close to, appropriately roughened surfaces. In this case, the atomic flat surfaces commonly used in fundamental research in electrochemistry, are not suitable for SERS investigations. The roughening of the electrode surfaces usually involves the application of oxidation-reduction potential cycling in sulfate or chloride media, chemical etching in acids, electrochemical deposition of films on the substrate, etc. [173]. The inherent constraints of the technique are the limited substrate choices that exhibit localized surface plasmon resonance behaviour (Cu, Ag and Au) and the need for a roughened surface, which due to variation in the fabrication procedures can lead to inconsistent optical properties and hence, discrepant enhancement factors.

More literature about the SERS technique is available for further reading [174–176]. The use of SERS in upd systems are presented in the following examples.

Weaver et al. [177] reported surface enhanced Raman spectra for representative adsorbates, namely, halides, thiocyanate, benzonitrile, and pyridine adsorbed on upd monolayers of Ag and Cu on electrochemically roughened Au electrodes, as compared with corresponding spectra at unmodified Au and at Ag and Cu electrodes. The SER intensities on the upd surfaces were comparable to, or higher than, those observed for the bulk metal electrodes, exhibiting reversibility with respect to negative–positive potential excursions, as noted for Au substrates. Figure 2.30 shows sets of SER spectra at Ag upd on Au obtained as a function of potential for adsorbed chloride (A) and bromide (B) anions.

From the previous results, it was observed that the surface-bromide and the surface-chloride band at the most positive potentials were more intense than those typically obtained under similar conditions for conventional Ag and Au surfaces, leading to sharp decreases in the band intensities when the potential was changed to more negative values. Furthermore, these band intensities were largely recovered when the potential was reversed to the original value for anodic stripping of Ag monolayer. The same behaviour was observed for Au but not for Ag where a complete irreversible loss of SERS occurred upon such negative potential excursions. Therefore, the authors were able to infer that the stability of the SERS signals characteristic for Au substrates, was retained after the deposition of Ag upd monolayer. In this work it was also demonstrated that the surface-halide stretching frequencies and the C-N and surface-sulfur frequencies for thiocyanate on Ag upd were significantly higher than those on bulk silver electrodes at a given potential.

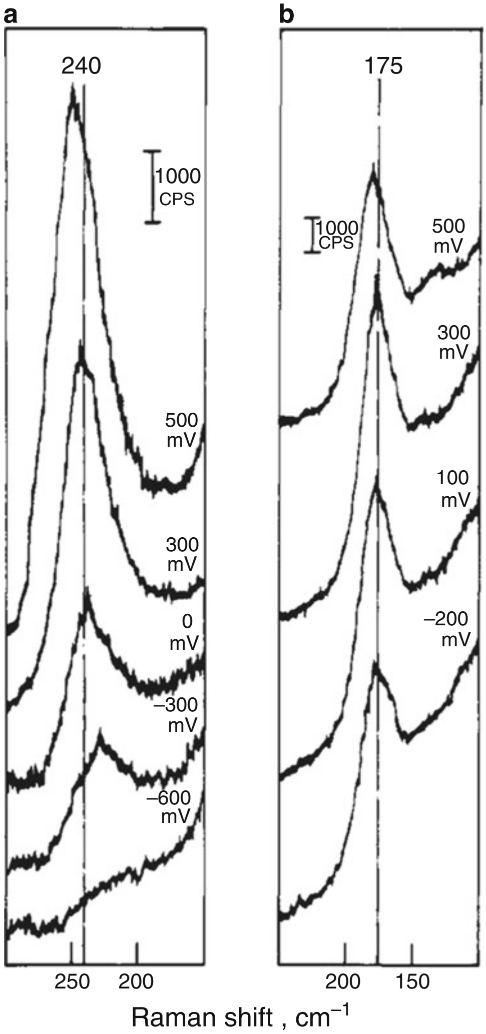

Fig. 2.30 SER spectra dependence on potential for: (**a**) chloride and (**b**) bromide adsorbed on an upd Ag monolayer on Au. Electrolytes: 10 mM NaCl + 0.1 M $NaClO_4$, and 10 mM NaBr + 0.1 M $NaClO_4$, respectively (Reprinted with permission from Ref. [177])

This behaviour was attributed to the greater electronic polarization of the adsorbate on the upd silver surface caused by the underlying gold substrate. Qualitatively similar, although smaller, frequency differences were seen for thiocyanate adsorbed on upd copper and bulk copper electrodes. Similar SER spectra were also seen as a function of electrode potential for benzonitrile and pyridine adsorbed on the corresponding upd and bulk metal electrodes.

Another work performed by two of the previous authors also showed the influence of modifying Au electrodes by upd layers on adsorbate-surface interactions by SERS [178]. Surface Enhanced Raman (SER) spectra were analysed for several adsorbates on underpotential deposited layers of mercury, thallium, and lead on an electrochemically roughened gold electrodes, concluding that metal overlayers on gold provide a mean to examine adsorbate-metal bonding at surfaces which do not exhibit suitable Raman scattering enhancements.

At the same time, Fleischmann and Tian [179] found that the underpotential deposition and dissolution of monolayers of Pb and Tl on Ag roughened surfaces produced diminished surface enhanced Raman scattering, while electrodes covered by complete upd and overpotential deposited layers allowed significant SER spectra. They also probed that chloride ions were especially active in causing the loss of SERS.

2.21 Techniques Suited to Study Alloy Formation During the upd Process

In many upd systems the strong metal-substrate interaction induces place exchange processes, which lead to the formation of M-S surface alloys. This phenomenon is usually observed in systems exhibiting sufficient miscibility between the substrate and the upd metal and is usually kinetically hindered at room temperature [1]. For this reason, experiments at elevated temperature or with long-time polarization at room temperature should be carried out in order to study the formation of alloy phases. The phenomenon can be recognized by the appearance of a new desorption peak at relatively high underpotentials in an anodic linear sweep measurement and changes in the normal desorption peaks corresponding to the M upd adsorption process. STM and AFM measurements also provide detailed structural information and show clearly the drastic changes in surface morphology due 2D M-S surface alloy formation.

Interdiffusion has been observed in the following systems: Ag/Tl^{+} [180–183], Ag/Pb^{2+} [182–193], Au/Pb^{2+} [194–197], Ag/Cd^{2+} [198–203], and Au/Cd^{2+} [91, 204–211]. Typical examples are represented by the systems Au/Cd^{2+} and Ag/Cd^{2+}, which were considered as model systems for the study of surface alloy formation processes.

García et al. [201, 202] analyzed the kinetics and mechanism of Cd upd on Ag (111) and the surface alloy processes involved in sulfate solutions by means of combined electrochemical measurements and in-situ STM. In relation with the surface alloy phenomenon, they showed that, at long polarization times, the condensed Cd monolayer formed via a first order phase transition undergoes structural changes involving place exchange processes between Cd atoms and surface Ag atoms. The formation of a second Cd monolayer and a significant Ag-Cd surface alloying takes place at lower underpotentials ($\Delta E < 50$ mV). The kinetics of surface alloying was studied on the basis of a diffusion model proposed by Vidu and Hara [208] for the system Ag(100)/Cd, including the relatively fast initial formation of a very thin surface alloy film and the subsequent slow alloy growth controlled by solid state diffusion. The results were in good agreement with previous measurements in the system studied [199] and suggested that at long polarization times, alloy formation occurs preferentially by the motion of Ag atoms through a vacancy–rich surface alloy layer and the simultaneous Cd deposition at the Ag-Cd interphase. Anodic dealloying led to the appearance of a large number of 2D islands and monatomically deep pits as was observed by in-situ STM after anodic stripping. The clustering of vacancies created during removal of Cd from the surface alloy led to formation of larger pits, which disappeared by changing the underpotential to sufficiently positive values. This behaviour suggested a high mobility of Ag surface atoms at these potentials in good agreement with observations reported previously in studies with Ag(100) substrates [212].

The surface alloy process has also been observed in systems consisting in an ultra-thin Ag-Cd bimetallic layer with epitaxial arrangement on Au(111) electrodes, electrochemically deposited from separate electrolytes containing Ag^+ and Cd^{2+} ions, as well as from a multicomponent solution containing both ions [213, 214]. Anodic stripping curves obtained after long time polarization experiments demonstrated that a significant Ag–Cd surface alloying accompanied the formation of the Cd monolayer on the Au(111)/Ag modified surface, irrespective of the Ag film thickness. In the case of an extremely thin Ag layer (1 Ag ML) and taking into account the results obtained by the same authors for the Au(111)/Cd system [209], the STM images and long time polarization experiments revealed a solid state diffusion process of Cd, Ag, and Au atoms, which can be responsible for the formation of different Ag–Cd or Au–Ag–Cd alloy phases. Figure 2.31 shows a sequence of in-situ STM images corresponding to the formation of the Ag-Cd bimetallic layer onto the Au(111) substrate from a solution containing both metallic cations and its dissolution. Figure 2.31a shows the surface morphology of the bare Au(111) substrate at $E = 650$ mV vs SSE, composed of flat terraces. Figure 2.31b exhibits a Ag ML electrodeposited onto the Au(111) surface after a polarization time, $t_p = 15$ min at $E = -200$ mV (Ag overpotential deposition region). This Au (111)/Ag modified substrate was then polarized at $E = -1170$ mV producing a Cd ML (Fig. 2.31c), and also, the formation of a second Cd ML, as recognized by the presence of 2D Cd islands. Figure 2.31d displays the Au(111) surface morphology after the anodic dissolution of both Cd and Ag monolayers by polarization at $E = 650$ mV. As seen, the removal of both layers leads to the appearance of a large number of 2D islands and monatomically deep pits on the original gold terraces, indicating an alloy dissolution process. In particular, this type of behaviour was observed in the systems Au(111)/Cd^{2+} [209, 215, 216] and Ag(111)/Cd^{2+} [201], but was practically not observed during Ag upd on Au(hkl) [13, 113]. Therefore, it was possible to infer that in the present case, the Cd atoms reached the underlying Au surface by diffusion and/or by a place exchange mechanism with the Ag and Au atoms.

Recently, the Cd upd process in the system Au(100)/Cd^{2+}, $SO_4{}^{2-}$ and the Au-Cd surface alloy involved were investigated by the same group, by conventional electrochemical techniques and in-situ STM analysis arriving to similar conclusions [211].

García et al. [203] studied the formation of bimetallic Cd–Ag nanoparticles on vitreous carbon (VC) by conventional electrochemical techniques and ex-situ AFM. The solutions used for metal deposition were: 1 mM $Ag_2SO_4 + 0.02$ M

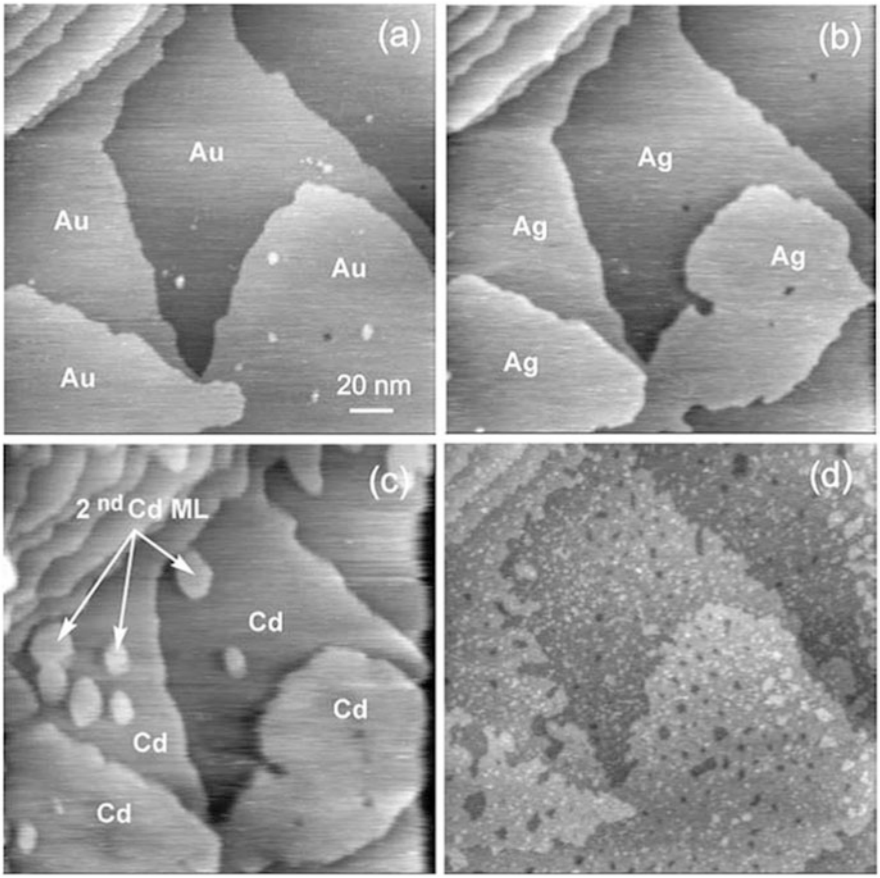

Fig. 2.31 Sequence of in-situ STM images obtained during the formation of a Ag/Cd bimetallic layer onto a Au(111) substrate under different conditions. (**a**) Bare Au(111) surface at $E = 650$ mV; (**b**) formation of a Ag ML at $E = 200$ mV; (**c**) formation of a Cd ML at $E = -1170$ mV; (**d**) surface morphology after anodic stripping at $E = 650$ mV (Reprinted with permission from Ref. [214])

$H_2SO_4 + 0.1$ M Na_2SO_4 and 2 mM $CdSO_4 + 0.1$ M Na_2SO_4 (pH = 2.28), whereas a 0.1 M Na_2SO_4 (pH = 2.28) solution was employed as blank electrolyte. The authors demonstrated that alloy formation between both metals could be inferred, which had not been previously reported using nanoparticles. They found that the alloy formation phenomena observed previously during Cd upd on bulk Ag electrodes [199, 201, 213] was also found in the case of Cd upd on Ag nanoparticles. The desorption spectra in the system Cd/Ag (nanoparticles)/VC employing different polarization times, showed three desorption peaks associated with the dissolution of the Cd overpotential deposits (opd) and upd deposits and a Ag–Cd alloy formed at low underpotentials, respectively. This phenomenon was also confirmed by performing an anodic stripping of Ag/Cd deposits to more positive electrode potentials in a blank electrolyte solution.

2.22 In-Situ Measurement of Surface and Growth Stress

Less frequently employed for studying the alloy formation process in the upd region, is the in-situ measurement of surface and growth stress, which is originated by the difference of the atomic configuration of surface atoms with regards to that in the bulk. Experimental procedures and equipment for this technique are detailed elsewhere [217]. The simplest and most widely used method involves the measurement of the deflection of a flexible cathode, typically in a direction that is perpendicular to the in-plane stress generated in the film. Interferometry, capacitance measurements, laser beam deflection and STM/AFM can be employed for monitoring the deflection. Stafford and Bertocci [217] indicated that the adsorption of species on the surface can be expected to alter the surface stress, since the local interaction of each adsorbate will modify the bond strength between neighboring atoms on the surface. Also the lattice misfit between a metal adlayer and the substrate generates surface stress, where the sensitivity of the later to both ionic and fully discharged adsorbates makes this measurement attractive for upd studies. Stafford et al. [218] investigated the voltammetric and stress response during Pb upd on textured Au(111) evaporated films in 0.1 M $HClO_4$ containing 10 mM Pb $(ClO_4)_2$ solution. Particularly, the authors analyzed the stress behaviour of the system at different sweep rates and observed initially, as shown in Fig. 2.32a, an increase in the surface stress, similar to that observed in Pb^{2+}-free solution, associated with a combination of electrocapillarity and surface charge redistribution induced by anion desorption. At a potential of about −0.43 V vs SSE, a change of stress in the compressive direction was detected, under conditions where nucleation and growth of Pb islands took place [196]. Then, stress relaxation in the tensile direction occurred in a very narrow potential range after which the Pb monolayer was completed. From results reported previously [219], the surface stress was correlated to Pb coverage, obtaining an overall compressive surface stress change

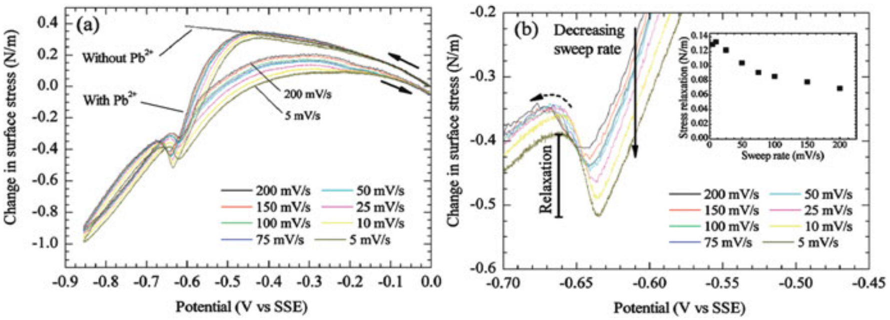

Fig. 2.32 (**a**) Dependence of surface stress on potential during Pb upd on a (111)-textured Au film at different sweep rates (5–200 mV s^{-1}). Solutions: 0.1 M $HClO_4$ with and without 10 mM Pb $(ClO_4)_2$. (**b**) Magnification of the zone where stress relaxation takes place. Only cathodic scans are shown. Inset: magnitude of stress relaxation as a function of sweep rate (Reprinted with permission from Ref. [218])

of about -1.2 N m^{-1} for the complete Pb monolayer. With further deposition, the stress moved once again in the compressive direction, as more Pb atoms were incorporated into the adlayer, causing contraction of the interatomic spacing and eventually rotation of the monolayer. Previous results obtained by Welland et al. [220] led to similar conclusions. In this case, an AFM Au-coated cantilever was used as a bending-beam sensor to measure surface stress changes, which occurred during the electrodeposition of Pb monolayer on Au(111), without considering alloy formation. This phenomenon could not be studied due to experimental conditions where fast scan rates were needed to avoid thermal drift.

The sweep rate dependence of surface stress is shown in the inset of Fig. 2.32b, indicating that at slower sweep rates, larger compressive stress was developed, something that can be explained by the occurrence of Pb-Au surface alloying, because in this case the slow sweep rate allows more time for the hcp adlayer to transform to the alloy structure. The authors concluded that the stress behavior was due to kinetically controlled surface alloying occurring at low coverages, while at high coverages the surface alloy removal took place generating a hexagonal close-packed Pb monolayer with subsequent Pb deposition. This behaviour was quite different from other systems, such as Ag(111)/Cd, in which, as mentioned above, the alloying was produced into the solid state at complete coverage and the charge required to strip Cd adatoms exceeded that of a monolayer [201]. Stafford and Bertocci also suggested that the observed stress relaxation hump could be caused by an alloying/dealloying transition. Therefore, after many cycles of Pb deposition and dissolution, the (111)-textured Au surface was roughened, as a consequence of surface alloying and dealloying processes, in accordance with the STM results reported by Green and Hanson [197].

2.23 Applications of upd as a Tool

As the M upd phenomenon is the initial stage of metal phase formation, it has often been used to modify electrodeposition processes and has been regarded as a powerful tool to modify, in a controlled way, the catalytic properties of the substrate.[5]

On the other hand, M upd has been employed to prepare ultrathin metal films. For example, a method has been developed by Brankovic et al. [221] in which an ordered metal adlayer underpotentially deposited on a substrate is replaced by a more noble metal monolayer in an electroless deposition process, producing 2D deposits uniformly covering the substrate surface. The replacement of the M upd layer takes place via an irreversible and spontaneous redox process in which this adlayer is oxidatively dissolved by cations of more noble metals, which are simultaneously reduced and deposited. The authors applied this procedure using a

---

[5] This application of M upd will be discussed in detail in Chap. 4

Cu upd adlayer on Au(111) as "sacrificial layer", which was then replaced by a submonolayer of Pt, a monolayer of Pd and a bilayer of Ag in a spontaneous reversible redox process. The total amount of the deposited metal was determined by the stoichiometry of the redox reaction and the structure of the upd Cu adlayer. This method, known later as *Surface-limited redox replacement* (SLRR), refers then to a confined, in a monolayer or two, reaction where a predeposited metal layer is replaced by a more noble metal at open-circuit potential, and offers an interesting alternative approach to prepare bimetallic catalyst surfaces or uniform ultrathin 2D M films. The applicability of this procedure was also examined for the systems Au (111)/Cu and Ag(111)/Cu [222]. Two-dimensional growth of Cu up to 100 monolayers has been achieved by multiple redox replacement of monolayers of underpotentially deposited Pb used as a sacrificial metal. In this case, open-circuit potential monitoring during the replacement reaction was used to control the completion of each deposition event and the film thickness was determined by anodic film stripping. The excellent surface quality of the epitaxially grown Cu film was characterized by STM in situ and XPS analysis, which showed no traces of Pb into the Cu film.

In a recent work, Brankovic et al. [223] analyzed the stoichiometry of Pt deposition on a Au(111) substrate by SLRR employing Cu upd as intermediate, emphasizing that it was influenced by the specific experimental conditions and anions involved. The Au(111)/Cu upd was formed from a 10^{-3} M Cu^{2+} + 0.1 M $HClO_4$ solution, whereas the Pt deposition (redox reaction) was carried out from a 10^{-3} M $[PtCl_6]^{2-}$ + 0.1 M $HClO_4$ solution. The results indicated that, as the anion of the supporting electrolyte of both solutions was ClO_4^{-}, which does not have the tendency for complexing the Cu ions, the ligand in the depositing complex, $[PtCl_6]^{2-}$, was responsible for the final oxidation state of dissolved Cu ions as it stabilized the Cu^{+} ions forming the complex $[CuCl_2]^{-}$. Combining the statistical STM data analysis and conventional electrochemical techniques, the authors concluded that the Cu upd adatoms oxidation to Cu(I) was thermodynamically more favorable than their oxidation to Cu(II), during the redox replacement reaction, suggesting that four Cu upd adatoms were replaced by each deposited Pt adatom.

As the electrochemical deposition method based on SLRR of underpotentially deposited sacrificial metal monolayers has gained considerable interest due to its broad applications in the preparation of catalytic materials and growth of ultrathin epitaxial films, the kinetics of metal deposition via this technique was examined by the same authors [224]. The model system was Au(111)/Pt using Pb and Cu upd sacrificial monolayers deposited on Au(111), considering $HClO_4$ and H_2SO_4 supporting electrolytes. The parameters of the reaction kinetics, i.e. reaction half time, reaction order and reaction rate constant, were determined. The effects on the reaction kinetics of the nature of the M upd monolayer, the transport limitation and the present anions were also investigated.

In recent years, the synthesis of multimetallic nanoclusters has been extensively studied due to their widespread applications specifically in electrocatalysis. Electrodeposition of these nanostructures can be performed by codeposition of metals from a common electrolytic bath or by sequential deposition of the involved metals. The SLRR methodology is another option for the preparation of bimetallic nanoclusters.[6]

Several studies have been reported about thin composite films, using M upd layers. Particularly, the formation of nanostructures composed by compound semiconductors is of great interest because their application in optoelectronic devices. Epitaxial growth of compound semiconductors was achieved by Stickney and co-workers [225–228] using the so-called *Electrochemical Atomic Layer Epitaxy* (ECALE) method, which is based on successive upd atomic layers of different elements to form a compound. The principle is similar to that of the SLRR in the sense that both use surface limited reactions to form each atomic layer of a deposit. They developed this method for the production of II-VI compound semiconductors which are deposited epitaxially. The upd is used in order to limit deposition to a monolayer and because of the enhanced stability provided by bond formation between the II and VI elements, relative to formation of bulk elemental deposits [229]. The thin-layer electrodeposition of CdTe on a Au polycrystalline electrode was the first system studied employing the ECALE method. This deposition technique has several advantages such as the prevention of generating three-dimensional nuclei by never exceeding the monolayer regime. The control of deposition potentials is such that only deposition enough to cover the deposit occurs and the combination of each successive element with only the element previously deposited, prevents the mixing between the metals being deposited. Adequate deposition potentials and solution composition are necessary for each element being deposited. Each deposition cycle forms a monolayer of the compound, and the number of cycles determines the thickness of the deposit.

Most semiconductors compounds consist of both a metal and a main group element such as Te, Se, S, As, Sb, or Bi. At present, several compounds have been prepared by ECALE. Among them are CdTe, CdSe on polycrystalline and single crystal Au electrodes [226, 230–233]. Another groups adopted Ag(111) as substrate to prepare semiconductor compounds. For example CdTe and ZnSe deposition on Ag(111) was obtained by ECALE, alternating underpotential deposition of atomic layers of the elements making up the compound [234, 235].

Upd-based systems have been analysed in recent years for the development of electrochemical supercapacitors, which attract growing attention as electrical energy storage systems because of the high capacitance of the electrode materials resulting in higher specific power than batteries and higher specific energy than conventional capacitors. The supercapacitor processes are, ideally, 2-D and rely on faradaic processes in which a monolayer or quasi-monolayer of electrochemically

---

[6] It will be discussed in detail in Chap. 6

Fig. 2.33 Chronopotentiogram of Tl upd on Ag in the presence of Br^- ions at $I = 10\ \mu A\ cm^{-2}$. Electrolyte: 2 mM $TlNO_3$ + 20 mM KBr + 1 mM KNO_3 (Reprinted with permission from Ref. [237])

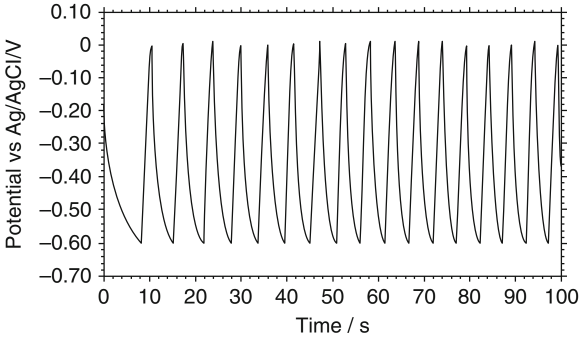

reactive species can be electrosorbed or electrodesorbed with charge transfer via upd processes, e.g. Cu on Pt, Pb on Au, Bi on Au, Bi on Ag [236].

Girija and Sangaranarayanan [237] have studied Tl upd on Ag in the presence of bromide ions. They demonstrated the feasibility of upd-based systems as supercapacitors using this system as an illustrative example and estimated the specific capacitance employing voltammetric and galvanostatic charge/discharge studies. Upd-based supercapacitor systems are favorable due to the following considerations: high reversibility, large pseudocapacitance values, wide choice of the substrate and depositing species, feasibility of employing aqueous and non-aqueous solvents, specific choice of electrolytes in order to increase adsorption via pseudocapacitance. Figure 2.33 shows a typical chronopotentiogram obtained at a constant current density of 10 μA cm^{-2} over the Tl upd range, exhibiting the usually charge/discharge behaviour of supercapacitors. Furthermore, the charge curves are symmetrical to their corresponding discharge counterparts in the potential region considered, an essential criterion for the feasibility of supercapacitors, and the reversibility is maintained for ~10^2 cycles.

2.24 Photoacoustic Technique

The Photoacoustic (PA) technique has not been widely applied for upd systems but some works are found in the literature. Fujishima et al. [238, 239] reported results on the Au oxide layer and the plating of Cu on Au, demonstrating the capability of the Photoacoustic spectroscopy (PAS) to study the surface behaviour of metal electrodes in-situ. They also described the cell and the experimental procedure used for this purpose, where the current-potential and photoacoustic signal-potential curves are recorded simultaneously. Basically, PA refers to the generation of acoustic waves by modulated optical radiation. The process involves absorption of light (e.g. laser beams) in the working electrode and production of heat followed by propagation of heat-generated thermal waves to the electrode surface. Heat is then transferred into the adjacent gas, varying its pressure, which is then measured by a microphone as the photoacoustic signal. This technique differs from the conventional ones mainly by the fact that even though the incident energy is in the form of optical photons, the interaction of these photons with the sample is studied not through subsequent detection and analysis of some of them but rather through a direct measure of the energy absorbed by the material because of its interaction with the photon beam [240, 241].

Later, Fujishimaet al. [242] demonstrated that PAS is a sensitive optical method that has both sensitivity and ability to provide in-situ information about the interface electrode-electrolyte modified by upd. They were able to detect Pb upd from 0.1 M $NaClO_4$, +0.01 M $Pb(ClO_4)_2$ + 0.005 M $HC10_4$ solution onto Ag substrate employing PA. The clear peaks pair (deposition and dissolution) related to the Pb upd were detected in the PA signal-potential curve showing a slight increase or decrease at the potential where the peaks in the current-potential curve were evidenced. The slow transformation phenomena of Pb adsorbates on Ag(111) electrode surfaces [183–192] reported previously, was also detected as a slight fluctuation of the PA signal.

2.25 Electrochemical Impedance Spectroscopy

The potentiodynamic electrochemical impedance spectroscopy (PDEIS) is a relatively new and promising technique to study in real time the electrochemical response of metal monolayers and nanostructures on various substrates providing fast acquisition and visualisation of the interface response to ac and dc current in a single potential scan [243, 244]. In a simple experiment, the cyclic voltammogram of the system and the Nyquist and Bode plots extended to 3D as a function of potential are obtained. These later are then individually extracted from the 3D plots as orthogonal sections and decomposed by a built-in equivalent circuit analyser into the constituent responses of the circuit elements, analogous to conventional ac impedance measurements. Unlike conventional electrochemical impedance spectroscopy (EIS), which analyses frequency response in stationary states to obtain the whole equivalent circuit, PDEIS analyses the ac response in terms of equivalent electric circuit parameters dependences on the potential, allowing dynamic surface control. PDEIS appeared to be useful for nonstationary effects monitoring in upd. Different equivalent circuits were found for reversible and irreversible upd processes. For the first ones, low-amplitude ac probing generates oscillation of adatom coverage, which produces the capacitance of adsorption in the equivalent circuit, but no adsorption capacitance was found in irreversible upd systems. Moreover, PDEIS enables separate monitoring of anions coadsorption in upd processes.

Ragoisha and Bondarenko [245] demonstrated the application of PDEIS to copper underpotential deposition on polycrystalline gold in 10 mM $CuSO_4$ + 0.1 M H_2SO_4 and 10 mM $Cu(NO_3)_2$ + 0.1 M HNO_3 providing in situ investigation of anion adsorption during copper monolayer formation on gold. The dependences of the equivalent circuit parameters on potential showed different behaviours of nitrate

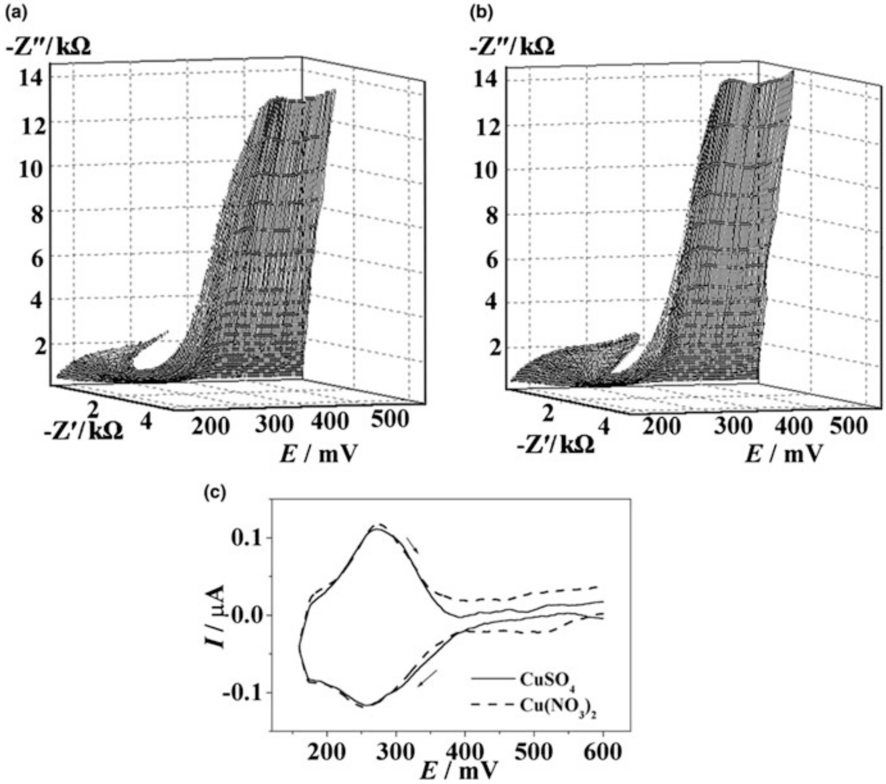

Fig. 2.34 Cathodic (**a**) and anodic (**b**) branches of the PDEIS spectrum for Cu upd on Au in 10 mM $CuSO_4$ + 0.1 M H_2SO_4. (**c**) Cyclic voltammograms of Au in 10 mM $CuSO_4$ + 0.1 M H_2SO_4 and 10 mM $Cu(NO_3)_2$ + 0.1 M HNO_3 solutions. $|dE/dt| = 2$ mV s^{-1} (Reprinted with permission from Ref. [245])

and sulfate ions. The authors also indicated that the results revealed some irreversibility of the constituent processes that appeared to be reversible from cyclic voltammograms.

Figure 2.34 shows the PDEIS spectra, cathodic (Fig. 2.34a) and anodic (Fig. 2.34b) branches, for the system Au/10 mM $CuSO_4$ + 0.1 M H_2SO_4 and the corresponding cyclic voltammogram together with the voltammetric results in the system Au/10 mM $Cu(NO_3)_2$ + 0.1 M HNO_3 (Fig. 2.34c). Differences between the ac responses of the cathodic and anodic scans evidenced intrinsic irreversibility and non-stationary of the underlying processes. The presence of sulfate and nitrate anions for Cu upd on Au shows no pronounced changes in voltammetric results which is not the case as it is shown below. In Fig. 2.35 the best-fit equivalent circuit in each case, and the dependences of the equivalent circuit parameters on the potential are presented, such as the double layer capacitance (C_{dl}), the pseudocapacitance and pseudoresistance of Cu upd (C_c, R_c) and anion adsorption (C_a, R_a).

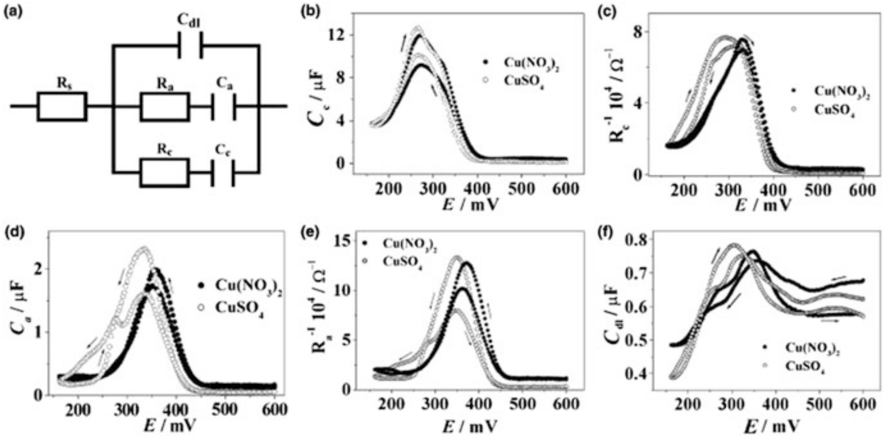

Fig. 2.35 (**a**) Equivalent electric circuit obtained from the PDEIS spectra for Cu upd on Au, (**b**)–(**f**) dependencies of the equivalent circuit parameters on potential (Reprinted with permission from Ref. [245])

Nitrate adsorption pseudocapacitance, and the inverse of the adsorption pseudoresistance, both exhibited peaks in a narrow range of Cu monolayer growth, while sulfate affected a wider potential range and gave two desorption peaks in the anodic scan. The complex and different potential dependences of the double layer capacitances in sulfate and nitrate solutions evidenced the anion effects during the Cu upd process on Au electrodes.

PDEIS was also used for characterisation of Ag upd on polycrystalline Pt [244], Pb upd on polycrystalline Au and on Au coated with Se atomic layer [246], Bi upd on Au [247] and Pb upd on Te [248], where no adsorption pseudocapacitances were found in equivalent electric circuit of irreversible lead upd on tellurium.

2.26 Thermal Desorption Spectroscopy

The Thermal Desorption Spectroscopy (TPS), also known as Temperature Programmed Desorption (TPD) [249, 250] is an important tool to study for example hydrogen desorption kinetics in metal hydrides, but it was found throughout the literature that it can be also applied to M upd processes, although not extensively. Briefly, TPS consists in a non-isothermic analysis of desorption kinetics and it is used to obtain information on the energetics and kinetics of adsorbed particles. It involves heating resistively via thin tantalum or tungsten wires, a sample covered with one or more adsorbate(s), following a pre-defined temperature profile (mostly

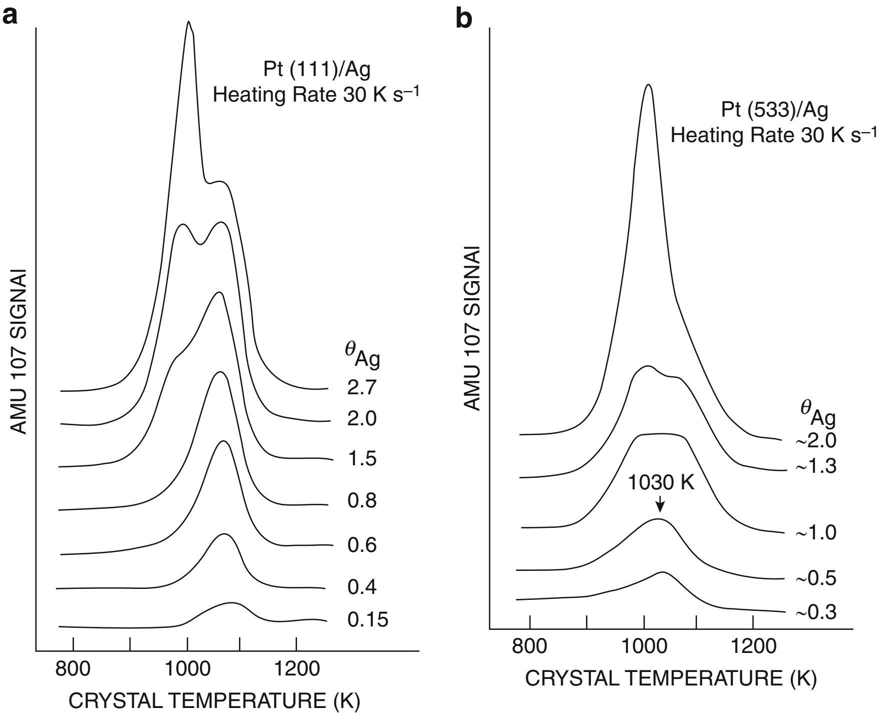

Fig. 2.36 Silver (AMU 107) thermal desorption spectra from (**a**) Pt(111) and (**b**) Pt (553) surfaces as a function of Ag coverage (Reprinted with permission from Ref. [251])

in a time-linear fashion) and simultaneously detecting the residual gas in the vacuum desorbed by the material by means of a mass analyser. The concentration of desorbing species is usually measured with a quadrupole mass spectrometer. As the temperature rises, certain absorbed species will have enough energy to escape and will be detected as a rise in pressure for a certain mass. The experiments are performed in a continuously pumped ultra-high vacuum (UHV) chamber. With increasing temperature, the desorption rate increases, eventually goes through a maximum, and drops back to zero as the surface is depleted of adsorbate. As a result one obtains a spectrum composed of several peaks of the desorption rate as a function of temperature.

Davies et al. [251] used TDS besides AES and LEED, to analyse the growth and chemisorptive properties of Ag and Au monolayers on platinum (111) and (553) surfaces. Only the system Ag/Pt will be mentioned here. AMU 107 TDS results from Ag-covered Pt(111) and Pt(553) surfaces, are presented in Fig. 2.36. A single, desorption peak centered at 1080 K from the Pt(111) substrate was observed up to an initial Ag coverage of 1ML (Fig. 2.36a), corresponding to the desorption of this layer. At coverages >1 ML a second, lower temperature peak is developed which becomes the dominant desorption feature at coverages >2 ML. This lower temperature peak was identified with desorption from subsequent monolayers. From these thermal desorption studies of Ag adlayers from the Pt substrates, the authors also determined that the Ag-Pt bond in the first monolayer was ~25 kJ mol^{-1} stronger (278 kJ mol^{-1}) than the Ag-Ag bond (253 kJ mol^{-1}) in the subsequent monolayers. Therefore, it could be expected that the first Ag monolayer deposited on the Pt surface would spread evenly over the surface to maximize the number of Ag-Pt bonds. The growth of Ag in this case proceeded via a Stranski-Krastanov mechanism. However, the TDS spectrum for Ag desorption from the Pt(553) surface (Fig. 2.36b), shows that both peaks were detected at initial coverages below 1 ML. At 1 ML the two peaks are of comparable intensity, and at 2 ML the lower temperature peak becomes the dominant feature. These observations indicated that silver was present as multilayer 3D crystallites, as would be expected from a system followed a Volmer-Weber growth mechanism.

Stickney and coworkers [252] reported studies about the influence of the halogen layer structure on the electrodeposition of silver on a Pt(100) surface pretreated with iodine, from aqueous perchloric acid solutions, employing TPS among other techniques. They analized the thermal desorption from various structures formed by electrodeposition of Ag onto Pt(100) $[c(\sqrt{2} \times 2\sqrt{2})]R45°$ I surface and found that the onset of atomic I desorption was retarded to some extent by the presence of electrodeposited silver and the desorption of metal deposits generally took place after most of the iodine had desorbed. The TDS spectrum for the system showed that whenever the packing density of deposited silver equaled that of a silver monolayer, silver desorption took place almost exclusively in a single, massive peak beginning near 950 K. Desorption of several silver monolayers ($\theta_{\mathrm{Ag}} >> 1$) and the initial stages of desorption of a silver monolayer evidently occurred in this single predominant process having a rate maximum at about 1000 K.

2.27 Glow Discharge Optical Emission Spectroscopy

Glow Discharge Optical Emission Spectroscopy (GDOES) has not been usually employed as a surface analysis technique for upd systems, but it is suitable for chemical analysis and surface depth-profiling characterization on solid materials including ultrathin films [253]. This technique is frequently used in combination with any of the well-known surface analysis methods, such as XPS, to obtain the composition of thin films as a function of depth.

The basic principles of GDOES [254, 255] are described here briefly. The glow discharge is a kind of plasma which is created by inserting two electrodes in a cell filled with gas at low pressure (e.g. 1 Torr), commonly Ar. A potential difference (of the order of 1 kV) is applied between the flat sample to be analyzed, which functions as cathode, and the anode (copper electrode). The glow discharge plasma is thus formed and viewed by one or more optical spectrometers. Argon ions, created in the negative glow of the plasma, are accelerated towards the sample where they bombard the surface, inducing an erosion process (sputtering). The atoms, removed from the sample surface, move into the glow discharge plasma.

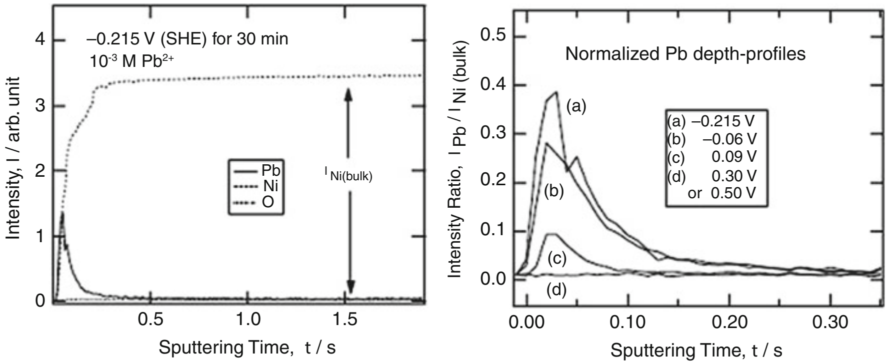

Fig. 2.37 (**a**) GDOES depth-profile for the Ni specimen polarized for 30 min at −0.215 V (SHE), (**b**) Normalized Pb depth-profiles of the Ni specimens polarized for 30 min at various potentials. Solution: 0.1 M $NaClO_4 + 10^{-2}$ M $HClO_4 + 10^{-3}$ M PbO (Reprinted with permission from Ref. [256])

Here they are excited through collisions with high energy electrons, metastable argon atoms and ions. The negative glow emits a characteristic radiation (optical emission spectrum) of the discharge gas and the elements present in the sample. This spectrum is recorded by an optical spectrometer and the concentration distribution of the different elements is deduced from the intensities of the characteristic spectral lines. Analytical applications of GDOES involve bulk elemental analysis, mostly of metals and alloys, as well as depth profile analysis of various coatings and surface-modified materials, acquiring the signal from each chemical element as a function of the sputtering time.

GDOES is a promising technique for ultrathin films analysis, including those formed by upd. Seo et al. [256] employed XPS and GDOES, together with electrochemical techniques, to confirm the evidence of Pb upd on Ni in acidic perchlorate solutions containing Pb^{2+} ions and its effect on the anodic dissolution and passivity of Ni. They reported that the upd of lead on Ni in the potential range larger than −0.215 V (SHE) corresponding to the equilibrium potential of the Pb^{2+} (10^{-3} M)/Pb electrode, was confirmed by XPS and GDOES analyses, indicating that the upd process occurred on Ni surface in the potential range of the active dissolution and active/passive transition. The GDOES results are shown in Fig. 2.37. The typical depth-profile of the Ni sample, polarized for 30 min at −0.215 V (SHE) in 0.1 M $NaClO_4 + 10^{-2}$ M $HClO_4 + 10^{-3}$ M PbO solution, evidenced the presence of lead on the uppermost surface (Fig. 2.37a). In order to compare the difference in Pb depth-profile between the Ni specimens, graphics of the intensity ratio, i.e. the intensity of Pb, I_{Pb}, normalized by dividing it with the Ni intensity in bulk, $I_{Ni(bulk)}$, vs the sputtering time were performed.

Figure 2.37b exhibits the normalized Pb depth-profiles of the Ni specimens polarized for 30 min at various potentials. It was observed that the maximum of the intensity ratio, $I_{Pb}/I_{Ni(bulk)}$, decreased with increasing polarization potential from −0.215 to 0.09 V (vs. SHE) and no Pb was detected for the Ni specimen polarized at 0.30 or 0.50 V (vs. SHE) in the passive region. Both the XPS and

GDOES results indicated that lead was present on the Ni surface in the potential region of hydrogen evolution and active dissolution, while there was no lead on the Ni surface in the complete passive region.

2.28 Underpotential Deposition in Nuclear Chemistry

Electrochemical methods for the isolation and separation of radioelements in weightless amounts are popular because of their cleanliness. The deposited radioisotopes may be desorbed from the electrodes again or may form firmly adhering uniform layers, with which radioactive energy or intensity measurements can be performed. The deposition methods are either electroless or they make use of electric current (electrolytic methods). A valuable overview on the application of electrochemical methods in radiochemistry until the middle 1950s can be found in the book of E. Broda and T. Schönfeld. [257]. The practical aspects have been summarized by Rogers [258]. This author has performed depositions in volumes of 0.01 ml. A more recent overview on theoretical aspects of this problem can be found in the article of Eichler and Kratz [259].

Due to its ability to sense very small cation concentrations, the underpotential deposition phenomenon has found application in nuclear chemistry and emerges as an interesting method for separating trace levels of a radioactive substance.

From theoretical predictions, elements with atomic number in the range 108–116 are expected to be partially very noble metals and therefore their electrochemical deposition on suitable electrode materials from aqueous solutions may be used as a possible method for their isolation [260].

Eichler and Kratz [259] have shown by means of theoretical calculations that the potential associated with the electrochemical deposition of radionuclides in metallic form from solutions of extremely small concentration is strongly influenced by the choice of the electrode material. Based on a previous work of Byrne and Rogers [261], these authors proposed a modified Nernst equation for a thermodynamic description of the electrodeposition of radiotracers in the upd range. This equation is based on physical properties (partial molar adsorption enthalpy and entropy) of the deposited metal A and the electrode metal B and lead to predictions for electrode potentials for depositions of 50 %, $E_{50\%}$:

$$E_{50\%} = E^0 - \frac{\Delta\overline{H}(\text{A-B}) - T\Delta\overline{S}_{\text{vib}}}{zF} - \frac{RT}{zF}\ln\frac{A_{\text{m}}}{1000} \tag{2.4}$$

Where E^0 is the standard electrode potential, $\Delta\overline{H}(\text{A-B})$ is the partial molar net adsorption enthalpy, which corresponds to the enthalpy difference associated with the transformation of 1 mol of the pure metal A in its standard state into the state of "zero coverage", where the interaction of A-B is strong and the interaction of A-A negligible. In the state of "zero coverage" deposition occurs in the upd range. ΔS_{vib} is the difference of vibrational entropies in the above mentioned states, and A_{m} is

Table 2.2 $E_{50\%}$ values. and E^0, as defined in Eq. (2.4) for Hg, Tl, Pb, Bi, and Po at different electrode surfaces. All potentials are referred to Ag/AgCl electrode

$E_{50\%}$(mV) Electrode	Ni	Cu	Pd	Ag	Pt	Au	E^0(mV)
Ion							
Hg^{2+}	660	635	1145	620	965	710	595
Tl^{+}	555	315	1915	380	1425	655	−530
Pb^{2+}	−235	−380	450	−380	170	−305	−320
Bi^{3+}	300	145	790	125	585	175	120
Po^{2+}	775	330	1035	355	720	670	425
Po^{4+}	600	375	730	340	575	545	565

Data taken from Ref. [262]

the surface occupied by 1 mol of A atoms as a monolayer on a metal electrode B. Calculations for the deposition of elements 112–115 and their homologs Hg, Tl, Pb, Bi and Po on Ni -, Cu-, Pd -, Ag-, Pt- and Au- electrodes were carried out, confirming the influence of the nature of the electrode material on the deposition potential. Hummrich et al. [262] recalculated the $E_{50\%}$ values from [259], which are presented in Table 2.2 together with the standard electrode potentials E^0. All the potentials are referred to the Ag/AgCl reference electrode. It is found that for Pd, and in some cases Pt or Au, particularly large, positive values of $E_{50\%}$ were calculated, larger than the standard electrode potentials tabulated for these elements. This fact indicates that these electrode materials are an excellent choice for practical applications enabling the electrochemical deposition of this kind of elements from aqueous solutions.

Hevesy and Paneth [263] performed the first studies of Po underpotential deposition on gold electrodes and introduced the quantity denominated "critical potential", E_{crit}. This value refers to the potential at which a significant electrodeposition of a radiotracer on a metal surface occurs. The E_{crit} as well as the experimental quantity defined above $E_{50\%}$ can be considered as a measure for the strength of the interaction between the metal A and the electrode material B. These quantities are discussed in more detail below.

A specific electrolytic cell has to be designed for the present type of studies, because electrodeposition must be produced in a fast way due to the very short life of the isotopes which have to be deposited. Therefore, a small ratio of an electrolyte volume to electrode area, intensive stirring and a high temperature were considered by Hummrich et al. [262]. The electrode set-up and electrolytic cell used by these authors are depicted in Fig. 2.38. The electrolytic cell was made of polyether-ether-ketone with two slots for working electrodes, which were shaped in the form of foils on which the electrodeposition took place. The electrolyte volume was small, 1 mL. A large stir bar was placed between the two metal foil working electrodes, to make possible a vigorous stirring, reducing simultaneously the ratio of electrolyte volume to electrode. Electrolyte in- and outlets were provided for online experiments and were plugged in the offline experiments, and a positive temperature coefficient resistor (PCT) was mounted behind one working electrode.

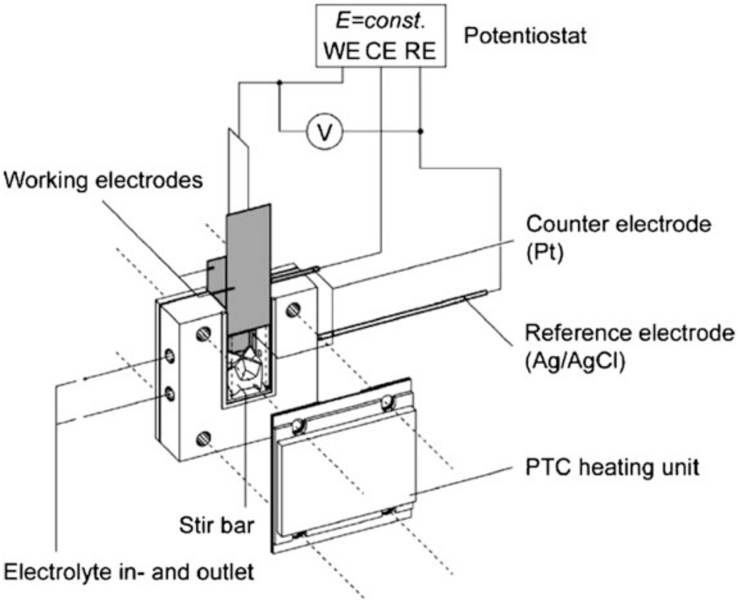

Fig. 2.38 Potentiostatic three electrode set-up and electrolytic cell for fast electrochemical deposition experiments with short-lived isotopes. *WE*: working electrode, *CE*: counter electrode, *RE*: reference electrode (Taken from Ref. [262] With permission)

With this set-up, Hummrich et al. [262] performed offline and online experiments. The term offline refers to experiments performed with relatively long lived homologues of the super-heavy elements, while the term online refers to experiments coupled to the nuclear facility. The first ones served to investigate the appropriate potentials for electrochemical deposition and the electrodeposition velocity of several standard radiotracers. This was achieved via measurement of the γ activity of the electrodes, which was compared with the measured count rates of a standard sample that was prepared by pipetting a definite activity on a glass fiber filter.

In Figure 2.39, the deposition yield of Pb on Pd, Ni, Cu and palladinated Ni (Ni (Pd)) surfaces is plotted versus the electrode potential, where the critical potentials E_{crit} were determined by the tangent method as proposed by Joliot [264]. In this method, the intersection of the tangent of the flat part of the curve (before deposition starts) and of the tangent that goes through the point of inflection of the gradient part of the curve, defines the E_{crit}. Starting at this potential, the deposition sets in and approaches eventually 100 %. From the potential curve, $E_{50\%}$ can be also deduced.

For the deposition of Pb on Pd the E_{crit} and $E_{50\%}$ values were +125/−20 mV, on Ni −150/−250 mV, and on Cu −350/−460 mV, respectively. Comparing these measured values with the calculated hypothetical Nernst potential (−530 mV vs. Ag/AgCl; 3 M KCl) for lead deposition on lead, it can be deduced that the

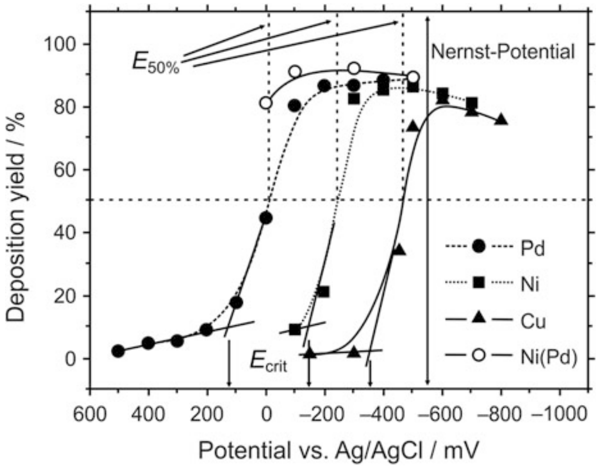

Fig. 2.39 Determination of critical potentials (E_{crit}) and $E_{50\%}$-values for the deposition of ^{212}Pb on different electrode materials from 0.1 M HCl. A hypothetical Nernst potential for lead deposition on lead is also indicated (Reprinted with permission from Ref. [262])

underpotential deposition phenomenon is present in all cases. Especially for the deposition of Pb on Pd, the effect is more pronounced because it shows the strongest underpotential shift, namely more than 600 mV more positive than the Nernst potential. Then the electrode with the deposited product was analyzed by α – spectrometry and the results indicated that more than 97 % of the radioactivity of Pb remained on the Pd electrodes and therefore Pd should then be used as the electrode material.

Coming back to the previous studies of Eichler and Kratz [259], these authors compared theoretical $E_{50\%}$-values with the measured E_{crit} data, and suggested that the predictions seemed to be upper limits for the “critical potentials”. In that sense, the characteristic quantities $E_{50\%}$ can be seen as useful predictions of the largely different “driving forces” for electrochemical depositions depending on the nature of the microcomponent A and on the choice of the electrode material B. On the other hand, in the work of Hummrich et al. [262] the highest measured $E_{50\%}$ values were tentatively compared with the theoretical calculations in Table 2.2. As examples, it is found that the predicted large underpotential deposition values of Pb on Pd and Pt were confirmed, although the measured values were lower than the predicted ones. The predicted $E_{50\%}$ values for the deposition on Cu and Ni were within 100 mV close to the measured values, while the calculated value for Au was much too low.

Hummrich et al. [262] also performed online experiments, which involved a set-up suited to perform electrodeposition experiments with accelerator produced isotopes. These experiments involved the following steps: (1) fast transport of the produced isotopes to the chemistry set-up, (2) transfer of the isotopes from the gas into the aqueous phase, (3) transport into the electrolytic cell, (4) electrodeposition onto the electrodes, (5) preparation of samples for decay spectrometry, (6) transport of the electrodes to a detector set-up for α-spectrometry and identification of the element by detection of its nuclear decay.

In a first type of online experiments, the electrolytic cell with the foil electrodes was used and the transport of the metal foil electrodes to detectors was performed manually. In a second type of online experiments, the working electrodes were long metal tapes which allowed for moving the spot with the deposited radioactivity very fast to a detector array, i.e. these tapes were then be pulled through the electrolytic cell in order to transport the deposited activities in front of α-detectors. This perspective was taken with the aim of developing a fully automatised system and to improve the detection probability increasing the number of detectors. Finally, these authors mentioned that a good candidate for first electrodeposition experiments in the field of the super heavy elements could be ^{270}Hs (Hassium, atomic number 108), which has a sufficient long half-life time (22 s).

References

1. Budevski E, Staikov G, Lorenz WJ (1996) Electrochemical phase formation. An introduction to the initial stages of metal deposition. Weinheim, VCH
2. Kolb DM, Przasnyski M, Gerischer H (1974) J Electroanal Chem 54:25
3. Szabó S (1991) Int Rev Phys Chem 10:207
4. Budevski E, Staikov G, Lorenz WJ (2000) Electrochim Acta 45:2559
5. Kolb DM (1978) Physical and electrochemical properties of metal monolayers on metallic substrates. In: Gerischer H, Tobías CW (eds) Advances in electrochemistry and electrochemical engineering. Wiley, New York, p 125
6. Herrero E, Buller LJ, Abruña HD (2001) Chem Rev 101:1897
7. Sudha V, Sangaranarayanan MV (2005) J Chem Sci 117:207
8. Aramata A (1997) Underpotential deposition on single-crystal metals. In: Bockris JO'M, White RW, Conway BE (eds) Modern aspects of electrochemistry, number 31. Plenum Press, New York, p 181
9. Leiva EPM (1996) Electrochim Acta 41:2185
10. Adžic RR (1984) Electrocatalytic properties of the surfaces modified by foreign metal adatoms. In: Gerischer H, Tobías CW (eds) Advances in electrochemistry and electrochemical engineering, vol 13. Wiley, New York, p 159
11. Kokkinidis G (1986) J Electroanal Chem 201:217
12. Cullity BD (1978) Elements of X-ray diffraction, 2nd edn. Addison-Wesley, Reading, p 506
13. García S, Salinas D, Mayer C, Schmidt E, Staikov G, Lorenz WJ (1998) Electrochim Acta 43:3007
14. Chen C-H, Vesecky SM, Gewirth AA (1992) J Am Chem Soc 114:451
15. Mrozek P, Sung Y-E, Han M, Gamboa-Aldeco M, Wieckowski A, Chen C-H, Gewirth AA (1995) Electrochim Acta 40:17
16. Uchida H, Miura M, Watanabe M (1995) J Electroanal Chem 386:261
17. Ogaki K, Itaya K (1995) Electrochim Acta 40:1249
18. Rooryck V, Reniers F, Buess-Herman C, Attard GA, Yang X (2000) J Electroanal Chem 482:93
19. Schulze JW, Dickertmann D (1976) Surf Sci 54:489
20. Dickertmann D, Koppitz FD, Schulze JW (1976) Electrochim Acta 21:967
21. Zei M, Qiao G, Lempfuhl G, Kolb DM (1987) Ber Bunsenges Phys Chem 91:3494
22. Beckmann HO, Gerischer H, Kolb DM, Lempfuhl G (1977) Symp Faraday Soc 12:51
23. Hachiya T, Honbo H, Itaya K (1991) J Electroanal Chem 315:275
24. Omar IH, Pauling HJ, Jüttner K (1993) J Electrochem Soc 140:2187

25. Borges GL, Kanazawa KK, Gordon JG II, Ashley K, Richer J (1994) J Electroanal Chem 364:281
26. Shi Z, Lipkowski J (1994) J Electroanal Chem 364:289
27. Shi Z, Lipkowski J (1994) J Electroanal Chem 365:303
28. Shi Z, Wu S, Lipkowski J (1995) Electrochim Acta 40:9
29. Magnussen OM, Hotlos J, Beitel G, Kolb DM, Behm RJ (1991) J Vac Sci Technol B 9:969
30. Magnussen OM, Hotlos J, Nichols RJ, Kolb DM, Behm RJ (1990) Phys Rev Lett 64:2929
31. Kolb DM (1994) Ber Bunsenges Phys Chem 98:1421
32. Manne S, Hansma PK, Massie J, Elings VB, Gewirth AA (1991) Science 251:183
33. Parry DB, Samant MG, Seki H, Philpott MR (1993) Langmuir 9:1878
34. Blum L, Abruña HD, White J, Gordon JG II, Borges GL, Samant MG, Melroy OR (1986) J Chem Phys 85:6732
35. Melroy OR, Samant MG, Borges GL, Gordon JG II, Blum L, White JH, Albarelli MJ, McMillan M, Abruña HD (1988) Langmuir 4:728
36. Tadjeddine A, Guay D, Ladouceur M, Tourillon G (1991) Phys Rev Lett 66:2235
37. Gordon JG, Melroy OR, Toney MF (1995) Electrochim Acta 40:3
38. Nakai Y, Zei MS, Kolb DM, Lempfuhl G (1984) Ber Bunsenges Phys Chem 88:340
39. Kolb DM (2002) Surf Sci 500:722
40. Randler RJ, Kolb DM, Ocko BM, Robinson IK (2000) Surf Sci 447:187
41. Möller FA, Magnussen OM, Behm RJ (1995) Phys Rev B 51:2484
42. Cappadonia M, Linke U, Robinson KM, Schmidberger J, Stimming U (1996) J Electroanal Chem 405:227
43. Kuzume A, Herrero E, Feliu JM, Nichols RJ, Schiffrin DJ (2004) J Electroanal Chem 570:157
44. Bowles BJ (1965) Electrochim Acta 10:717
45. Bowles BJ (1965) Electrochim Acta 10:731
46. Bowles BJ, Cranshaw TE (1965) Phys Lett 17:258
47. Bowles BJ (1966) Nature 212:1456
48. Bowles BJ (1970) Electrochim Acta 15:589
49. Bowles BJ (1970) Electrochim Acta 15:737
50. Horányi G, Vértes G (1973) J Electroanal Chem 45:295
51. Horányi G (1974) J Electroanal Chem Interfacial Electrochem 55:45
52. Horanyi G (2004) Radiotracer studies of interfaces. Elsevier B.V, The Netherlands
53. Waszczuk P, Wnuk A, Sobkowski J (1999) Electrochim Acta 44:1789
54. Poškus D, Agafonovas G (2000) J Electroanal Chem 493:50
55. Zelenay P, Rice-Jackson LM, Wieckowski A, Gawlowski J (1991) Surf Sci 256:253
56. Hölzle MH, Retter U, Kolb DM (1994) J Electroanal Chem 371:101
57. Schultze JW, Dickertmann D (1976) Surf Sci 54:489
58. Bewick A, Fleischmann M, Thirsk HR (1962) Trans Faraday Soc 58:2200
59. Jüttner K, Lorenz WJ (1980) Z Phys Chem Neue Folge 122:163
60. Staikov G, Jüttner K, Lorenz WJ, Budevski E (1994) Electrochim Acta 39:1019
61. Schmidt E, Siegenthaler H (1969) Helv Chim Acta 52:2245
62. Schmidt E, Wüthrich N (1970) J Electroanal Chem 28:349
63. Lorenz WJ, Hermann HD, Wüthrich N, Hilbert F (1974) J Electrochem Soc 121:1167
64. Kolb DM, Schneider J (1986) Electrochim Acta 31:929
65. Hamelin A (1995) J Electroanal Chem 386:1
66. Vitanov T, Popov A, Sevastyanov ES (1982) J Electroanal Chem 142:289
67. Bruckenstein S, Napp DT (1968) J Am Chem Soc 90:6303
68. Tindall GW, Bruckenstein S (1968) Anal Chem 40:1051
69. Cadle SH, Bruckenstein S (1971) Anal Chem 43:932
70. Tindall GW, Bruckenstein S (1971) Electrochim Acta 16:245
71. Opekar F, Beran P (1976) J Electroanal Chem 69:1
72. Bruckenstein S, Miller B (1977) Acc Chem Res 10:54
73. Swathirajan S, Bruckenstein S (1983) Electrochim Acta 28:865

74. Mascaro LH, Santos MC, Machado SAS, Avaca LA (1997) J Chem Soc Faraday Trans 93:3999
75. Cadle SH, Bruckenstein S (1972) Anal Chem 44:1993
76. Vicente VA, Bruckenstein S (1973) Anal Chem 45:2036
77. Riedhammer TM, Melnicki LS, Bruckenstein S (1978) Zeit Phys Chem 111:177
78. Sherwood WG, Bruckenstein S (1978) J Electrochem Soc 125:1098
79. Santos MC, Mascaro LH, Machado SA (1998) Electrochim Acta 43:2263
80. Bruckenstein S, Swathirajan S (1985) Electrochim Acta 30:851
81. Buttry DA (1991) Chapter 10: the quartz crystal microbalance as an in situ tool in electrochemistry. In: Abruña HD (ed) Electrochemical interfaces. VCH Publishers, Inc, New York, p 529
82. Bruckenstein S, Shay M (1985) Electrochim Acta 30:1295
83. Melroy O, Kanazawa K, Gordon JG II, Buttry D (1986) Langmuir 2:697
84. Deakin MR, Melroy O (1988) J Electroanal Chem 239:321
85. Deakin MR, Li TT, Melroy OR (1988) J Electroanal Chem 243:343
86. Watanabe M, Uchida H, Miura M, Ikeda N (1995) J Electroanal Chem 384:191
87. Uchida H, Hiei M, Watanabe M (1998) J Electroanal Chem 452:97
88. Toney MF, Howard JN, Richer J, Borges GL, Gordon JG, Melroy OR, Yee D, Sorensen LB (1995) Phys Rev Lett 75:4472
89. Wu S, Shi Z, Lipkowski J, Hitchcock AP, Tyliszczak T (1997) J Phys Chem B 101:10310
90. White JH, Albarelli MJ, Abruña HD, Blum L, Melroy OR, Samant MG, Borges GL, Gordon JG (1988) J Phys Chem 92:4432
91. Inzelt G, Horányi G (2000) J Electroanal Chem 491:111
92. Binnig G, Rohrer H, Gerber C, Weibel E (1982) Phys Rev Lett 49:57
93. Hansma PK, Tersoff J (1987) J Appl Phys 61:R1
94. Sonnenfeld R, Hansma PK (1986) Science 232:211
95. Siegenthaler H (1992) STM in electrochemistry. In: Güntherrodt H-J, Wiesendanger R (eds) Scanning tunneling microscopy II. Springer, Berlin/Heidelberg, p 7
96. Gewirth AA, Niece BK (1997) Chem Rev 97:1129
97. Itaya K (1998) Prog Surf Sci 58:121
98. Kolb DM (2000) Electrochim Acta 45:2387
99. Tao NJ, Li CZ, He HX (2000) J Electroanal Chem 492:81
100. Christensen PA, Hamnet A (1994) Techniques and mechanisms in electrochemistry. Blackie Academic & Professional (An imprint of Chapman & Hall), Glasgow
101. Lustenberger P, Rohrer H, Christoph R, Siegenthaler H (1988) J Electroanal Chem 243:225
102. Hamelin A, Gao X, Weaver MJ (1992) J Electroanal Chem 323:361
103. Dietterle M, Will T, Kolb DM (1995) Surf Sci 342:29
104. Wolf JF, Vicenzi B, Ibach H (1991) Surf Sci 249:233
105. Poensgen M, Wolf JF, Frohn J, Giesen M, Ibach H (1992) Surf Sci 274:430
106. Hachiya T, Itaya K (1992) Ultramicroscopy 42–44:445
107. Itaya K (1992) Nanotechnology 3:185
108. Chen C, Gewirth AA (1992) Ultramicroscopy 42–44:437
109. Esplandiu MJ, Schneeweiss MA, Kolb DM (1999) Phys Chem Chem Phys 1:4847
110. Ikemiya N, Yamada K, Hara S (1996) Surf Sci 348:253
111. García SG (1997) Ph.D. thesis, Universidad Nacional del Sur, Bahía Blanca
112. Zei MS, Qiao G, Lehmpfuhl G, Kolb DM (1987) Ber Bunsenges Phys Chem 91:349
113. Garcia SG, Salinas D, Mayer C, Vilche JR, Pauling H-J, Vinzelberg S, Staikov G, Lorenz WJ (1994) Surf Sci 316:143
114. Batina N, Will T, Kolb DM (1992) Faraday Discuss 94:93
115. Hotlos J, Magnussen OM, Behm RJ (1995) Surf Sci 335:129
116. Vasiljevic N, Viyannalage LT, Dimitrov N, Sieradzki K (2008) J Electroanal Chem 613:118
117. Binnig G, Quate F, Gerber C (1986) Phys Rev Lett 56:930
118. Binnig G, Gerber C, Stoll E, Albrecht TR, Quate CF (1987) Europhys Lett 3:1281

119. Binnig G (1992) Ultramicroscopy 42–44:7
120. Bhushan B, Marti O (2004) Scanning probe microscopy – principle of operation, instrumentation, and probes. In: Brushan B (ed) Handbook of nanotechnology, 2nd edn. Springer, Heidelberg, p 591
121. Meyer E (1992) Prog Surf Sci 41:3
122. Butt H-J, Cappella B, Kappl M (2005) Surf Sci Rep 59:1
123. Manne S, Massie J, Elings VB, Hansma PK, Gewirth AA (1991) J Vac Sci Technol B 9:950
124. Held G (2012) Low-energy electron diffraction: crystallography of surfaces and interfaces. In: Schäfer R, Schmidt PC (eds) Methods in physical chemistry. Wiley-VCH, Weinheim, Chapter 20
125. Henk J (2002) Theory of low-energy electron diffraction and photoelectron spectroscopy from ultra-thin films. In: Nalwa S (ed) Handbook of thin film materials, vol 2: Characterization and spectroscopy of thin films. Academic, CA, San Diego, Chapter 10
126. Gallon TE, Matthew JAD (1972) Rev Phys Technol 3:31
127. Holloway PH (1980) Fundamentals and applications of auger electron spectroscopy. In: Marton L, Marton C (eds) Advances in electronics and electron physics, vol 54. Academic, New York, p 241
128. Bubert H, Rivière JC, Werner WSM (2011) Auger electron spectroscopy (AES). In: Friedbacher G, Bubert H (eds) Surface and thin film analysis: a compendium of principles, instrumentation, and applications, 2nd edn. Wiley-VCH Verlag GmbH & Co. KGaA, Weinheim, Chapter 3
129. Madden HH (1981) J Vac Sci Technol 18:677
130. Shchukarev A (2006) Adv Col Interf Sci 122:149
131. Venezia AM (2003) Catal Today 77:359
132. Fadley CS (2010) J Electron SpectroscRelat Phenom 178–179:2
133. Zei MS, Nakai Y, Weick D, Lehmpfuhl G (1985) Surf Sci 152/153:254
134. Rehr JJ, Albers RC (2000) Rev Mod Phys 72:621
135. Teo B-K (1981) EXAFS spectroscopy: techniques and applications. In: Teo B-K, Joy DC (eds) EXAFS spectroscopy: techniques and applications. Springer Science + Business Media, New York, Chapter 3
136. Lee PA, Citrin PH, Eisenberger P, Kincaid BM (1981) Rev Mod Phys 53:769
137. Samant MG, Borges G, Melroy OR (1993) J Electrochem Soc 140:421
138. Chabala ED, Ramadan AR, Brunt T, Rayment T (1996) J Electroanal Chem 412:67
139. Lee D, Rayment T (1999) Phys Chem Chem Phys 1:4389
140. Ramadan AR, Rayment T (2001) J Electroanal Chem 503:28
141. Kondo T, Morita J, Okamura M, Saito T, Uosaki K (2002) J Electroanal Chem 532:201
142. Adžić RR, Wang JX, Ocko BM, McBreen J (2010) EXAFS, XANES, SXS. In: Vielstich W, Gasteiger HA, Lamm A, Yokokawa H (eds) Handbook of fuel cells – fundamentals, technology and applications. Wiley, New York, p 679
143. Chabala ED, Harji BH, Rayment T, Archer MD (1992) Langmuir 8:2028
144. Matsui J, Mizukil J (1993) Annu Rev Mater Sci 23:295
145. Segmüller A (1987) Thin Solid Films 154:33
146. Samant MG, Toney MF, Borges GL, Blum L, Melroy OR (1988) J Phys Chem 92:220
147. Herrero E, Glazier S, Abruña HD (1998) J Phys Chem B 102:9825
148. Miles R (1983) Surf Interf Anal 5:43
149. Iwasita T, Nart FC (1997) Prog Surf Sci 55:271
150. Bewick A (1983) J Electroanal Chem 150:481
151. Hummel RE, Dubroca T (2013) Differential reflectance spectroscopy in analysis of surfaces. In: Meyers RA (ed) Encyclopedia of analytical chemistry. Wiley, New York
152. McIntyre JDE, Aspnes DE (1971) Surf Sci 24:417
153. Kolb DM (1988) Ber Bunsenges Phys Chem 92:1175
154. Kolb DM, Leutloff D, Przasnyski M (1975) Surf Sci 47:622
155. Kolb DM, Kötz R (1977) Surf Sci 64:698

156. McIntyre JDE, Kolb DM (1970) Symp Faraday Soc 4:99
157. Borensztein Y, Abelès F (1985) Thin Solid Films 125:129
158. Kolb DM (1988) UV-visible reflectance spectroscopy. In: Gale RJ (ed) Spectroelectrochemistry: theory and practice. Plenum Press, New York, p 87, Chapter 4
159. Bard AJ, Faulkner LR (2001) Electrochemical methods. Fundamentals and applications, 2nd edn. Wiley, New York, p 698
160. Shannon VL, Koos DA, Richmond GL (1987) J Phys Chem 91:5548
161. Yagi I, Lantz JM, Nakabayashi S, Corn RM, Uosaki K (1996) J Electroanal Chem 401:95
162. Richmond GL, Robinson JM, Shannon VL (1988) Prog Surf Sci 28:1
163. Richmond GL (1992) Second harmonic generation as an in-situ probe of single crystal electrode surfaces. In: Gerischer H, Tobías CW (eds) Advances in electrochemical science and engineering. VCH Verlagsgesellschaft, Weinheim, p 141
164. Corn RM, Higgins DA (1994) Chem Rev 94:107
165. Richmond LR (1991) Investigations of electrochemical interfaces by nonlinear optical methods. In: Abruña HD (ed) Electrochemical interfaces. Modern techniques for in-situ interface characterization. VCH Publishers Inc, New York, p 265
166. Richmond GL, Bradley RA (1995) Surface second harmonic generation studies of single crystal metal surfaces. In: Dai H-L, Ho W (eds) Laser spectroscopy and photochemistry on metal surface. World Scientific, Singapore, p 132, Chapter 4
167. Lakkaraju S, Bennahmias MJ, Borges GL, Gordon JG II, Lazaga M, Stone BM, Ashley K (1990) App Opt 29:4943
168. Koos DA, Richmond GL (1992) J Phys Chem 96:3770
169. Walters MJ, Pettit CM, Roy D (2001) Phys Chem Chem Phys 3:570
170. Brolo AG, Irish DE, Smith BD (1997) J Mol Struct 405:29
171. Haynes CL, McFarland AD, Van Duyne RP (2005) Anal Chem 77:338A
172. Tian Z-Q, Ren B, Wu D-Y (2002) J Phys Chem 106:9463
173. Tian ZQ, Ren B (2003) Raman spectroscopy of electrode surfaces. In: Bard AJ, Stratmann M, Unwin PR (eds) Encyclopedia of electrochemistry, instrumentation and electroanalytical chemistry, vol 3. Wiley-VCH, New York, pp 572–659
174. Pemberton JE (1991) Surface enhanced raman scattering. In: Abruña HD (ed) Electrochemical interfaces: modern techniques for in-situ interface characterization. VCH Publishers, Inc, New York, p 193
175. Otto A (1991) J Raman Spectrosc 22:743
176. Sharma B, Frontiera RR, Henry A-I, Ringe E, Van Duyne RP (2012) Mater Today 15:16
177. Leung L-WH, Gosztola D, Weaver MJ (1987) Langmuir 3:45
178. Leung L-WH, Weaver MJ (1987) J Electroanal Chem 217:367
179. Fleischmann M, Tian ZQ (1987) J Electroanal Chem 217:385
180. Jüttner K, Siegenthaler H (1978) Electrochim Acta 23:971
181. Siegenthaler H, Jüttner K, Schmidt E, Lorenz WJ (1978) Electrochim Acta 23:1009
182. Schmidt E, Siegenthaler H (1983) J Electroanal Chem 150:59
183. Carnal D, Oden PI, Müller U, Schmidt E, Siegenthaler H (1995) Electrochim Acta 40:1223
184. Siegenthaler H, Jüttner K (1979) Electrochim Acta 24:109
185. Vitanov T, Popov A, Staikov G, Budevski E, Lorenz WJ, Schmidt E (1986) Electrochim Acta 31:981
186. Popov A, Dimitrov N, Velev O, Vitanov T, Budevski E (1989) Electrochim Acta 34:265
187. Popov A, Dimitrov N, Kashchiev D, Vitanov T, Budevski E (1989) Electrochim Acta 34:269
188. Dimitrov N, Popov A, Kashchiev D, Vitanov T, Budevski E (1991) Electrochim Acta 36:1259
189. Dimitrov N, Popov A, Vitanov T, Budevski E (1991) Electrochim Acta 36:2077
190. Popov A, Dimitrov N, Kashchiev D, Vitanov T, Budevski E (1993) Electrochim Acta 38:387
191. Dimitrov N, Popov A, Kashchiev D, Vitanov T (1994) Electrochim Acta 39:957
192. Popov A, Dimitrov N, Vitanov T, Kashchiev D, Budevski E (1995) Electrochim Acta 40:1495

193. Schmidt U, Vinzelberg S, Staikov G (1996) Surf Sci 348:261
194. Engelsmann K, Lorenz WJ, Schmidt E (1980) J Electroanal Chem 114:1
195. Green MP, Hanson KJ, Scherson DA, Xing X, Richter M, Ross PN, Carr R, Lindau I (1989) J Phys Chem 93:2181
196. Green MP, Hanson KJ, Carr R, Lindau I (1990) J Electrochem Soc 137:3493
197. Green MP, Hanson KJ (1991) Surf Sci Lett 259:L743
198. Schmidt E, Christen M, Beyeler P (1973) J Electroanal Chem 42:275
199. Bort H, Jüttner K, Lorenz WJ, Staikov G (1983) Electrochim Acta 28:993
200. Martins ME, Hernández-Creus A, Salvarezza RC, Arvía AJ (1994) J Electroanal Chem 375:141
201. García SG, Salinas DR, Staikov G (2005) Surf Sci 576:9
202. Staikov G, García SG, Salinas DR (2010) ECS Trans 25:3
203. Ambrusi RE, Staikov G, García SG (2014) J Electroanal Chem 728:130
204. Schultze JW, Koppitz FD, Lohrengel MM (1974) Ber Bunsenges Phys Chem 78:693
205. Vidu R, Hara S (1999) Scr Mater 41:617
206. Vidu R, Hara S (1999) J Electroanal Chem 475:171
207. Vidu R, Hara S (2000) Surf Sci 452:229
208. Vidu R, Hirai N, Hara S (2001) Phys Chem Chem Phys 3:3320
209. del Barrio MC, García SG, Salinas DR (2004) Electrochem Commun 6:762
210. del Barrio MC, García SG, Mayer CE, Salinas DR (2008) Surf Interface Anal 40:22
211. del Barrio MC, Salinas DR, García SG (2014) Electrochim Acta 130:164
212. Hirai N, Tanaka H, Hara S (1998) Appl Surf Sci 130–132:506
213. del Barrio MC, García SG, Salinas DR (2009) Electrochim Acta 55:451
214. García SG, Salinas DR (2007) Nanoelectrochemistry: 2D and 3D metal-phase formation processes. In: Mariscal MM, Dassie SA (eds) Recent advances in nanoscience. Research Signpost, Kerala, pp 103–122, Chapter 4
215. Lay MD, Varazo K, Srisook N, Stickney JL (2003) J Electroanal Chem 554:221
216. Lay MD, Stickney JL (2003) J Am Chem Soc 125:1352
217. Stafford GR, Bertocci U (2006) J Phys Chem B 110:15493
218. Shin JW, Bertocci U, Stafford GR (2010) J Phys Chem C 114:7926
219. Stafford GR, Bertocci U (2007) J Phys Chem C 111:17580
220. Brunt TA, Rayment T, O'Shea SJ, Welland ME (1996) Langmuir 12:5942
221. Brankovic SR, Wang JX, Adžic RR (2001) Surf Sci 474:L173
222. Viyannalage LT, Vasilic R, Dimitrov N (2007) J Phys Chem C 111:4036
223. Gokcen D, Bae S-E, Brankovic SR (2010) J Electrochem Soc 157:D582
224. Gokcen D, Bae S-E, Brankovic SR (2011) ECS Trans 35:11
225. Huang BM, Colletti LP, Gregory BW, Anderson JL, Stickney JL (1995) J Electrochem Soc 142:3007
226. Colletti LP, Flowers BH Jr, Stickney JL (1998) J Electrochem Soc 145:1442
227. Stickney JL (2002) Electrochemical atomic layer epitaxy (EC-ALE): nanoscale control in the electrodeposition of compound semiconductors. In: Kolb DM, Alkire R (eds) Advances in electrochemical science and engineering, vol 7. Wiley-VCH, Weinheim, p 1
228. Mathe MK, Cox SM, Flowers BH Jr, Vaidyanathan R, Pham L, Srisook N, Happek U, Stickney JL (2004) J Cryst Growth 271:55
229. Gregory BW, Stickney JL (1991) J Electroanal Chem 300:543
230. Gregory BW, Suggs DW, Stickney JL (1991) J Electrochem Soc 138:1279
231. Suggs DW, Stickney JL (1993) Surf Sci 290:362
232. Suggs DW, Stickney JL (1993) Surf Sci 290:375
233. Varazo K, Lay MD, Sorenson TA, Stickney JL (2002) J Electroanal Chem 522:104
234. Pezzatini G, Caporali S, Innocenti M, Foresti ML (1999) J Electroanal Chem 475:164
235. Forni F, Innocenti M, Pezzatini G, Foresti ML (2000) Electrochim Acta 45:3225
236. Conway BE, Birss V, Wojtowicz J (1997) J Power Sources 66:1
237. Girija TC, Sangaranarayanan MV (2006) J Appl Electrochem 36:531

238. Fujishima A, Masuda H, Honda K (1979) Chem Lett 8:1063
239. Yoshihara S, Ueno M, Nagae Y, Fujishima A (1988) Electrochim Acta 33:1685
240. Rosencwaig A (1975) Anal Chem 47:592A
241. Sunandana CS (1988) Phys Stat Sol (a) 105:11
242. Yoshihara S, Takahashi R, Okamoto M, Sato E, Fujishima A (1991) Electrochim Acta 36:1959
243. Ragoisha GA, Bondarenko AS (2003) Solid State Phenom 90–91:103. (Proceedings of solid state chemistry, 2002)
244. Ragoisha GA, Bondarenko AS (2004) Surf Sci 566–568:315
245. Ragoisha GA, Bondarenko AS (2003) Electrochem Commun 5:392
246. Bondarenko AS, Ragoisha GA, Osipovich NP, Streltsov EA (2005) Electrochem Commun 7:631
247. Ragoisha GA, Bondarenko AS (2005) Electrochim Acta 50:1553
248. Ragoisha GA, Bondarenko AS, Osipovich NP, Streltsov EA (2004) J Electroanal Chem 565:227
249. Niemantsverdriet JW (2007) Temperature-programmed techniques. In: Spectroscopy in catalysis. An introduction, 3rd edn. Wiley-VCH, Weinheim, p 23, Chapter2
250. Falconer JL, Schwarz JA (1983) Catal Rev Sci Eng 25:141
251. Davies PW, Quinlan MA, Somorjai GA (1982) Surf Sci 121:290
252. Stickney JL, Rosasco SD, Schardt BC, Hubbard AT (1984) J Phys Chem 88:251
253. Angeli J, Bengtson A, Bogaerts A, Hoffmann V, Hodoroabae V-D, Steers E (2003) J Anal At Spectrom 18:670
254. Bogaerts A, Gijbels R (1998) Spectrochim Acta B 53:1
255. Weiss Z (2006) Spectrochim Acta B 61:121
256. Seo M, Fushimi K, Habazaki H, Nakayama T (2008) Corros Sci 50:3139
257. Broda E, Schönfeld T (1955) Radiochemische Methoden der Mikrochemie. In: Hecht F et al (eds) Verwendung der Radioaktivität in der Mikrochemie. Springer, Wien
258. Rogers LB (1950) Anal Chem 22:1386
259. Eichler B, Kratz JV (2000) Radiochim Acta 88:475
260. Kratz JV (2011) Chemistry of transactinides. In: Vértes A, Nagy S, Klencsár Z, Lovas RG, Rösch F (eds) Handbook of nuclear chemistry. Springer Science + Business Media B.V, Springer Dordrecht Heidelberg London New York, p 925, Chapter 20
261. Byrne JT, Rogers LB (1951) J Electrochem Soc 98:457
262. Hummrich H, Banik NL, Breckheimer M, Brüchle W, Buda R, Feist F, Jäger E, Kratz JV, Kuczewski B, Liebe D, Niewisch L, Schädel M, Schausten B, Schimpf E, Wiehl N (2008) Radiochim Acta 96:73
263. Hevesy GV, Paneth F (1915) Monatschefte 36:45
264. Joliot F (1930) J Chim Phys 27:119